Multiscale Investigations on the Mechanical Behaviour and Hydrogen Embrittlement of Advanced Medium Manganese Steel

Weixian Li

Supervisors: Dr Xianghai An

Prof. Julie Cairney

School of Aerospace, Mechanical and Mechatronic Engineering

Faculty of Engineering

The University of Sydney

24 September 2023

This thesis is submitted for the degree of

Master of Philosophy

Statement of originality

I hereby declare that except where specific reference is made to the work of others, the contents of this thesis are original and have not been submitted in whole or in part for consideration for any other degree or qualification in this, or any other University. This thesis is the result of my own work and includes nothing which is the outcome of work done in collaboration, except where specifically indicated in the text. This thesis contains less than 50,000 words, including appendices, references, tables, and equations and has less than 150 figures.

Weixian Li

2023

Authorship attribution statement

This thesis does not contain any material that was published or written by another person except where due reference is made in the text.

Weixian Li

30 June 2023

Xianghai An

30 June 2023

Acknowledgements

I would like to express my sincere gratitude and acknowledge the following individuals for their invaluable support and contributions to my candidature.

First and foremost, I am deeply grateful to my mother and grandma for their unwavering support, both emotionally and financially, from the very beginning of my academic journey. Their constant encouragement and belief in my abilities have been instrumental to my candidature.

I am incredibly fortunate to have the support and guidance of my partner, Ms Xinyi He. Her belief in me, along with their continuous provision of emotional support and professional advice, has been an immense source of strength throughout my candidature.

I am immensely grateful for the professional research guidance provided by my supervisor, Dr Xianghai An. His expertise, support, and constructive feedback have been pivotal in shaping the direction of my research. His assistance in experiment planning, sharing of relevant literature, and insightful feedback on my weekly reports have been truly invaluable.

I would like to acknowledge and express my gratitude to Dr. Hongjian (Andy) Wang from the School of Aerospace, Mechanical, and Mechatronic Engineering for his technical support and professional guidance in planning and conducting various mechanical testings. His expertise and assistance have been crucial in achieving accurate and reliable results.

In addition, I extend my appreciation to former postdoctoral research assistant Dr. Md Nazmul Hasan for his valuable advice on experimental processes and machine parameters, which greatly contributed to the success of this study. I also want to acknowledge my colleague, Ms Heqing Li, for her constructive advice and insightful discussions throughout my candidature.

Furthermore, I would like to acknowledge the technical support provided by the engineers, both current and former, from Sydney Microscopy & Microanalysis. Specifically, I am grateful to Mr Jabco Byrnes and Dr Bryan Lim for their training and general guidance in material sample preparation, Dr Hongwei Liu for his training and technical guidance in transmission electron microscopy, and Dr Vijay Bhatia, Dr Huma Bilal and Dr Limei Yang for their training and technical guidance in scanning electron microscopy and electron back-scattered diffraction.

Lastly, I would like to acknowledge the contributions of all those who have directly or indirectly supported me in this research journey. Thank you all for your assistance, encouragement, and collaboration.

Abstract

The third-generation advanced high-strength steels (AHSS) have attracted significant attention due to their superior combination of strength, ductility, and toughness. The current studied medium Mn steel has demonstrated remarkable mechanical performance among other 3rd-Gen AHSS, with a yield strength of about 1140 MPa, a tensile strength of around 1600 MPa, and a uniform elongation of ~ 30%. These extraordinary mechanical properties could be attributed to the high dislocation density resulting from warm rolling and quenching processes, while the large fraction of elongated retained austenite with a wide range of stability that will be gradually transformed into martensite during deformation can provide a sustained work-hardening effect to enable the excellent ductility. The stress-strain curves indicated the pronounced plastic instability featured by localised deformation that could be reflected by the Lüder band and Portevin-Le Chatelier (PLC) bands. It was found that the discontinuous yielding behaviours were significantly affected by the applied strain rates, in which more prominent stress serration events were observed with decreasing strain rates. In addition, extensive experimental studies were conducted on the effects of strain rates on the discontinuous yielding behaviours using a series of in-situ and ex-situ macroscale and microscale characterisation methods. The experimental results indicated that loading conditions in terms of strain rate and deformation temperature essentially influence the formation of shear bands during deformation, resulting in different kinetics of martensitic transformation and therefore affecting the mechanical properties remarkably.

Hydrogen embrittlement of materials has become a critical issue since hydrogen is believed to be the next generation of fuel. Despite having numerous microstructural traits that were known for having effective hydrogen resistance, the current studied medium Mn steel showed pronounced premature failure after hydrogen ingression, featuring a hydrogen embrittlement index (HEI) of 37%. Microstructural studies suggested that the deformation mechanism was not affected by the hydrogen, whereas the fracture mechanism was heavily altered by the release of mobile hydrogen atoms resulting from phase transformation.

Contents

Contents vii
List of Figures ix
List of Tables xv
Chapter 1 Introduction and literature review 17
  1.1 History of steel 17
  1.2 Medium Manganese steel 19
  1.3 Phase Transformation 24
  1.4 Discontinuous yielding 28
  1.5 Hydrogen embrittlement 37
  1.6 Summary 41
Chapter 2 Experimental Methodology 43
  2.1 Manufacturing process 43
  2.2 Bulk material characterisation techniques 44
    2.2.1 Universal uniaxial tensile tests 44
    2.2.2 Nanoindentation 47
  2.3 Microstructure characterisation techniques 48
    2.3.1 Scanning electron microscopy 48
    2.3.2 Transmission electron microscope 50
  2.4 *In-situ* Observation 52
    2.4.1 Digital image correlation 52
    2.4.2 Infrared camera temperature measurement 54
Chapter 3 Mechanical properties and microstructural characterisation 57
  3.1 Overview 57
  3.2 Tensile stress-strain curve 57
  3.3 Local nanohardness 61
  3.4 Microstructures before deformation 62
  3.5 Microstructures after deformation and fracture surface 65
  3.6 Phase transformation 68
  3.7 Discussion 71
  3.8 Summary 73
Chapter 4 Discontinuous yielding 74
  4.1 Overview 74
  4.2 Strain rate effect 74

4.3 Serrations in the stress-strain curves 80
4.4 In-situ observation 83
  4.4.1 Digital image correlation 83
  4.4.2 Infrared thermographic imaging 87
4.5 Discussion 93
4.6 Summary 96
Chapter 5 Hydrogen embrittlement 97
5.1 Overview 97
5.2 Experimental methodology 97
5.3 Results 99
5.4 Discussion 102
5.5 Summary 104
Chapter 6 Conclusion and future work 106
6.1 Conclusion 106
6.2 Future work 107
Chapter 7 References 110
Appendix A A.1
A.1 Matlab code for post-processing DIC data A.1
A.2 Matlab code for post-processing infrared camera data A.3
A.3 Evidence of VC from TEM images A.6

List of Figures

Figure 1.1 Fe-C equilibrium phase diagram [2] 18

Figure 1.2 Time-temperature-transformation diagram of Fe-C alloying system [4] 19

Figure 1.3 Overview of the steelmaking process and application [6] 20

Figure 1.4 Comparison of strength and elongation of the advanced high-strength steel [15], with the current work highlighted. Interstitial-Free (IF), Bake Hardenable (BH), Carbon-Manganese (CMn), High Strength Low Alloy (HSLA), Press Quenched Steel (PQS), Ferrite-Bainite (FB), Dual Phase (DP), Transformation Induced Plasticity (TRIP), Complex Phase (CP), Dual phase with high formability/ductility (DH), Complex phase with high formability/ductility (CH), TRIP-Assisted Bainitic Ferrite (TBF), Carbide-Free Bainite (CFB), Quenched and Partitioned (QP), Medium Manganese (MedMn), Twinning Induced Plasticity (TWIP), Mild Steel (MS), Press Hardened Steels (PHS). 21

Figure 1.5 Effect of Si addition to Fe-0.18C-3Al-xSi medium manganese steel. The fraction of austenite is controlled by the temperature of intercritical annealing, with LA and HA denoting low and high fractions of austenite, respectively [5] 22

Figure 1.6 Microstructural features of Fe0.47C-10Mn-0.7V. (a) Initial microstructure shows banded-structure and multi-phase feature; (b, c) bimodal grain distribution with equiaxed and elongated grains; (d) slips band 23

Figure 1.7 Study on Fe-0.3C-9Mn-2.4Al-0.2V showing typical manufacturing processes and heat treatments involved in medium Mn steel, reconstructed from [19] 23

Figure 1.8 The Bain strain model of martensitic transformation, white circles represent Fe atom and solid black dots represent carbon atom, a) carbon atom locates in the octahedral site on $[001]\_\gamma$ axis, b) tetragonal unit cell in between two austenite lattices and c) lattice compression along the c-axis 25

Figure 1.9 Relationship between lattice parameter and carbon content of austenite and martensite [1] 26

Figure 1.10 Schematic of dynamic strain aging mechanism explained by C-Mn solutes atom pairs in which grey filled circles represent Fe atom, red filled circles represent C atom and blue filled circles represent Mn atom. In a) C atom locates in the octahedral site pairing with substitutional atom Mn. b) shear displacement for partial dislocation moves the C atom to the tetrahedral site. c) C atom jumps back to the octahedral site due to energetically favourable reorientation of the C-Mn complex [47] 30

Figure 1.11 Formation mechanism of Lüder band proposed by Varanasi et al., in which (a) shows phase constituents, (b) shows shear band preferentially initiate in austenite phase, (c) pile up of shear band leads to activation of shear band in adjacent grain, (d) shear band and intersection causes martensite nucleation and (e) combination effect of shear band coalescence and volume expansion due to martensitic transformation leads to avalanche of deformation [48] 31

Figure 1.12 Surface roughness caused by the passage of the Lüder band [53] 32

Figure 1.13 Schematic of Lüder band propagation, with a) the strain and stress difference between the elastic region and banded region, b) Lüder band propagation from point 1 to point 2, and c) illustrated the change in stress and strain during the propagation [54, 55] 32

Figure 1.14 Types of serrations [63]..35

Figure 1.15 Stress-strain curve of 7Mn-0.3C-2Al at various strain rates [38]. S700: intercritical annealing at 700°C; S720: intercritical annealing at 720°C. 35

Figure 1.16 Hopping of PLC band due to the low austenite stability [38] 36

Figure 1.17 (a) Tensile stress-strain curve and (b) the relationship between the mechanical properties of Fe-11.2Mn-0.22C-1.95Al and strain rates obtained by Cai et al. [45] 36

Figure 1.18 Schematic of the interaction of hydrogen and microstructural defect in metallic material [37]...38

Figure 1.19 Experimental techniques that have been used to study the hydrogen embrittlement phenomenon [67]...38

Figure 1.20 Example of thermal desorption spectroscopy on Fe-7Mn-0.1C-0.5Si, desorption peaks show the difference in hydrogen solubility between austenite and ferrite. HRA and CRA denote hot-rolling and cold-rolling steel, respectively [70]..39

Figure 1.21 Illustration of hydrogen diffusion path and hydrogen embrittlement mechanism by Sun et al. [69]. (a) shows microstructure with sufficient diffusion path (i.e., ferrite phase), leading to HE by HELP mechanism. (b) microstructure with limited diffusion path (i.e., austenite-rich), leading to the HEDE mechanism...41

Figure 2.1 Electron Backscatter Diffraction (EBSD) data after hot-rolling and subsequent cooling of current studied steel (a) EBSD phase map, (b) Inverse pole figure along Z direction (IPF-Z) crystal orientation and (c) local misorientation 43

Figure 2.2 Heat treatment process of the current studied steel 44

Figure 2.3 Experimental setup of the tensile testing machine 45

Figure 2.4 Illustration of universal tensile test with temperature control 46

Figure 2.5 (a) Illustration of the UMIS nanoindentation system [86] and (b) Typical load-displacement (P-h) curve obtained from nanoindentation test [87].......................................48

Figure 2.6 Illustration of twin-jet polishing mechanism. For EBSD sample preparation, the jets were controlled by time, and for TEM sample preparation, the jets were controlled by the passage of light through the specimen [92] 51

Figure 2.7 Schematic of the DIC technique, in which the local strain is calculated from the displacement of speckles in each subset [100] 52

Figure 2.8 Experimental setup of universal tensile testing with DIC and infrared cameras ...53

Figure 2.9 Sample surface after applying speckle pattern 54

Figure 2.10 Visualisation of temperature measurement on the surface of specimen 54

Figure 3.1 Engineering stress-strain curve obtained from universal tensile testing at a strain rate of $1\times10^{-3}s^{-1}$ 58

Figure 3.2 Benchmark of (a) yield strength and (b) ultimate tensile strength verse uniform elongation of medium Mn steel. Symbol coloured in red represent the current studied steel [5, 17, 19, 21, 39, 41-43, 45, 101-103] 59

Figure 3.3 Benchmark of the product of ultimate tensile strength and uniform elongation verse (a) ultimate tensile strength (b) yield strength of medium Mn steel. Symbol coloured in red represent the current studied steel [5, 17, 19, 21, 39, 41-43, 45, 101-103] 60

Figure 3.4 (a) True stress-strain curve and (b) work-hardening rate of the current studied steel obtained from universal tensile testing at a strain rate of 1×10^{-3}s^{-1} 60

Figure 3.5 The hardness of phases obtained using UMIS nanoindentation system with a Berkovich tip 61

Figure 3.6 Initial microstructure of 35-WR-LN before deformation. (a) EBSD phase map, (b) IPF-Z orientation map, (c) Local misorientation map 62

Figure 3.7 Histogram count on grains with respect to their aspect ratio in the initial microstructure 63

Figure 3.8 TEM image of microstructure prior to deformation 64

Figure 3.9 TEM image of zoomed twin structure and vanadium carbide precipitate (more TEM image in Appendix A.3) 64

Figure 3.10 TEM image of BCT martensite in the microstructure before deformation 65

Figure 3.11 Final microstructure of 35-WR-LN after fracture. (a) EBSD phase map, (b) IPF-Z orientation map, (c) Local misorientation map 66

Figure 3.12 Histogram count on grains with respect to their aspect ratio in the final microstructure 66

Figure 3.13 TEM image of present steel after deformation 67

Figure 3.14 Fractography of the current studied steel deformed at 1×10^{-3}s^{-1} 67

Figure 3.15 Transformed austenite fraction at 1×10^{-3}s^{-1} measured by Feritscope and calibrated by EBSD data 68

Figure 3.16 EBSD Phase mapping of the interrupted tensile 35-WR-LN sample at a strain rate of 1×10^{-3}s^{-1}. (a) 6% pre-Lüder strain, (b) 6% post-Lüder strain, (c)12%, (d) 15%, (e)20%, and (f) 25%. 70

Figure 4.1 (a) Engineering stress-strain curve of 35-WR-LN deformed at different strain rates, and (b) Mechanical properties obtained from the curves 75

Figure 4.2 (a) Tensile true stress-strain curve of 35-WR-LN deformed at a range of strain rates, and (b) work-hardening rate calculated from true stress-strain curves. 76

Figure 4.3 EBSD phase map of fractured 35-WR-LN under strain rate-of (a) 1×10^{-1} s^{-1}, (b) 1×10^{-2} s^{-1}, (c) 1×10^{-3} s^{-1} and (d) 5×10^{-5} s^{-1} 77

Figure 4.4 Final austenite phase fraction of fractured tensile sample 77

Figure 4.5 Transformed austenite fraction at a range of strain rates measured by Feritscope and calibrated by EBSD phase data obtained from the initial and fractured sample. Dotted curves fitted by the OC model. 78

Figure 4.6 Parameters fitted from Olson-cohen phase transformation model [34] 79

Figure 4.7 Magnified Lüder band regime of the stress-strain curve. 81

Figure 4.8 Histogram of the magnitude of stress serration event in the Lüder band regime ... 81

Figure 4.9 Magnified work-hardening regime of the stress-strain curve................................82

Figure 4.10 Histogram of stress serration event in work-hardening regime...........................82

Figure 4.11 Strain evolution with time of 35-WR-LN extracted from DIC result at the strain rate of (a)$1\times10^{-1}s^{-1}$, (b)$1\times10^{-2}s^{-1}$, (c)$1\times10^{-3}s^{-1}$ and (d)$5\times10^{-5}s^{-1}$. With arrows indicating band propagation direction and labels showing the speed of propagating bands.............................84

Figure 4.12 Differentiated strain evolution with time of 35-WR-LN extracted from DIC result at the strain rate of (a)$1\times10^{-1}s^{-1}$, (b)$1\times10^{-2}s^{-1}$, (c)$1\times10^{-3}s^{-1}$ and (d)$5\times10^{-5}s^{-}1$. With arrows indicating band propagation direction and labels showing the speed of propagating bands. ..85

Figure 4.13 Normalised speed of Lüder band and PLC bands of 35-WR-LN varied with strain rates 86

Figure 4.14 Band strain extracted from work-hardening curves. Band strain is defined as the true strain between two work-hardening rate peaks in Figure 4.2..86

Figure 4.15 Surface temperature evolution with time of 35-WR-LN extracted from infrared camera result at the strain rate of (a)$1\times10^{-1}s^{-1}$, (b)$1\times10^{-2}s^{-1}$, (c)$1\times10^{-3}s^{-1}$ and (d)$5\times10^{-5}s^{-}1$. With arrows indicating band propagation direction and labels showing the speed of propagating bands. 88

Figure 4.16 Differentiated surface temperature evolution with time of 35-WR-LN extracted from infrared camera result at the strain rate of (a)$1\times10^{-1}s^{-1}$, (b)$1\times10^{-2}s^{-1}$, (c)$1\times10^{-3}s^{-1}$ and (d)$5\times10^{-5}s^{-}1$. With arrows indicating band propagation direction and labels showing the speed of propagating bands. 89

Figure 4.17 Tensile stress-strain curve of 35-WR-LN deformed at 1×10^{-3} s^{-1} with ambient temperatures of 297 K, 333K, 363 K...90

Figure 4.18 EBSD phase mapping of sample deformed at $1\times10^{-3}s^{-1}$ with an ambient temperature of (a) 333 K (87.4% Austenite and 12.6% Martensite) and (b) 363 K (89.3% Austenite and 10.7% Martensite)..92

Figure 5.1 Experimental setup for hydrogen charging of the tensile specimen.......................98

Figure 5.2 (a) Engineering stress-strain curve and (b) true stress-strain curve of the hydrogen-free and hydrogen-charged sample under a strain rate of $5\times10^{-5}s^{-1}$..99

Figure 5.3 Benchmark of hydrogen resistance with other medium Mn steels [68, 70, 72, 77, 78, 121-123]. (a) Product of UTS and UE, and (b) UTS verses hydrogen embrittlement index 100

Figure 5.4 EBSD phase map of (a) original sample before the tensile test, (b) deformed hydrogen-charged sample and (c) hydrogen-free sample after fractured 100

Figure 5.5 In-situ magnetic measurement using Feritscope during the tensile test of hydrogen-free and hydrogen-charged sample under strain rate of $5\times10^{-5}s^{-1}$...101

Figure 5.6 Nanohardness of hydrogen-free and hydrogen-charged samples measured by nanoindentation..102

Figure 5.7 Fractography of hydrogen-free sample strained at $5\times10^{-5}s^{-1}$ with (a) the overview and (b, c) the magnification on layer 103

Figure 5.8 Fractography of hydrogen-charged sample strained at $5\times10^{-5}s^{-1}$ with (a) the overview and (b, c) the magnification on layer 104

Figure 6.1 High-resolution DIC study conducted by in-situ SEM [129]..............................108

Figure 6.2 *In-situ* nanoindentation equipment concept and prototype for hydrogen charging 109
Figure 7.1 VC precipitate found in initial microstructure A.6
Figure 7.2 VC precipitate found in initial microstructure A.7
Figure 7.3 VC precipitate found in initial microstructure A.7

List of Tables

Table 2.1 Electrolyte and equipment settings of Tenupol-5 for electropolishing....................50

Chapter 1 Introduction and literature review

1.1 History of steel

The history of steel can be dated back to the nuclear fusion of stars in the infinite universe, where iron (Fe) and carbon (C), the two indispensable elemental constituents of steel, were formed after a massive explosion. It is difficult to obtain high purity iron in the nature. As dimensions are scaled up into industrial application, the impurity of iron inevitably leads to the deterioration of properties [1]. The combination of iron and carbon opens up extraordinary possibilities beyond pure iron due to the large varieties of microstructures and properties that can be finely tailored by processing and solid-state transformation [1].

There are three types of iron allotropes in the equilibrium state, which are categorised by the crystal structure, containing ferrite (α), the body-centred cubic (BCC) phase; austenite (γ), the face-centred cubic (FCC) phase and hexagonal close-packed (HCP) ϵ phase. As illustrated in the Fe-C equilibrium phase diagram [2] (Figure 1.1), steel exists in different phases depending on the temperature and the weight percentage of carbon. For hypo-eutectoid steel, γ austenite phase dominates at high temperatures. When the temperature dropped below the A3 line, α ferrite started to appear and co-exist with the austenite until the temperature decreased to A1, where all the austenite transformed into pearlite (ferrite + Fe_3C cementite). The regime with a temperature lower than A3 and higher than A1 is referred to as intercritical temperature, and it is a temperature range widely used in the heat treatment of steel due to its essential ability to tailor the microstructural features of both phases. Apart from the equilibrium phases that can be found in the phase diagram, steel also exists in the form of a non-equilibrium phase known as α' martensite that is a crucial phase to strengthen the steels.

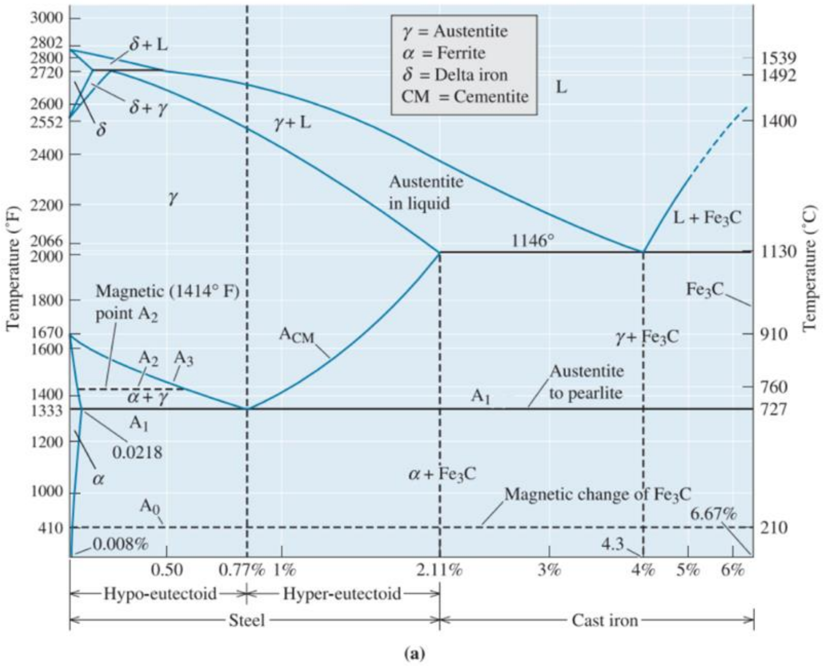

Figure 1.1 Fe-C equilibrium phase diagram [2]

Martensite was named after the German metallurgist Adolf Martens who found the body-centred tetragonal crystal in 1890. Martensite is a non-equilibrium phase obtained by cooling the austenite very rapidly from a high temperature (i.e., quenching). The phase transformation involved is known as the martensitic transformation. Compared with pearlite, martensite is a much harder phase due to the high dislocation density resulting from the rapid transformation [3]. The fast-cooling rate is the key element for martensitic transformation due to the diffusionless characteristic of the transformation. The rate of cooling is so fast that the carbon atom does not have sufficient time for diffusion to form cementite (Fe_3C). The time-temperature-transformation (TTT) diagram illustrated the time dependency of the non-equilibrium phase transformation with a cooling trajectory of possible martensitic transformation curve drawn on the graph (Figure 1.2) [4]. The temperature label, M_s, denotes the martensite starting temperature. If austenite is cooled down below this temperature rapidly, martensite will form accordingly. Another temperature label, M_f, denotes the martensite finishing temperature, and martensite reaches the saturation limit at this temperature. If the austenite is quenched to a temperature lower than this, the volume fraction of martensite will not increase. Symbols M_s and M_f are often used to quantify the stability of austenite [5].

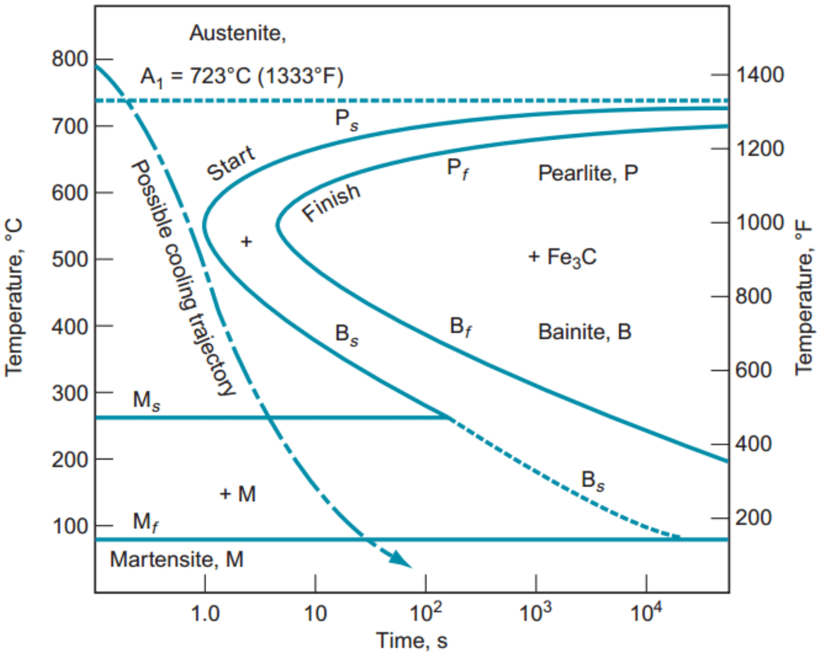

Figure 1.2 Time-temperature-transformation diagram of Fe-C alloying system [4]

1.2 Medium Manganese steel

The variation in phase property resulting from compositional design and processing has enabled the vast possibility of steel applications for different purposes (Figure 1.3), making it one of the most popular alloys in the world [6]. Steel has been used in the automobile industry since the early 20th century. Nowadays, the majority of the body frame of automobile vehicles are still constructed of steel. To meet the safety standard, a special class of high-strength steel was developed, namely the advanced high-strength steel (AHSS). Global warming is a significant worldwide issue, and the automobile industry plays a vital role in this crisis due to the massive fuel consumption for powering and producing vehicles. Optimising the weight by enhancing the mechanical properties of the material used in the vehicles can improve fuel efficiency without sacrificing passenger safety [7].

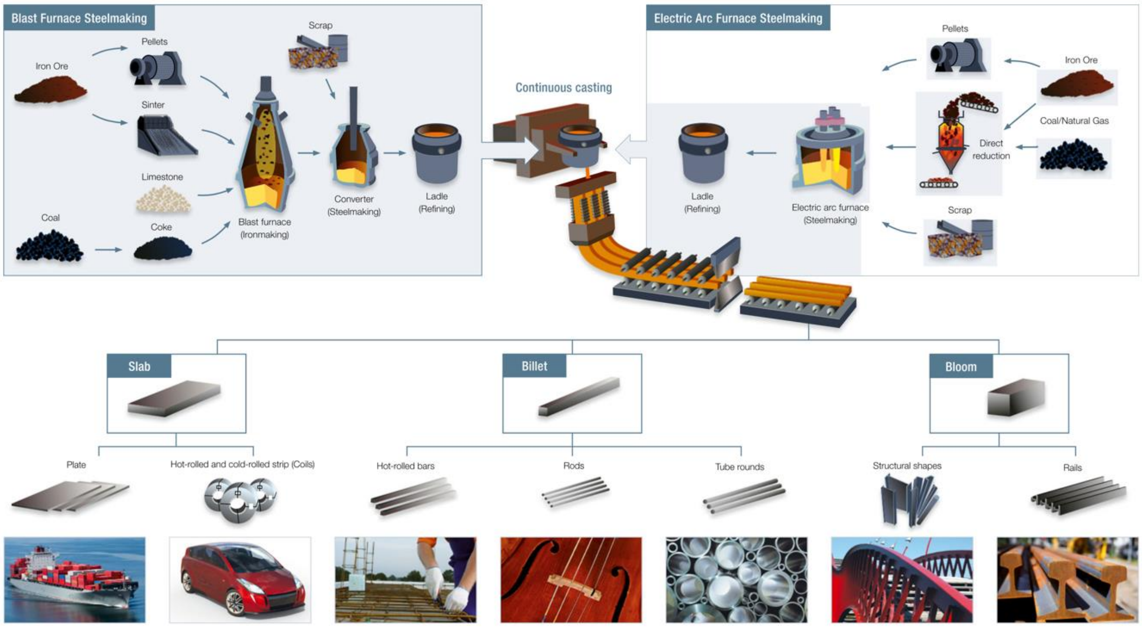

Figure 1.3 Overview of the steelmaking process and application [6]

The first generation of AHSS refers to dual-phase (DP) steel, transformation-induced plasticity (TRIP) steel, complex phase (CP) steel, mild steel (MS), and press-hardened steel (PHS). While having a moderate performance on strength, this group of AHSS was not able to satisfy the formability for making sophisticated automobile parts due to the low ductility (<25% total elongation (TE)) (Figure 1.1) [8, 9]. This led to the development of the second generation of AHSS, the twinning-induced plasticity (TWIP) steel with high Mn content (12% - 30 w.t.%), which can reach a total elongation of 50% (Figure 1.1). However, the displeasingly low yield strength (300-450 MPa), along with the high manufacturing cost and difficulty in processing due to the high alloy content, limited mass production in the automotive industry [10]. Hence, the superior combination of strength and ductility becomes the crucial direction of property improvement of the next generation AHSS [9]. Medium Manganese steel is believed as one of the most promising candidates for the third-generation AHSS, which relies on the transformation of retained austenite to improve the overall mechanical properties.

The original research of medium Mn steels can be dated back to 1972 by Miller [11], who discovered that the transformation of metastable austenite to martensite could significantly enhance the work-hardening ability of steels. The word “medium” refers to the intermediate

Mn content in the manganese composition, typically between 3-12% measured in weight percentage [12]. The addition of manganese stabilises the austenite phase during the thermo-mechanical process of re-heating the steel to intercritical temperature in the Fe-C system, in which the α-ferrite and γ-austenite phases are presented, while the manganese can be partitioned into the austenite phase to increase its stability, leading to the retaining of the austenite at room temperature [10, 13, 14]. During deformation, the retained austenite that is metastable will undergo stress-induced martensitic phase transformation, ensuring the significant work-hardening effect [13].

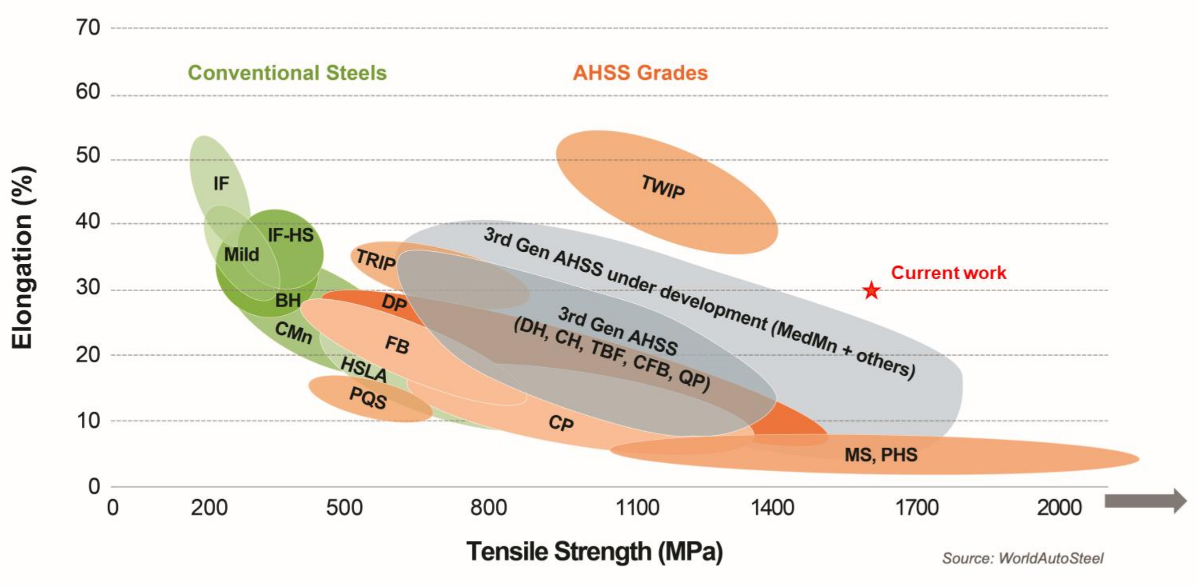

Figure 1.4 Comparison of strength and elongation of the advanced high-strength steel [15], with the current work highlighted. Interstitial-Free (IF), Bake Hardenable (BH), Carbon-Manganese (CMn), High Strength Low Alloy (HSLA), Press Quenched Steel (PQS), Ferrite-Bainite (FB), Dual Phase (DP), Transformation Induced Plasticity (TRIP), Complex Phase (CP), Dual phase with high formability/ductility (DH), Complex phase with high formability/ductility (CH), TRIP-Assisted Bainitic Ferrite (TBF), Carbide-Free Bainite (CFB), Quenched and Partitioned (QP), Medium Manganese (MedMn), Twinning Induced Plasticity (TWIP), Mild Steel (MS), Press Hardened Steels (PHS).

Unlike the element of Mn, the addition of Aluminium (Al) to medium Mn steels was reported to have the opposite effect due to its ability to stabilise ferrite [16]. It can also reduce the mass density of the material due to its relatively light atomic weight. Silicon, having a similar effect to Al, stabilises the ferrite phase by expanding the intercritical range of the two-phase region, resulting in the formation of delta (δ) ferrite with a typically large grain size (Figure 1.5) [5].

Strain partitioning was eliminated, attributed to the layered morphology separated by the δ ferrite [5].

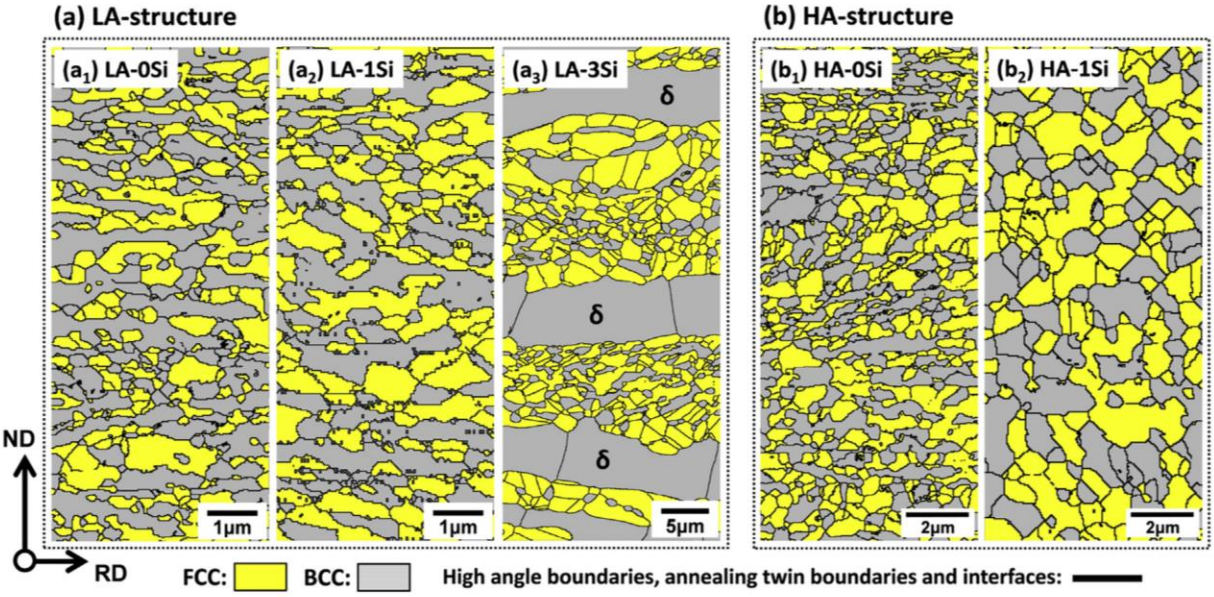

Figure 1.5 Effect of Si addition to Fe-0.18C-3Al-xSi medium manganese steel. The fraction of austenite is controlled by the temperature of intercritical annealing, with LA and HA denoting low and high fractions of austenite, respectively [5]

The additions of Vanadium (V) [14, 17], Titanium (Ti) [18], Molybdenum (Mo), and Niobium (Nb) could significantly promote the formation of precipitates and then further improved the mechanical properties of medium Mn steels [12]. For instance, Hu et al. [17] discovered that the formation of Vanadium carbides in ferrite and austenite, combined with warm rolling at intercritical temperature, followed by intercritical annealing, could greatly increase the yield strength of Fe-0.47C-10Mn-0.7V by 650MPa. To be more specific, the introduction of Vanadium carbides provided three major benefits: 1) precipitate strengthening during deformation (Figure 1.6 e-f); 2) promoted extensive work-hardening during the warm rolling process which increases the yield strength through dislocation strengthening; and c) facilitating the formation of the bimodal grain distribution (Figure 1.6 a-d) by preventing recrystallisation and decreasing the rate of dislocation annihilation, which would greatly enhance the strength-ductility synergy [17].

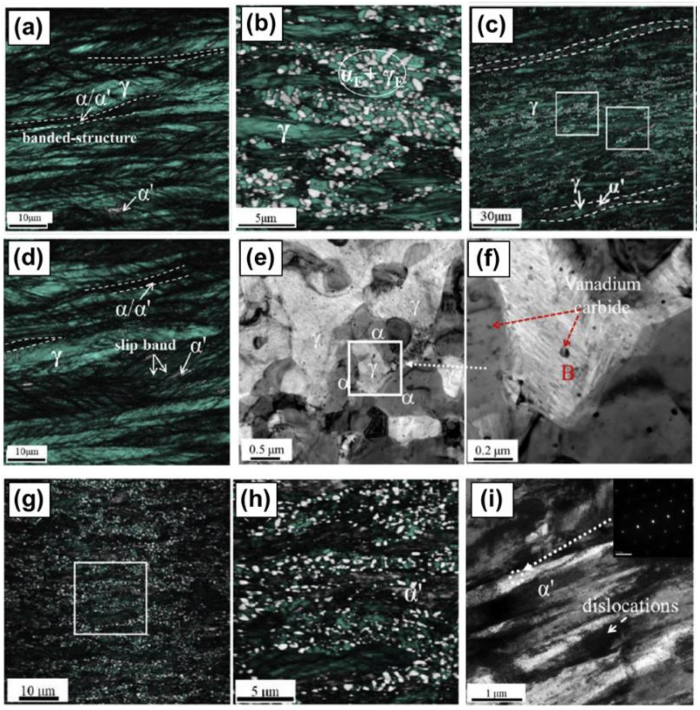

Figure 1.6 Microstructural features of Fe0.47C-10Mn-0.7V. (a) Initial microstructure shows banded-structure and multi-phase feature; (b, c) bimodal grain distribution with equiaxed and elongated grains; (d) slips band indicated the formation of martensite; (e,f) Vanadium Carbide in austenite phase under TEM; (g,h) EBSD phase distribution and grain morphology after fracture; and (i) TEM image after fracture [17]

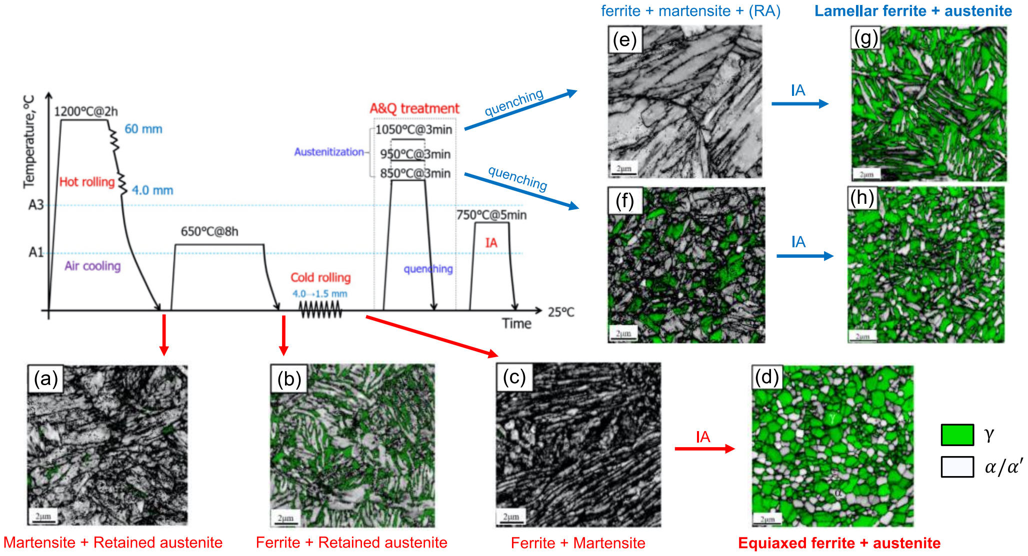

Figure 1.7 Study on Fe-0.3C-9Mn-2.4Al-0.2V showing typical manufacturing processes and heat treatments involved in medium Mn steel, reconstructed from [19]

Metallurgists have made enormous efforts to tailor the microstructure of medium Mn steels by adjusting the alloying content and the manufacturing process, meanwhile tuning the heat treatment conditions in terms of temperatures and durations has also attracted lots of focus. However, the manufacturing process and the following heat treatment can be quite sophisticated in medium Mn steels. A diagram in Figure 1.7 illustrates the typical steps involved. Homogenisation and hot rolling are deployed to make the distribution of all alloying compositions uniform and reduce the thickness, respectively. The resultant microstructure contained mainly martensite with embedded austenite depending on the cooling rate and alloying composition (Figure 1.7a) [20]. A prolonged annealing process at a relatively low temperature was applied to allow chemical partitioning to their preferential phase, creating stabilising effect correspondingly (Figure 1.7b) [20]. In recent studies, the cold rolling process was also employed to promote the formation of martensite in order to improve the mechanical strength [14, 20] (Figure 1.7c). The intercritical annealing process was then used to promote recrystallisation and recovery of austenite and ferrite grains, leading to an equiaxed grain morphology (depending on parent morphology and duration of intercritical annealing), as shown in Figure 1.7d-h [20].

Despite the extraordinary mechanical properties of medium Mn steels, the multi-phased microstructure and the complex deformation mechanism imposed critical challenges, which are ambiguous and yet to be determined, on the development of this kind of advanced steel, hindering it from real-world applications. Recent investigations have not only been focused on improving the mechanical properties [14, 17, 21] but also on elucidating the fundamental deformation mechanism, such as phase transformation and discontinuous yielding behaviour, including the yield point elongation with the formation of Lüder band [19, 22-24], and the Portenvin-Le Chatelier (PLC) effect during the work-hardening stage of deformation [25, 26].

1.3 Phase Transformation

Martensitic transformation is a displacive process without the diffusion of atoms involved. The model of the transformation in terms of crystal structure had been uncovered by E. C. Bain, known as the Bain strain [1, 27, 28], illustrated in Figure 1.8. Initially, the carbon atom locates in the octahedral site of the austenite lattice (Figure 1.8). Since the transformation is diffusionless, the position of the carbon atom remained stationary during the entire process. For the set of edges in BCC, which shares the octahedral site with austenite, a carbon will remain, leading to the tetragonal distortion in one of the axes in the BCC lattice (Figure 1.8).

Therefore, the body-centred cubic is distorted to body-centred tetragonal with an elongated $c_{\alpha'}$ lattice parameter. The length of $c_{\alpha'}$ varies with the carbon content of the material, as illustrated in Figure 1.9 [1]. The linear relationship could be roughly expressed using the following equation 1.1 [29, 30]:

$$\frac{c_{\alpha'}}{\alpha_{\alpha'}} = 1 + 0.045\, w.t.\%C \tag{1.1}$$

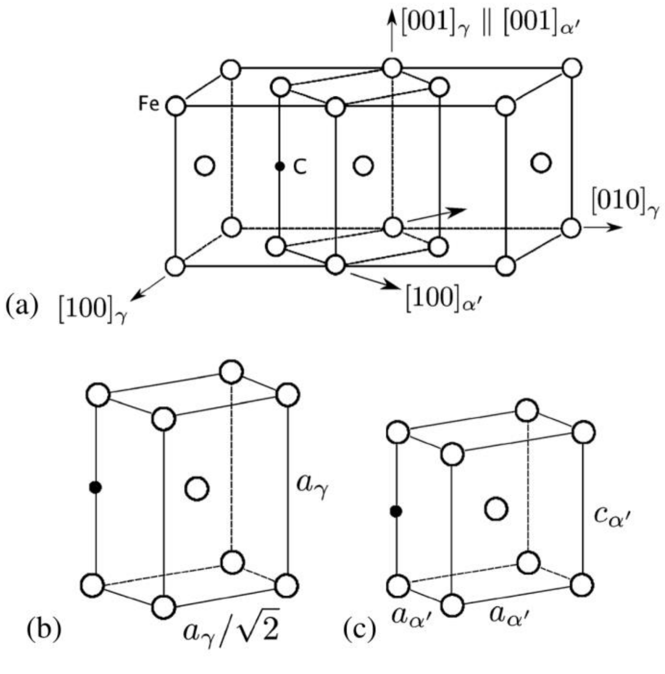

Figure 1.8 The Bain strain model of martensitic transformation, white circles represent Fe atom and solid black dots represent carbon atom, a) carbon atom locates in the octahedral site on [001]_γ axis, b) tetragonal unit cell in between two austenite lattices and c) lattice compression along the c-axis

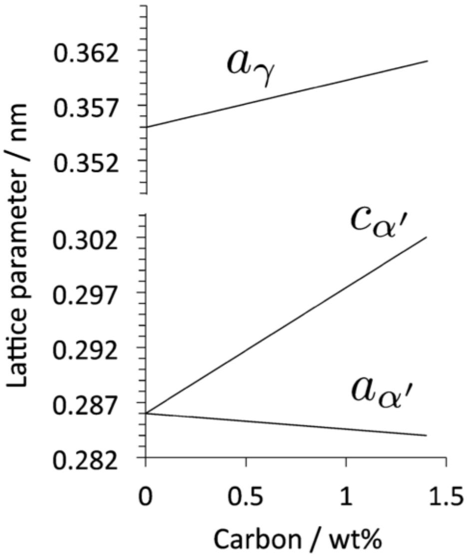

Figure 1.9 Relationship between lattice parameter and carbon content of austenite and martensite [1]

The crystallographic orientation relationship between austenite and martensite has been investigated and reported by numerous authors, including the Kurdjumov-Sachs (KS) OR [31], Nishiyama-Wasserman OR [32] and Greninger-Troiano OR [33], etc. The KS OR is used to describe the crystallographic relationship most frequently by researchers, which can be presented as [31]:

$$\{1\ 1\ 1\}_\gamma\ ||\ \{0\ 1\ 1\}_{\alpha'} \qquad \langle 1\ 0\ \bar{1}\rangle_{\alpha'}\ ||\ \langle 1\ 1\ \bar{1}\rangle_{\alpha'}$$

Besides the crystallographic orientation, investigations on the kinetic of strain-induced martensite formation were conducted decades ago with one of the most famous models proposed by Olson and Cohen [34, 35], known as the OC model. The model presumed that the regions of shear bands were the major martensite nucleation site. Hence the model could be initiated by setting the volume fraction of the shear bands, f^{sb}, in matrix austenite with respect to the strain value ϵ:

$$\frac{df^{sb}}{(1-f^{sb})} = \alpha d\epsilon \tag{1.2}$$

The parameter α is a strain-independent constant representing the formation rate of the shear band and increased with increasing strain rate and decreasing stacking fault energy (SFE). By integrating the equation 1.2, the volume fraction of the shear bands could be expressed as:

$$f^{sb} = 1 - \exp(-\alpha\epsilon) \tag{1.3}$$

By assuming a constant average volume of shear bands in each austenite volume, $\bar{v}^{sb}$, the number of shear bands per unit austenite volume, N_v^{sb}, could be worked out by:

$$N_v^{sb} = \frac{f^{sb}}{\bar{v}^{sb}} \tag{1.4}$$

Then, the number of shear-band intersections in each austenite volume, N_v^I, could be approximated by:

$$N_v^I = K(N_v^{sb})^n \tag{1.5}$$

Where K is a constant related to the grain size, and n is also a constant that accounts for the more frequent shear band intersection after the earlier stage of deformation, where the shear band tends to nucleate in a parallel manner. As mentioned above, assuming that the shear band intersection is the nucleating site of martensite, the number of martensite produced per unit austenite volume, $N_v^{\alpha'}$, could be approximately estimated by:

$$dN_v^{\alpha'} = p\,dN_v^I \tag{1.6}$$

The parameter p is the probability that a shear-band intersection will nucleate a successive martensite embryo, and it follows a Gaussian relationship with the temperature. Now, assuming the average volume per martensite unit $\bar{v}^{\alpha'}$, the incremental volume of the transformed martensite with respect to the total volume of austenite could be correlated to the number of martensites produced per unit of austenite volume that was previously approximated:

$$\frac{df^{\alpha'}}{1 - f^{\alpha'}} = \bar{v}^{\alpha'} dN_v^{\alpha'} \tag{1.7}$$

Upon rearranging and integrating, the relationship between the martensite fraction and the strain could be worked out as follows:

$$f^{\alpha'} = 1 - \exp\left\{-\frac{\bar{v}^{\alpha'}K}{(\bar{v}^{sb})^n}p[1 - \exp(-\alpha\epsilon)]^n\right\} \tag{1.8}$$

A parameter β was utilized so that:

$$\beta = \frac{\bar{v}^{\alpha'}K}{(\bar{v}^{sb})^n}p \tag{1.9}$$

This leaves the martensite fraction to be related to three terms, α and β, in which a is the rate of shear band formation, and β is related to a material constant n, and p that is the probability for a shear-band intersection to form a martensite embryo. The probability p tends to decrease with increasing temperature due to the reduced chemical driving force. Noting that some errors may be preserved in this model due to the neglected factors such as the temperature-induced softening effect and any stress-induced thermodynamical effects [34].

1.4 Discontinuous yielding

Medium Mn steels have been recognised as the third-generation advanced high-strength steels owing to their superior strength and ductility combination while maintaining affordable cost [8]. Under external loading, the martensitic transformation of retained austenite contributes to significant work-hardening of the material leading to the increase in strength and elongation, namely the transformation-induced plasticity (TRIP) [36, 37]. However, due to the localised TRIP effect [25, 38], this kind of steel often features the discontinuous yielding phenomena, namely the Lüder band and Portevin–Le Chatelier (PLC) band that may originate from the static strain aging (SSA) and dynamic strain aging (DSA) effect, respectively [25, 39]. Both the Lüder band and PLC band represent the plastic instability of metastable austenite during the deformation [25, 38, 40]. While the Lüder band generally occurs immediately after the yield point where the yield stress drops and followed by the yield point elongation, the PLC band happened during the work-hardening stage, which is associated with numerous stress serrations. It is believed that localised deformation takes place inside the bands and propagates along the longitudinal direction (i.e., rolling direction) of the tensile specimen.

The occurrence of Lüder strain is commonly observed in steels, and it is also frequently reported in medium Mn steels [19, 22, 41, 42]. This type of discontinuous yielding features with yield drop in the transition region from elastic to plastic deformation and a yield point elongation with a monotonous increase in strain without apparent strengthening [1]. The yield drop phenomenon is commonly recognised as the sudden movement of a large amount of mobile dislocation, either by the unpinning effect of dislocation from the interstitial carbon atmospheres or the newly generated mobile dislocation inside the microstructure [1]. It was reported that the presence of the Lüder strain could be highly related to the microstructure morphology. Han et al. [43] revealed that the cold-rolled medium Mn steels consists of equiaxed morphology demonstrated a large yield drop and yield point elongation at the early stage of plastic deformation, whereas this phenomenon was absent from the hot-rolled sample with a lamellar microstructure.

The other type of discontinuous yielding behaviour often reported in medium Mn steels is the PLC effect [21, 22, 25]. It is reflected, on the stress-strain curve, by the flow stress serration in the work-hardening stage [25]. Previous investigations proposed that the formation of PLC bands is associated with the dynamic strain aging (DSA) effect, in which the mobile dislocation is temporally pinned by the so-called Cottrell atmosphere formed by diffusible C and Mn atoms [44]. The stress serrations on the stress-strain curve are associated with the rapid pinning and unpinning motions of the dislocations. In the medium Mn steels, it is believed that the formation of PLC bands is essentially affected by the grain size, phase stability, the distribution of C and Mn atoms, and the SFE of the austenite phase. In addition, the extrinsic parameters, such as testing temperature and strain rate, have significant effects on the formation of the PLC bands as well [45, 46].

In term of the grain size, it is proposed that smaller grain sizes could not supply sufficient dislocation for PLC due to a lack of dislocation sources [19]. For larger grain sizes, both grain interiors and grain boundaries contribute to dislocation generation, resulting in sufficient dislocation density [38]. It was also pointed out that the strain-induced martensite has a hindrance effect on the propagation of the PLC band, and in return, the PLC band tends to hop around at lower strain when there is still plenty of austenites with low stability that exist in the microstructure [38]. Also, Sun et al. [25] revealed that the specimen with higher austenite stability did not show discontinuous yield behaviour, i.e., Lüder strain and PLC band. The author further indicated that the SFE played a critical role in the discontinuous yielding since the SFE controls the amount of partial dislocations. Nevertheless, the SFE is also determined by the amount of C-Mn complex, which is responsible for the DSA effect [25, 47] (Figure 1.10).

The stability of retained austenite was considered an important variable for the onset of discontinuous yielding [4, 5, 12]. Varanasi et al. [48] reported that the localised plastic zone was more pronounced in the Lüder band front by comparing similar material with a significant difference in austenite stability. Stacking faults accommodated the deformation of austenite, and the interceptions between them promoted the occurrence of martensitic transformation, leading to further volume expansion, which also deformed the neighbour grains and then resulted in a large area of the plastic zone (Figure 1.11) [48].

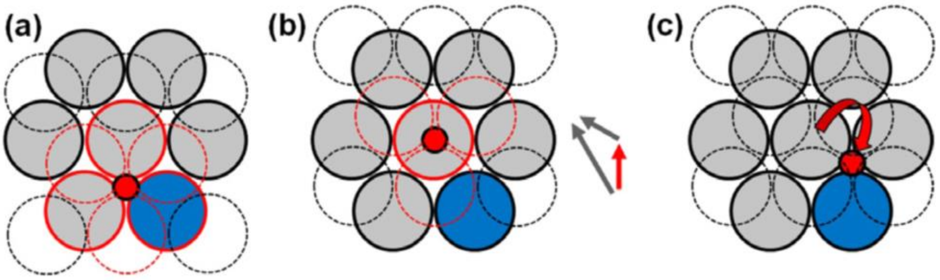

Figure 1.10 Schematic of dynamic strain aging mechanism explained by C-Mn solutes atom pairs in which grey filled circles represent Fe atom, red filled circles represent C atom and blue filled circles represent Mn atom. In a) C atom locates in the octahedral site pairing with substitutional atom Mn. b) shear displacement for partial dislocation moves the C atom to the tetrahedral site. c) C atom jumps back to the octahedral site due to energetically favourable reorientation of the C-Mn complex [47]

DSA theory is widely recognised as the main cause of discontinuous yielding in metallic alloying systems such as Ni-C alloys, Mg-Al alloys, and across a wide range of steels such as TRIP and TWIP steels [38]. This mechanism described the phenomenon that the interstitial carbon atom in the stable octahedral site could be pushed by the leading partial dislocation to the unstable tetrahedral site from the so-called Cottrell atmosphere [44, 49]. At the same time, the mobile dislocations moved inside the material and could be temporarily stopped by obstacles such as grain boundaries, forest dislocations, and precipitates [50]. The stopped mobile dislocations will then be locked by the Cottrell atmosphere and require accumulating sufficient stress to break free from this atmosphere. At the early stage of deformation, where strain rate and temperature rise are small, solute atoms without diffusivity are triggered, which is known as static strain aging [51]. During the later stage of deformation, with the assistance of imposed strain rate and increased temperature, solute atoms with sufficient diffusivity cause the rapid pinning and unpinning effect to dislocations, leading to the dynamic strain aging effect [38, 52].

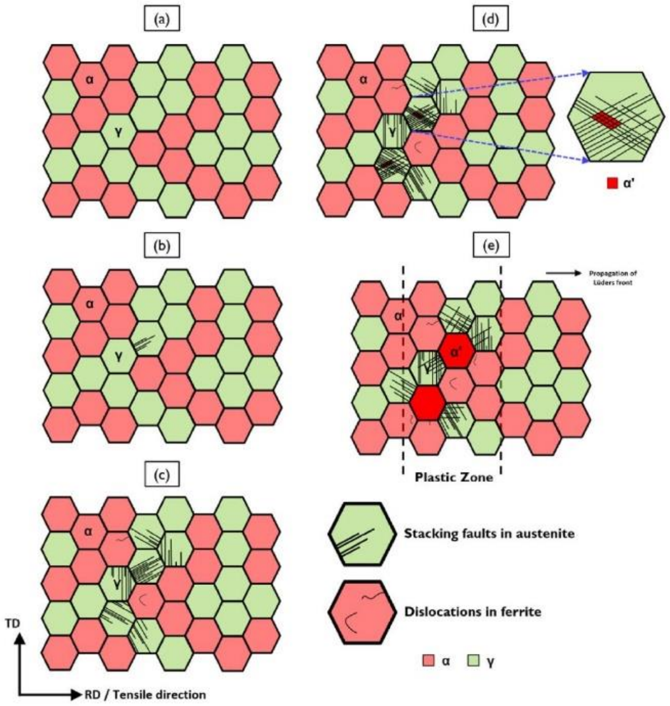

Figure 1.11 Formation mechanism of Lüder band proposed by Varanasi et al., in which (a) shows phase constituents, (b) shows shear band preferentially initiate in austenite phase, (c) pile up of shear band leads to activation of shear band in adjacent grain, (d) shear band and intersection causes martensite nucleation and (e) combination effect of shear band coalescence and volume expansion due to martensitic transformation leads to avalanche of deformation [48]

Due to the discontinuous yielding phenomena, the surface of the steel after deformation will contain uneven layers, as shown in Figure 1.12 [1, 53, 54]. Scanning electron microscopy (SEM) can allow us to have a closer look at the formation mechanism of this effect in the sub-micron scale. Koyama et al. [54] discovered that the rough surface is formed by the coalescing of deformation bands initiated from the edge of the specimen before the arrival of propagating

Lüder band, which can be attributed to the higher true local yield stress than the macroscopic stress. The propagating path of the deformation bands depends on the local hardness of the constituent phase(s) and/or grain(s) [54].

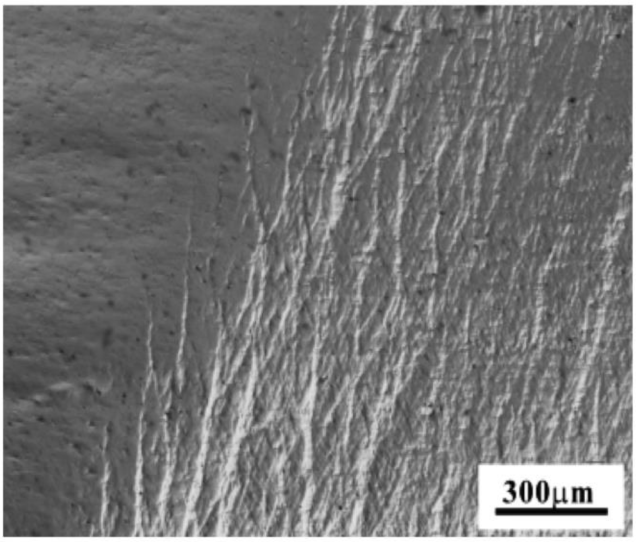

Figure 1.12 Surface roughness caused by the passage of the Lüder band [53]

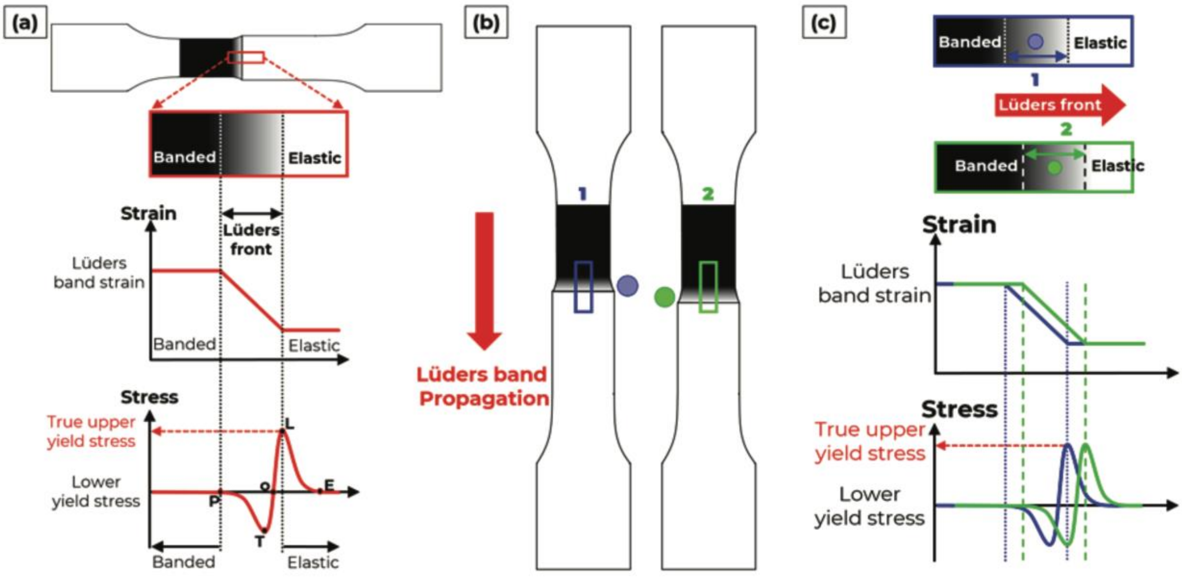

Figure 1.13 Schematic of Lüder band propagation, with a) the strain and stress difference between the elastic region and banded region, b) Lüder band propagation from point 1 to point 2, and c) illustrated the change in stress and strain during the propagation [54, 55]

Dislocation multiplication theory has also been used to explain discontinuous yielding behaviours. It was proposed that two requirements are needed to initiate discontinuous yielding, 1) initially low density of mobile dislocation and 2) rapid multiplication of mobile dislocation [41]. Therefore, medium Mn steels with ultra-fine equiaxed grains are prone to discontinuous yielding, whereas the lamellated counterparts are less likely to suffer from this effect due to the initially high density of mobile dislocation inherited from the hot-rolling process [43, 56]. However, this effect reappears when the rolling temperature is reduced [17, 21]. It was also reported that strain partitioning occurred in the soft ferrite phase, whereas the austenite phase with higher hardness underwent transformation within the Lüder band region [43, 57, 58], although many argued that retained austenite grain would yield prior to ferrite [41, 48].

Numerous characterization techniques were deployed to explore these plastic instability phenomena, including nanoindentation, in-situ magnetic induction measuring of austenite transformation [25], digital image correlation (DIC) technique [25, 26, 38, 40, 59, 60], infrared thermography (IRT) technique [40], ex-situ X-ray diffraction (XRD) technique [38] and in-situ high energy X-ray diffraction (HE-XRD) method [59, 60]. The main purpose of these techniques is to identify the nucleation sites of martensite and how these nucleation behaviours affect strain localization. Sun et al. [25] conducted an experimental study on medium Mn steels and demonstrated that the martensitic content in the material increased with the formation of the Lüder band and PLC bands using the in-situ magnetic induction method. By using IRT technique, Wang et al. [40] discovered, from the thermodynamic point of view that, besides the released heat due to the plastic strain in the Lüder band and PLC bands, there is an additional 56.4% of heat dissipation which they associated with the martensitic transformation. By using in-situ HE-XRD method, Zhang et al. [59, 60] and Ma at al. [59, 60] observed that strain partitioning behaviour occurred simultaneously with the present of plastic instability. However, among these research findings, despite a clear connection between phase transformation and plastic instability was established, the role of microstructure and how it contributes to phase transformation and plastic instability remains unknown.

The strain rate has a substantial effect on DSA since it essentially controls the dislocation velocity. It was reported that sufficiently high dislocation velocity could suppress the dislocation pinning [61] and a critical strain value is needed to activate the DSA with the expression of the equation 1.10 shown below [61]:

$$\dot{\varepsilon} = KC^n \exp\left(-\frac{Q_M}{RT}\right)\varepsilon_c^m \tag{1.10}$$

Where $\dot{\varepsilon}$ is the strain rate, parameters K, n, and m are constants contributing to the calculation of the rate of dislocation increase per unit strain, C is the carbon concentration, Q_M is the energy required to activate the DSA, T denotes the ambient temperature where the sample is deformed, R is the gas constant, and ε_c is the critical strain for stress serration to occur.

In the classic DSA theory, dislocations are locked by the obstacles that exist in the microstructure and can be described by a temporal term, the waiting time. The waiting time of dislocation is expressed by the equation below, with L representing the dislocation mean free path and v_d denoting the dislocation velocity.

$$t_w = \frac{L}{v_d} \tag{1.11}$$

By differentiating the relationship equation between dislocation velocity and macroscopic strain $\varepsilon = \rho_m bl$, the waiting time of dislocations at the obstacles could be expressed by the following equation, where ρ_m is the mobile dislocation density, and b is the Burgers vector of a full dislocation [62].

$$t_w = \frac{\rho_m bL}{\dot{\varepsilon}} \tag{1.12}$$

Stress serration induced by the PLC bands can be divided into five types based on the features presented on the stress-strain curves [38, 62-64] (Figure 1.14). Type A serration features with periodic stress jump and drop resulted from the rapid formation of deformation bands, which propagated from one end of the specimen to the other [63]. Type B serration can be reflected by more frequent stress changes but with a smaller amplitude which results from the propagation of discontinuous bands [63]. Type C serration exhibits periodic yield drops below the level of the stress-strain curve [63]. Type D serration features with yield plateaus-type curves like the Lüder band in which work-hardening is barely noticed outside of the propagating band [63]. Type E serration has a similar feature to Type A but with smoother stress jumps and drop, which generally occurs at high strain level [63].

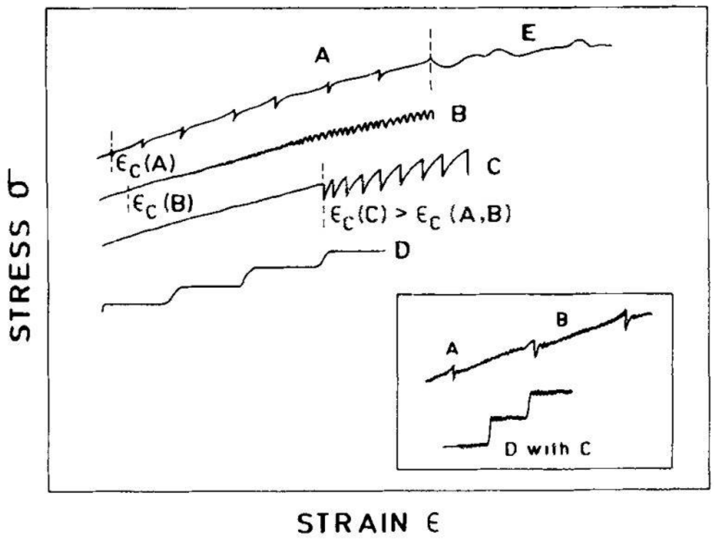

Figure 1.14 Types of serrations [63]

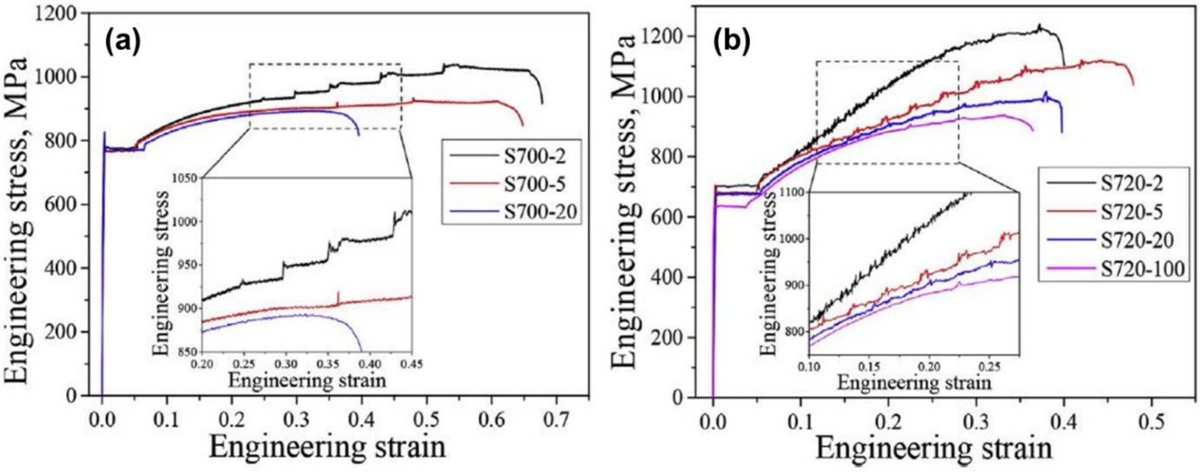

Figure 1.15 Stress-strain curve of 7Mn-0.3C-2Al at various strain rates [38]. S700: intercritical annealing at 700°C; S720: intercritical annealing at 720°C.

In medium Mn steel, various types of PLC bands have been observed. Yang et al. [38] reported the alternation of the PLC band from Type A+B to Type A when the stability of retained austenite is low, whereas the sample with moderate austenite stability presented a monotonic Type A PLC band (Figure 1.15). The author suggested that retained austenite stability affected the PLC type because the larger amount of martensite hindered the propagation of the Type A PLC band, causing the hopping effect (Type B) (Figure 1.16) [38]. The author also reported that stress serration was suppressed at a strain rate above $3.34\times10^{-2}s^{-1}$ (equivalent to 20mm/min constant crosshead speed). Noticeable changes in mechanical properties were also observed where total elongation and ultimate tensile strength decreased with increasing strain rate, i.e., negative strain rate sensitivity (NSRS).

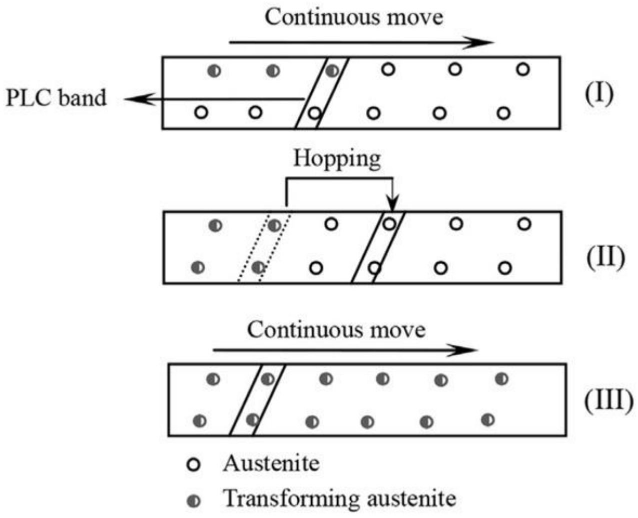

Figure 1.16 Hopping of PLC band due to the low austenite stability [38]

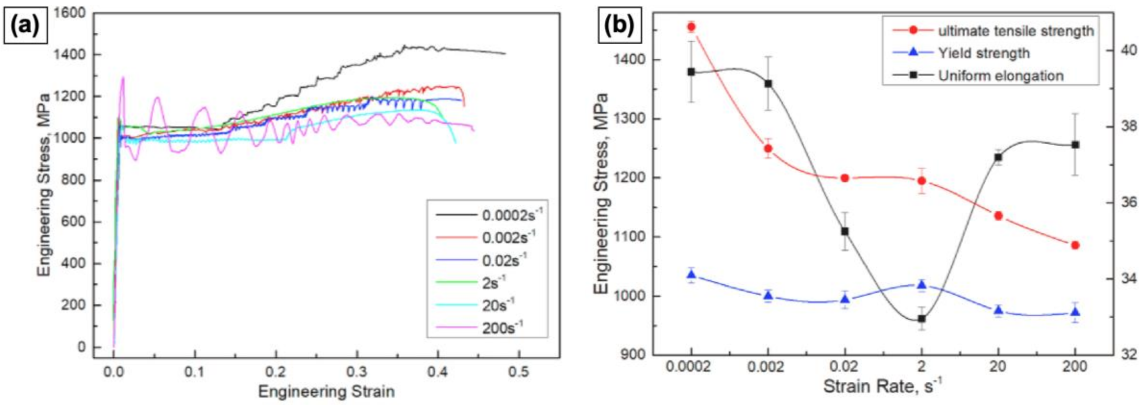

Figure 1.17 (a) Tensile stress-strain curve and (b) the relationship between the mechanical properties of Fe-11.2Mn-0.22C-1.95Al and strain rates obtained by Cai et al. [45]

A similar phenomenon on NSRS was reported by Cai et al. [45] in a medium Mn steel tested on different strain rates, where the ductility experienced a reduction as the strain rate increased to moderated level (0.02-2s^{-1}) (Figure 1.17), followed by a rebound of ductility as the strain rate further increased. The authors attributed the decrease in ductility at a moderate strain rate to the reduced TRIP effect and the decrease in dislocation density [45]. The subsequent rebound of ductility resulted from the appearance of the TWIP effect and softening effect due to the elevated sample temperature at a high strain rate [45]. In contrast, the ultimate tensile stress experienced a continuous decrease with strain rates, which can be due to the change from normal stress-dominated deformation to shear stress-dominated mode, while the yield strength remained relatively constant [45] (Figure 1.17). It could be obtained that the ductility is closely related to the volume fraction of austenite, implying that the TRIP effect dominates the ductility performance. However, the yield strength and tensile strength are dominated by other factors, such as the TWIP effect and temperature-induced softening effect. A similar alternation of the PLC band as exhibited by Yang et al. [38] was reported, where PLC characteristics shifted from Type A+B to Type C and then disappeared as the strain rate increased [45].

1.5 Hydrogen embrittlement

Hydrogen, as the lightest element in the world, can readily enter the crystal lattice as an interstitial atom deteriorating the mechanical properties of the steel, namely the hydrogen embrittlement (HE) [65]. Indeed, HE is a critical problem in high-strength steel because hydrogen can dissolve into the metal at various stages ranging from manufacturing to real-life servicing [66], making the prohibition of hydrogen ingress almost impossible. When the material is loaded during service, the penetrated hydrogen may interact with all types of microstructural defects, causing an unexpected premature failure (Figure 1.18) [37]. Studies on the hydrogen embrittlement issue have been conducted extensively by many researchers using various experimental techniques ranging from macro to nanoscale (Figure 1.19) [67], but this issue remains unresolved yet. This problem becomes more crucial and complicated when it comes to medium Mn steels due to their complex microstructure and high-strength property. To improve the hydrogen susceptibility of medium Mn steels, the mechanism of HE should be elucidated.

Ferrite and martensite possess a body-centred crystal structure, while austenite possesses a face-centred structure. Formers are weak hydrogen trapping site, meaning that hydrogen can easily diffuse through these phases and causes significantly vulnerable HE effects [68-70]. Later is a strong hydrogen trapping site with low hydrogen permeability[68, 70]. This phenomenon could be observed experimentally by evaluating the desorption peak on thermal desorption spectroscopy (TDS) (one typical example is shown in Figure 1.20) [68-74]. HE could be prominently worsened when it combines with the TRIP effect owning to the transformation of austenite to martensite. The trapped hydrogen will be released and diffuse freely in the martensite phase, leading to a more deteriorating HE behaviour [69].

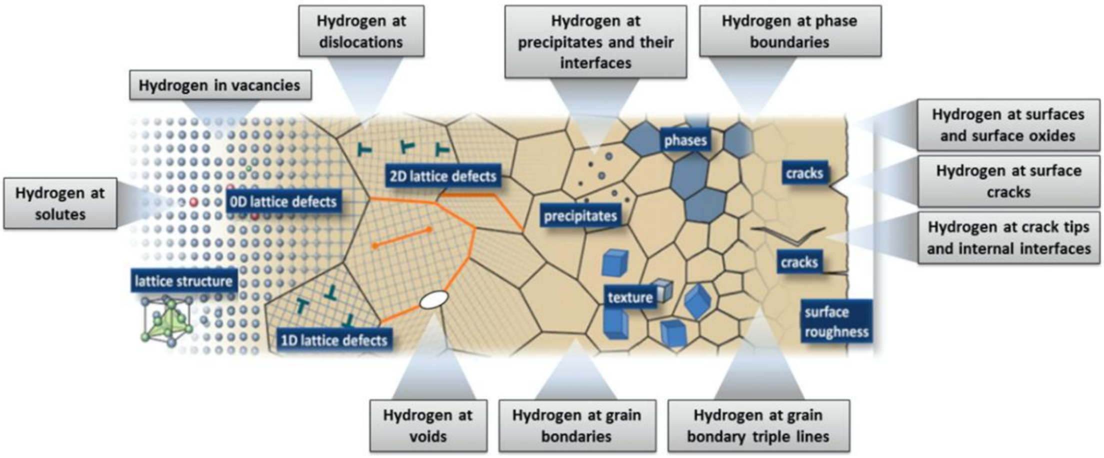

Figure 1.18 Schematic of the interaction of hydrogen and microstructural defect in metallic material [37]

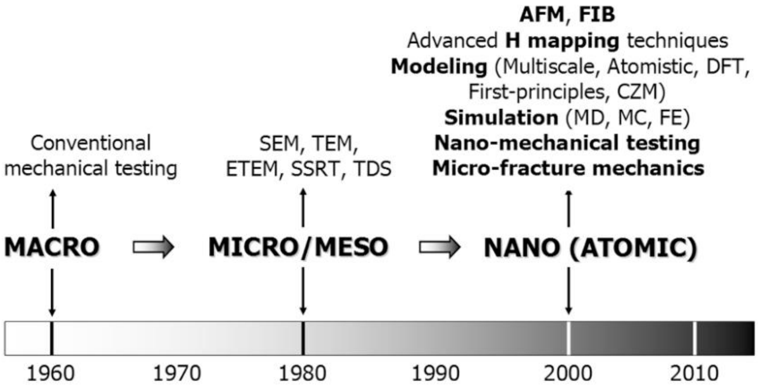

Figure 1.19 Experimental techniques that have been used to study the hydrogen embrittlement phenomenon [67]

To evaluate the resistance of a material to HE, total elongation loss (TEL) or hydrogen embrittlement index (HEI) is frequently used [69, 75-78]:

$$HEI(\%) = \left(\frac{TE_i - TE_H}{TE_i}\right) \times 100\% \tag{1.13}$$

Where the TE_H is the total elongation of the hydrogen-charged sample, and TE_i represents the total elongation of the uncharged sample. The larger the elongation loss after hydrogen charging, the larger the HEI (i.e., lower the hydrogen resistance). The value of total elongation is obtained by slow-strain rate tensile test (SSRT), typically in the order of 10^{-4} -$10^{-5}s^{-1}$ [75]. The SSRT ensures the susceptibility of hydrogen is maximized compared to the conventional-strain rate test ($10^{-3}s^{-1}$) because the sluggish dislocation motion at a slow-strain rate provides enough time for it to interact with hydrogen atoms [79].

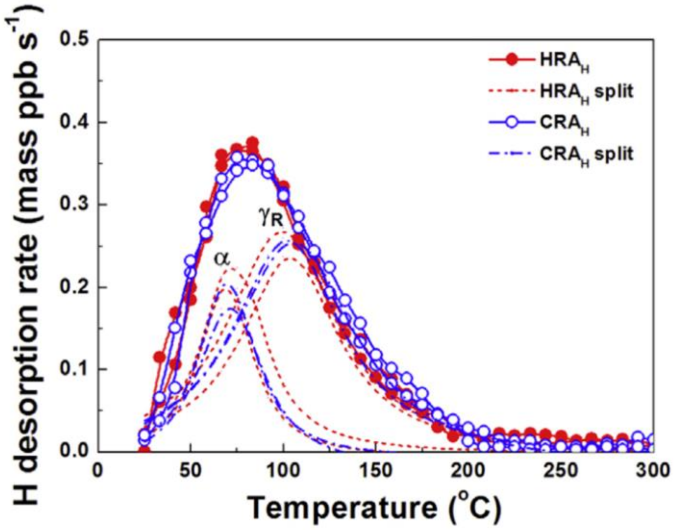

Figure 1.20 Example of thermal desorption spectroscopy on Fe-7Mn-0.1C-0.5Si, desorption peaks show the difference in hydrogen solubility between austenite and ferrite. HRA and CRA denote hot-rolling and cold-rolling steel, respectively [70].

Although the mechanisms behind the HE is not fully understood, it is believed that this phenomenon is driven by several mechanisms in materials, including hydrogen-enhanced decohesion (HEDE), hydrogen-enhanced local plasticity (HELP), hydrogen-enhanced strain-induced vacancy formation (HESIV), and adsorption-induced dislocation emission (AIDE). In fact, extensive investigations reported that the HEDE, HELP, and HESIV mechanisms were found to be responsible for the HE in medium Mn steels with hydrogen ingression [69, 70, 72, 75, 78, 80-82].

Han et al. [70] investigated the effect of microstructural morphology achieved by hot-rolling and cold-rolling on the HE. The author reported that HE in lamellar-grain medium Mn steel was driven by the HEDE mechanism proven by the flat facet and intergranular fractography. The cracks initiated at and propagated along the prior austenite grain boundaries, causing the intergranular fracture. The equiaxed-grain specimen also experienced intergranular fracture caused by the HEDE mechanism, and it was found that the cracking tend to occur along the phase interphase between austenite and ferrite, although it was unclear whether the cracks were formed before or after the phase transformation from austenite to martensite [70].

Sun et al. [69] explored the influence of the phase fraction of austenite on hydrogen susceptibility and illustrated the difference in the hydrogen diffusion path. The author reported a shift of the HE mechanism from HELP to HEDE as the austenite phase fraction increases, which could be related to the difference in the state of diffusible hydrogen [69]. With a lower austenite fraction (Figure 1.21a), hydrogen atoms are free to diffuse and interact with the mobile dislocations, readily leading to the formation of voids as stress increase, i.e., the HELP mechanism (Figure 1.21a). As the austenite phase fraction increases, most hydrogen atoms are trapped and not easily diffusible (Figure 1.21b). During deformation, austenite underwent the martensitic transformation, and hydrogen atoms were released. The diffusible hydrogen will then segregate to the α/α' interface and reduce the cohesion strength of the interface, promoting crack formation, i.e., the HEDE mechanism (Figure 1.21b) [69].

Research by Jeong et al. [77] focused on the variation of the hydrogen percolation behaviour with different austenite morphology. Zhang et al. [78] investigated the HE of the lamellar medium Mn steel with different lath thicknesses achieved by controlling the thickness reduction during warm rolling. Ryu et al. [68] investigated the effect of δ ferrite on HE by altering the aluminium alloying content, whereas Shao et al. [72] investigated the same aspect by tailoring the silicon alloying content.

Additionally, experimental procedures contribute considerable effects on the HE tolerance of steels. For example, Wang et al. [83] compared the effect of pre-strain on the cold-rolled and annealed medium Mn steel with recrystallized equiaxed grain structure. Lu et al. [84] utilised in-situ nanoindentation to perform a real-time study on the hydrogen effect on nano-hardness and martensitic phase transformation. Pop-in behaviour (the sudden increase in displacement during the nanoindentation test) was found to be intensified, and the nanohardness was increased by the ingression of hydrogen [84]. Also, the hydrogen has a suppression effect on the martensitic formation because the SFE was decreased, which effectively hinders the cross-slip of dislocations [84].

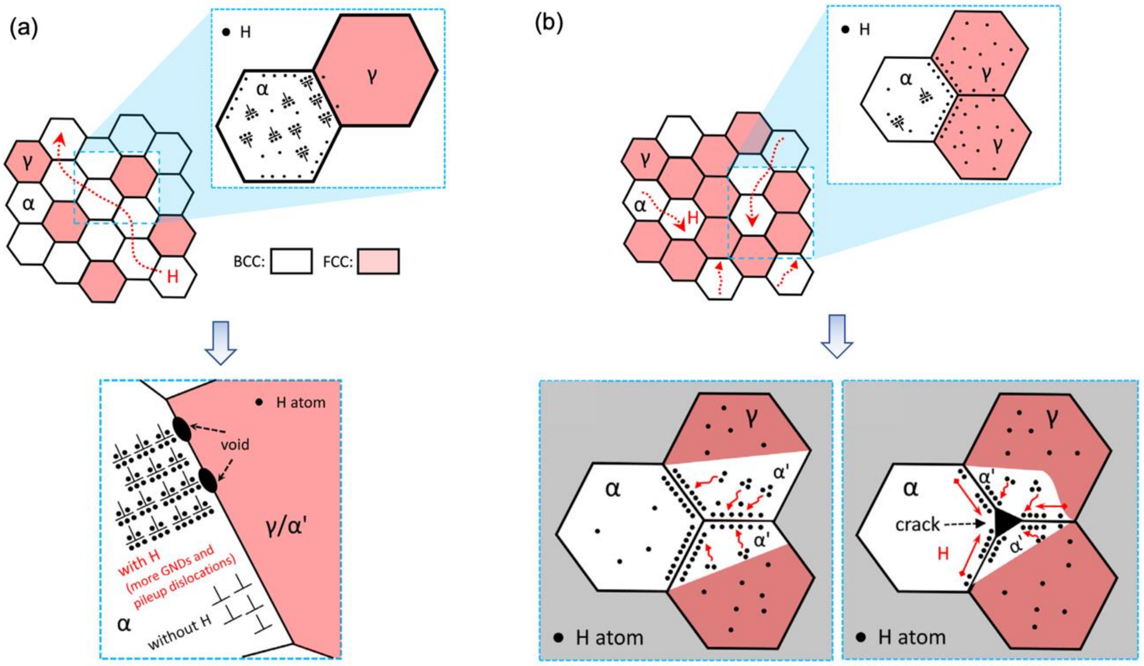

Figure 1.21 Illustration of hydrogen diffusion path and hydrogen embrittlement mechanism by Sun et al. [69]. (a) shows microstructure with sufficient diffusion path (i.e., ferrite phase), leading to HE by HELP mechanism. (b) microstructure with limited diffusion path (i.e., austenite-rich), leading to the HEDE mechanism.

1.6 Summary

Steel has been wildly applied in multiple industries for centuries, and material engineers around the globe have been investigating to quest various methods to improve the mechanical properties of steel for more cost-effective production and a more sustainable future. Medium manganese steel, one of the most promising candidates for next-generation advanced high-strength steel, attracts enormous attention due to its superior properties in terms of high strength and excellent ductility. The medium Mn steel that was studied in this project possessed an exceptional combination of strength and ductility, which can be attributed to the carefully designed alloying compositions and heat treatments. The mechanical properties of the current studied steel will be revealed in Chapter 3, whereas the experimental methodology will be covered in Chapter 2.

Despite the extraordinary mechanical performance, several research problems have not been fully elucidated, which hinders the industrial application of medium Mn steel. Among these problems, discontinuous yielding behaviour has raised substantial awareness, and a number of theories have been proposed to explain this phenomenon. It was evident that the applied strain rate and deformation temperature would affect the discontinuous yielding in the Fe-C alloy system, but the underlying mechanism is yet to be uncovered from the microstructural perspective. The phase transformation involved in the deformation of medium Mn steel further increased the complexity of the problem due to the interaction of different phases and microstructural features. In this regard, the following project focuses on examining and understanding the factors that would affect the discontinuous yielding behaviour in medium Mn steel, and the result and discussion are reported in Chapter 4. In addition, Hydrogen has been treated as one of the best candidates for renewable energies, but the issues related to hydrogen embrittlement have yet to be fully understood, especially in high-strength structural steel. In this regard, the problems related to hydrogen embrittlement in the present medium Mn steel will be studied. Furthermore, some microstructural features that are known to be beneficial to improve the resistance to hydrogen embrittlement were engineered into the present steel, and therefore, the previously reported theories could be tested. The result and discussion are presented in Chapter 5.

The thesis will be concluded in Chapter 6 with recommendations for future works based on the experimental experience and findings that we gained from the current work, shedding some light on the future development of medium Mn steel.

Chapter 2   Experimental Methodology

2.1   Manufacturing process

The medium Mn steel used in this study has a chemical composition of Fe-12Mn-0.35C-2Al-0.4V-0.8Mo (in weight percentage). It was first cast into a steel ingot in the vacuum induction furnace. After heat treatment for homogenisation at 1473 K (1200 °C) for 2 hours, the steel ingot was subjected to hot rolling at 1373 K (1100 °C), and the resulting hot-rolled microstructure is shown in Figure 2.1. It could be observed that the hot-rolled steel consisted of equiaxed grains with the grain sizes of tens of microns and a large amount of Σ3 twin boundaries, which were annealing twins inherited from the elevated rolling temperature. The phase constituent was dominated by FCC austenite with few embedded BCC phase (Figure 2.1a). The local misorientation map (Figure 2.1c) shows that the dislocation density is minor because the dynamic recrystallisation readily occurred during the deformation at elevated temperatures, which also promotes the occurrence of the dynamic recovery, except that some local misorientation can be observed near the BCC phase.

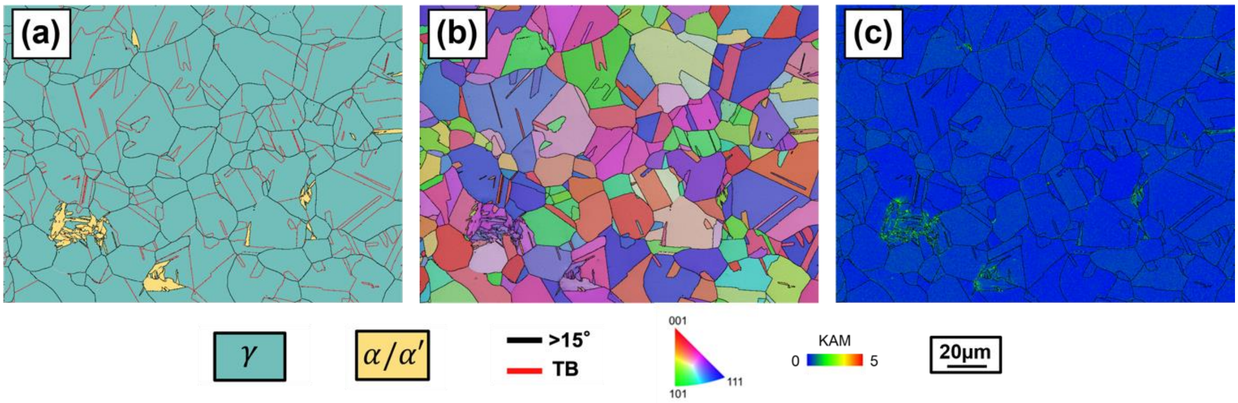

Figure 2.1 Electron Backscatter Diffraction (EBSD) data after hot-rolling and subsequent cooling of current studied steel (a) EBSD phase map, (b) Inverse pole figure along Z direction (IPF-Z) crystal orientation and (c) local misorientation

Then, the steel was subjected to the warm rolling processes at 1023K (750°C) within the intercritical temperature between A3 and A1 in the Fe-C equilibrium phase diagram (Figure 1.1). Subsequently, the warm rolled steel was quenched immediately in liquid nitrogen at a temperature of 77K (-196°C) for the deep cryogenic treatment. The whole processing and heat treatment procedures are illustrated in Figure 2.2. The warm rolled steel strip was then cut to the tensile samples by electrical discharge machining. The length of the gauge section is 15mm, with thickness of 1.8mm and width of 2.3mm.

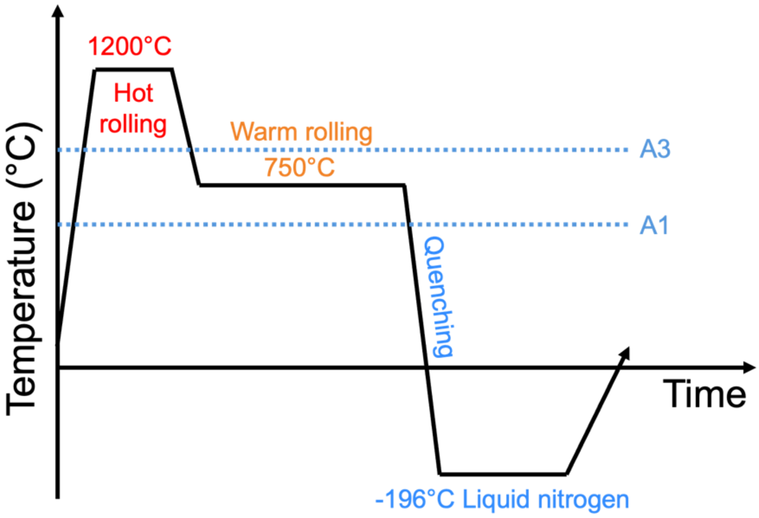

Figure 2.2 Heat treatment process of the current studied steel

2.2 Bulk material characterisation techniques

2.2.1 Universal uniaxial tensile tests

Uniaxial tensile testing is widely used for studying the mechanical properties of bulk material. The dog-bone-shaped sample, usually with either a rectangular or circular cross-section, is loaded into the universal tensile testing machine, with two ends clamped by mechanical grips. During the tensile testing, the uniaxial force will be applied by the load cell, which is controlled by the constant crosshead speed set before the test. Although the load frame of the tensile testing machine was designed to be rigid in the idealised case, minor movement on joints and deformation of structural components were inevitably induced due to the forces applied during the test. To minimise the effects and maximise the accuracy of the measurement of engineering strain, the extensometer was implemented to the gauge length of the sample, as illustrated in Figure 2.3.

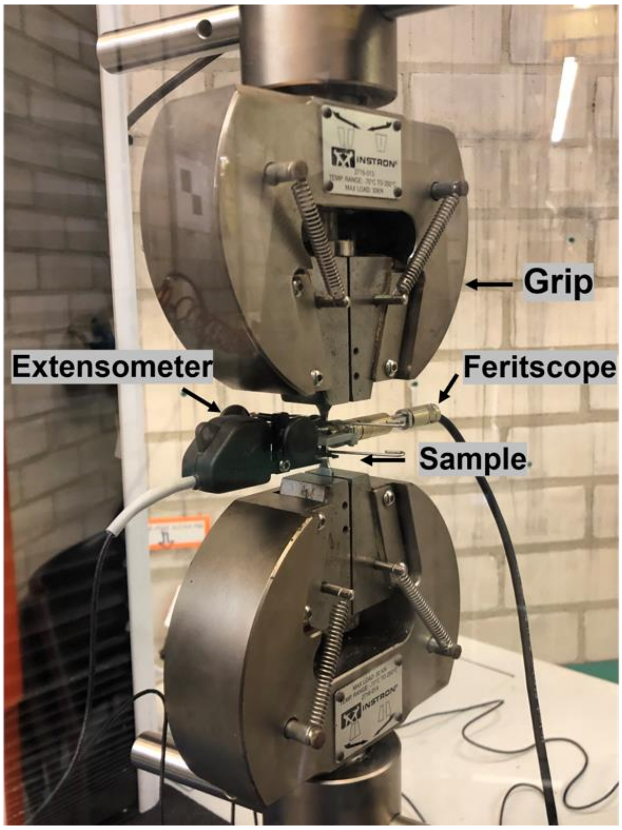

Figure 2.3 Experimental setup of the tensile testing machine

Due to the difference in magnetic properties between austenite and martensite, the FMP30 Feritscope from Helmut Fischer GmbH can be applied to record the real-time phase transformation, which was implemented to the surface of the specimen with a probing area of 2 mm × 2 mm. A dedicated clamping accessory for attaching the Feritscope to the tensile specimen was designed and modelled using Solidwork and additively manufactured with Polylactic Acid (PLA) printing filament using Ultimaker S3 fused deposition modelling (FDM) 3D printer. The maximum measuring frequency of the Feritscope is 5 Hz (0.2 s per measurement), providing sufficient temporal resolution for the phase transformation during the deformation. The Feritscope was positioned on the gauge section of the tensile specimen, as shown in Figure 2.3, allowing us to measure the real-time phase transformation during the tensile experiments.

To examine the ambient temperature during the universal tensile test, a thermally insulated cabinet with a built-in heater was used (Figure 2.4). The mechanical grips and Instron strain gauge were placed within the cabinet, with the Fluke 724 temperature calibrator placed next to the specimen, ensuring accurate control of the temperature. The variation of temperature during the test was controlled within ±1 K.

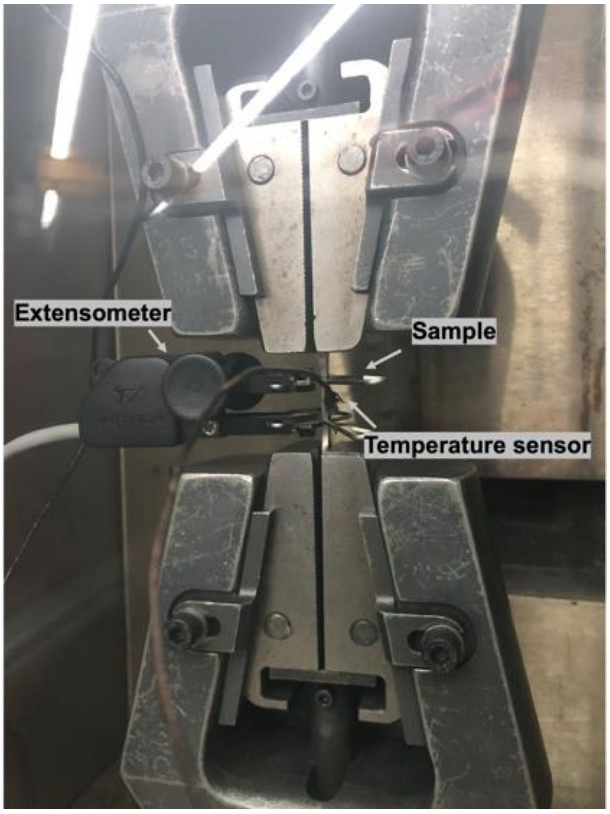

Figure 2.4 Illustration of universal tensile test with temperature control

Three tensile tests were repeated for every test condition to ensure the reliability of data and the standard deviation was calculated and represented by the error bar.

Sample preparation is a vital and compulsory process for all testing specimens, especially for steel that is readily subject to oxidation under ambient conditions. A proper sample preparation procedure could mitigate the inconsistency of experimental results and improve the measurement precision. The inaccuracy of results introduced to the sample during sample preparation, such as phase transformation, bending contour, and deformation, could also be prevented by the correct sample preparation techniques.

Tensile dog-bone-shaped samples were ground and polished using a rotary polisher to minimise the surface roughness effect [54], promoting surface crack formation during deformation. Both the sample surfaces along the normal direction and transverse direction were mechanically ground using grit size P80 (200µm) silicon carbide (SiC) paper to remove any surface rust and flatten the unlevel surface resulting from the residual strain inherited from the warm rolling process. The resultant tensile specimen would have consistent thickness and width across the gauge section.

With progressively increasing the grit size from P80, P180 (80µm), P400 (35µm), P1200 (15µm), and P4000 (5µm), the final surface of the samples would not contain scratches larger than 5µm. All the remaining scratches were homogenously distributed, and the surface roughness effect on the tensile result could be neglected. Before performing the tensile test, the width and thickness of the sample were measured three times, and the average values were taken to ensure the accuracy of the stress calculation.

2.2.2 Nanoindentation

Nanoindentation technique has been widely applied to measure the local hardness of materials in multi-phase materials [38, 57, 58]. The difference in hardness between austenite, ferrite, and martensite would introduce strain partitioning due to the plastic mismatch, which leads to stress concentration on phase boundaries [12, 60, 85]. To study the possible influence of strain partitioning on the current studied steel, a load-controlled nanoindentation test was conducted with the UMIS system from CSIRO (Figure 2.5a). The load was set at 20mN to ensure accurate measurement with a loading rate of 2mN/s.

The specimen for nanoindentation underwent identical preparation as the EBSD sample (in Chapter 2.3.1) and was mounted on a rigid base to support the specimen during loading. The Berkovich indenter tip was used for the measurement of hardness, with the area function of $A = 24.5h_p^2$ [86], in which h_p denotes the plastic depth. Load-displacement (P-h) curve was logged by the UMIS software, and the hardness of the specimen was worked out by power law fitting the top 75% of the elastic unloading curve (Figure 2.5b). After the nanoindentation, the sample was characterised using the EBSD for phase identification.

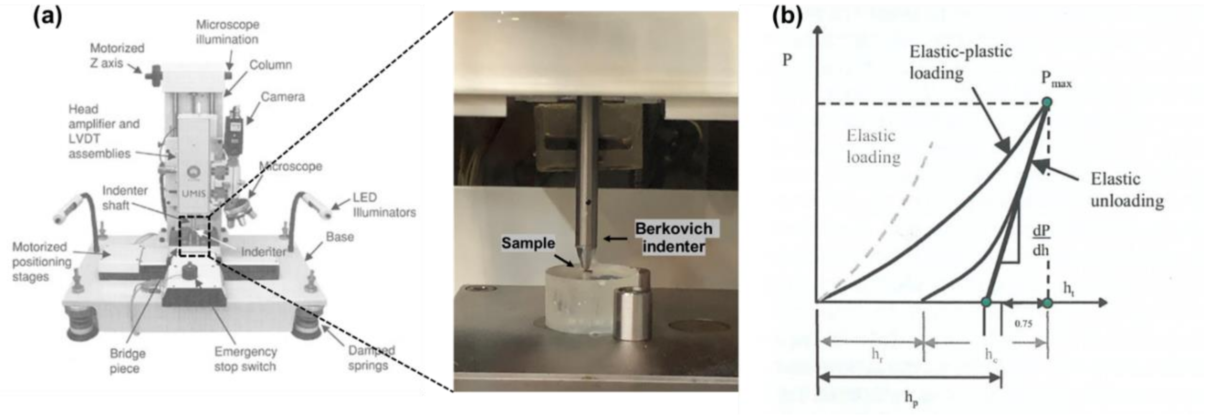

Figure 2.5 (a) Illustration of the UMIS nanoindentation system [86] and (b) Typical load-displacement (P-h) curve obtained from nanoindentation test [87]

2.3 Microstructure characterisation techniques

2.3.1 Scanning electron microscopy

Study on the material has been focused on not only the macroscopic point of view, but the microscopic perspective is also vital since most of the metallic material is formed by a finite amount of grains ranging from several micrometres to nanometre, which exceeds the resolution of human eyes (0.3 mm) [88].

Electron microscopy has been used widely and evolved rapidly in the field of material science to study the microstructure and the behaviour of the material under external load and other environmental conditions. The active interaction between the emitted electrons and the metal atom generates valuable information for the study of the microstructure of material by detecting the scattered electrons using an electronic sensor. For scanning electron microscope (SEM) imaging, secondary electrons are the source of the signal and provide a way of studying the surface topography on the sample surface. Hence, the secondary electron mode is widely used to obtain the fractography of fractured tensile samples.

When the emitted electrons are elastically scattered from the sample surface, they will undergo the so-called Bragg diffraction. Then, each set of planes will give rise to a Kikuchi line, and with sufficient Kikuchi line detected, the crystal structure of the metal could be obtained. This method is known as electron-backscattered diffraction (EBSD). The incident electron beam hits the sample surface at a 70-degree angle, and then scattered electrons will be detected by the EBSD detector. This characterization technique provides information on the corresponding phase and the crystal orientation, making studies on multi-phase material, grain size, grain morphology, and crystal texture possible.

Due to the size limitation of the SEM chamber and EBSD sample holder, the steel specimen required to be sectioned to size. The Struers Accuton-50 equipped with a 50A13 SiC cutting disc was used. The specimen was clamped onto the arm of the cutting machine, which allows precise X and Y position adjustment. Water injection was applied to reduce the heat released from the friction, preventing the alternation to microstructure due to the excessive heat. The step size of the moving arm was set at 0.025 mm/min to prevent potential fracturing of the cutting disc.

The sectioned specimen segment was then glued to the platen of Fischione's model 160 specimen grinder for the pre-thinning process. The platen with specimen was installed into the specimen grinder and was thinned using P400, P1200, P2500, and P4000 SiC paper. Each of the thinning processes with different grit sizes would remove a layer of at least three times the grain size of the SiC particles to mitigate the deformation layer effect, e.g., using P4000 (5µm) SiC paper to polish down a 30µm deformation layer induced by P2500 (10µm) SiC paper. With the equipped graduated scale on the specimen grinder, the thickness of the specimen can be thinned easily and precisely.

After pre-thinning the specimen to 500-1000µm, it was removed from the platen by submersing it into acetone to dissolve the adhesive. The solution and specimen were placed into an ultrasonic cleaner to accelerate the dissolution of the superglue. After mechanical polishing, the specimen with a thickness of 500-1000µm was taken to the twinjet electropolishing machine Tenupol-5 for the final preparation, with the specification listed in Table 2.1. The specimen, after electropolishing, would be mounted to the SEM sample stub using adhesive silver conductive paint. The secondary electron and EBSD images in the current study were conducted on the Zeiss Ultra Field Emission Scanning Electron Microscope and the Zeiss EVO SEM. Secondary electron images in this project were performed at an accelerating voltage of 5 kV and a working distance of 8 mm, whereas EBSD images were performed at a voltage of 15 kV and a working distance of 14.4 mm. The step size was set at 80 nm, so that the ultrafine grains were able to be distinguished. The raw EBSD data was processed by commercial software CHANNEL5 so that the unindexed data points could be interpolated. At least three EBSD scans were performed on each sample to accurately measure the phase fraction from EBSD data, with standard deviation shown by the error bar. For the fractured specimen, the samples for the EBSD study were cut within 3mm from the fracture surface, to ensure the measured phase fraction was accurate.

Table 2.1 Electrolyte and equipment settings of Tenupol-5 for electropolishing

Solution	6% perchloric acid + methanol
Voltage	25V
Temperature	-20°C
Flow rate	22
Polishing time	10s

2.3.2 Transmission electron microscope

The transmission electron microscope (TEM) is an advanced electron microscope invented in 1931, seven years prior to the scanning electron microscope [94]. Although these two microscopes share a similar internal structure to the SEM with an additional intermediate lens, the imaging mechanism between them is different. The SEM forms an image by detecting the electrons that are reflected or knocked out, whereas the TEM forms an image from the electrons transmitted through the specimen, providing valuable information about the internal microstructure within the crystal. Therefore, the sample for TEM needs to be thin (<100nm) so that the high-energy electron beam can be transmitted through, and the image could be probed to the fluorescent screen placed at the bottom section of the TEM chamber.

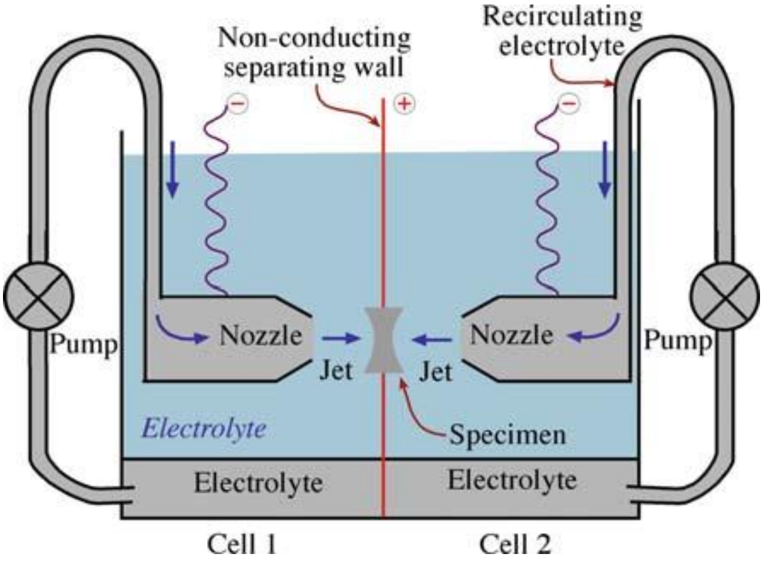

Figure 2.6 Illustration of twin-jet polishing mechanism. For EBSD sample preparation, the jets were controlled by time, and for TEM sample preparation, the jets were controlled by the passage of light through the specimen [92]

Sample preparation for TEM shares similar steps as EBSD sample preparation. The sample undergoes the same pre-thinning procedure as the EBSD sample, except the final thickness of the specimen would be ~80μm to reduce the polishing time for electropolishing. The 80μm specimen was disc-punched to <3mm in diameter disc so that it could fit into the designated TEM sample holder. Finally, it was taken to the twin-jet electropolishing machine and electro-polished with the same machine setup as the EBSD sample (Table 2.1), except the polishing time was automatically controlled by the twin-jet polisher, in which the flow would stop once it detected the light could pass through the specimen, and trigger the sensor (Figure 2.6). Finally, the TEM images in the current study were conducted on the JEOL JEM-2100 and JEM-2200 operated at voltage of 200 kV.

2.4 *In-situ* Observation

2.4.1 Digital image correlation

Discontinuous yielding behaviour can be reflected in the tensile stress-strain curves. However, the detailed characteristics that could be observed and analysed from the stress-strain curve are quite limited. Hence a direct observation of strain distribution on the sample surface is required to explore the distinct deformation traits. Here, we applied the advanced digital image correction (DIC) method to capture the localised strain changes by calculating the movement of pre-painted speckles during tensile deformation (Figure 2.7) [95-97]. DIC images allowed us to capture the initiation of the bands and enable the measurement of band propagation velocity, band initiation site, and angle of the band [48, 98, 99].

Although the DIC method provides a non-contact measurement of local strain distribution, the accuracy of the result is highly dependent on the quality of speckle patterns and the resolution of the image capture device. To minimise the image distortion and/or noise that might further affect the result, we employed two distinct cameras placed at an angle of 30° relative to the specimen surface to capture images for the 3D image correlation (Figure 2.8), which would enable a more reliable and accurate measurement of the local strains.

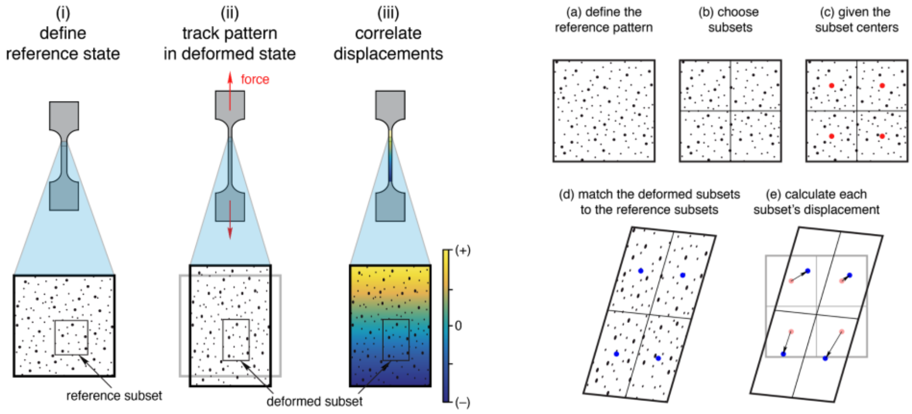

Figure 2.7 Schematic of the DIC technique, in which the local strain is calculated from the displacement of speckles in each subset [100]

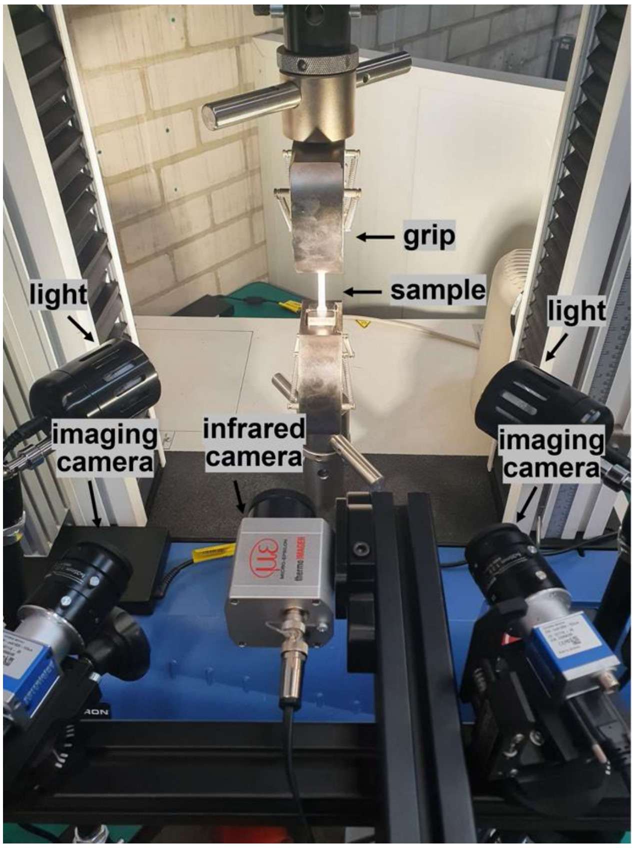

Figure 2.8 Experimental setup of universal tensile testing with DIC and infrared cameras

Post-processing and correlating the images to digital data requires significant computational power and specialised software. Hence the VIC-3D system was used throughout the measurement for calibration, image capturing, and strain data calculation. The calculated data was then imported to Matlab for the convenience of generating plots and cross-comparing with infrared temperature measurement and tensile stress-strain curve. The Matlab code is presented in Appendix A.1.

The introduction of speckle patterns on the surface is required for the DIC experiment. In our experiment, the tensile sample was polished up to P4000 SiC paper. After measuring the thickness and width of the cross-section, the white base coat was sprayed to the surface perpendicular to the normal direction. Until the base coat was dried, the speckles were introduced to the sample surface by a stamp rocker with the finest dot size (0.18mm) to ensure better spatial resolution. Speckles were stamped several times so that the pattern on the surface was random (Figure 2.9). After the speckles had dried, the sample could be used for the tensile test with DIC measurement.

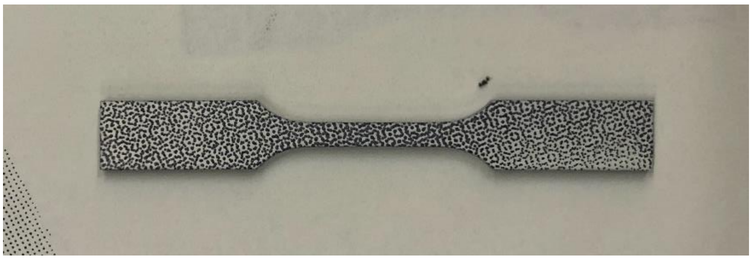

Figure 2.9 Sample surface after applying speckle pattern

2.4.2 Infrared camera temperature measurement

During deformation, part of the mechanical energy exerted on the tensile sample was dissipated to thermal energy, leading to the temperature elevation. Thus, monitoring the temperature evolution during the tensile test could capture the localised deformation and provide unique insights into the features of the propagating band. Herein, temperature data were measured and recorded by the infrared camera thermoIMAGER 160, which was placed perpendicular to the normal surface of the specimen on a tripod stand (Figure 2.8).

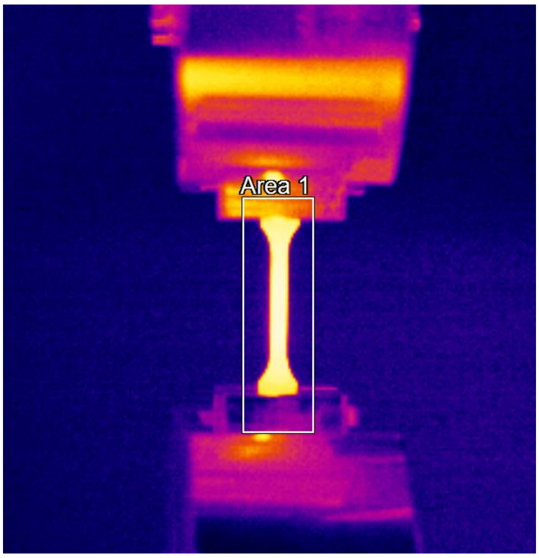

Figure 2.10 Visualisation of temperature measurement on the surface of specimen

The temperature scanning frequency was adjusted according to different strain rates, in which 25 Hz was used in the 1x10^{-1} s^{-1} and 1x10^{-2} s^{-1} strain rate test, 5 Hz was used in the 1x10^{-3} s^{-1} strain rate test, and 1Hz was used in 5x10^{--5} s^{-1} strain rate test. Temperature evolutions were recorded in a RAVI video format, and a rectangular profile was drawn to extract the temperature reading on the specimen surface (Figure 2.10), with 68×14 data points covering the entire sample. The extracted temperature data was post-processed by Matlab for further analysis, and the code is presented in Appendix A.2.

Chapter 3 Mechanical properties and microstructural characterisation

3.1 Overview

Advanced high-strength steels are imperatively needed to address the current and emerging industrial applications that are imposing increasingly demanding property requirements. In this study, we fabricated a medium Mn steel with a chemical composition of Fe-12Mn-0.35C-2Al-0.4V-0.8Mo (in weight percentage), exhibiting an excellent combination of yield strength, ultimate tensile strength, and ductility. In addition, unlike other advanced medium Mn steels that were fabricated via sophisticated processes, such as long-term intercritical annealing, the current steel was manufactured more effectively without involving the process of intercritical annealing, making our steel more sustainable and cost-effective. In this chapter, the mechanical properties of the current studied steel were examined by various mechanical tests, its microstructural traits were systematically characterised, and the reasons for how this steel achieved such performance will be extensively discussed in this section from both macro and microscopic perspectives.

3.2 Tensile stress-strain curve

The typical engineering stress-strain curve was obtained by universal tensile testing with the engineering strain measured directly from the extensometer, and the engineering stress was calculated by dividing the force by the cross-sectional area of the specimen. Figure 3.1 presents the tensile properties of the studied steel at a constant crosshead speed of 1 mm/min, which can be converted to about 1×10^{-3} s^{-1} in strain rate. As illustrated in Figure 3.1, the yield strength of the studied steel reached 1149±12 MPa, at the engineering strain of 1.4% in the elastic deformation regime. After yielding, the steel experienced a yield drop of about 60 MPa, followed by around 10% yield point elongation, which is also known as the Lüder strain, where a localised deformation band (Lüder band) propagates along the tensile direction of the specimen while the engineering stress nearly keeps constant during the propagation of Lüder bands. The work-hardening stage starts as soon as the Lüder band finishes propagating. During this stage, the elongation and strength of the tensile specimen increased until it reached the ultimate tensile strength and uniform elongation of 1605±26 MPa and 29.5±2.6%, noting that uniform elongation of the studied steel is also the total elongation, in which necking was not observed. The elastic modulus of the sample was measured as 146 GPa by linearly fitting the elastic deformation regime on the stress-strain curve. Stress serrations were observed from the yield point elongation regime and work-hardening regime, representing the widely reported plastic instability phenomena. The current studied steel experienced superior mechanical properties compared to the other medium Mn steels reported by other studies [5, 17, 19, 21, 39, 41-43, 45, 101-103]. The mechanical properties were benchmarked and plotted in Figure 3.3.

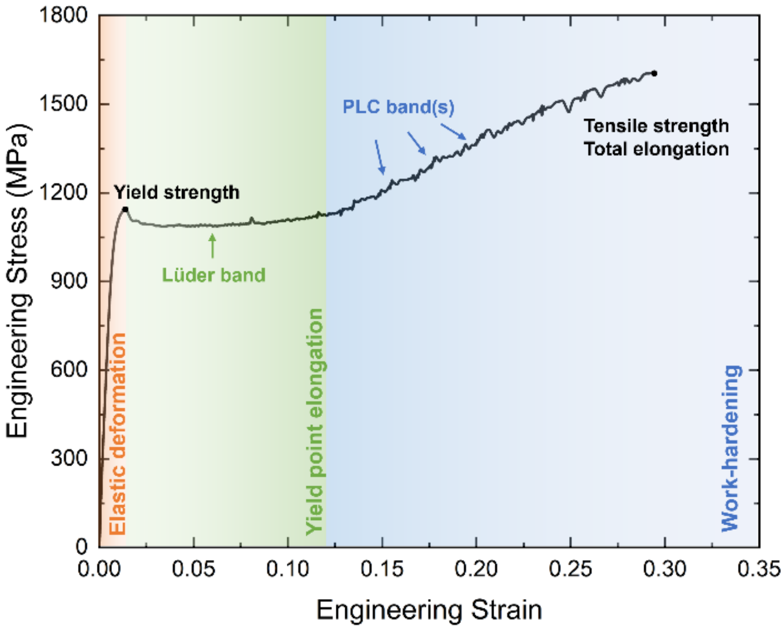

Figure 3.1 Engineering stress-strain curve obtained from universal tensile testing at a strain rate of 1×10^{-3}s^{-1}

Figure 3.2a shows the yield strength verse uniform elongation of medium Mn steels studied by other researchers. While the uniform elongation of our steel exhibits an intermediate uniform elongation, a relatively high value of yield strength was obtained compared to others. A similar trend was obtained from the product of tensile strength verse uniform elongation graph (Figure 3.2b). In fact, if we set the benchmark of tensile strength to be about 1400 MPa, the current steel demonstrates superior ductility.

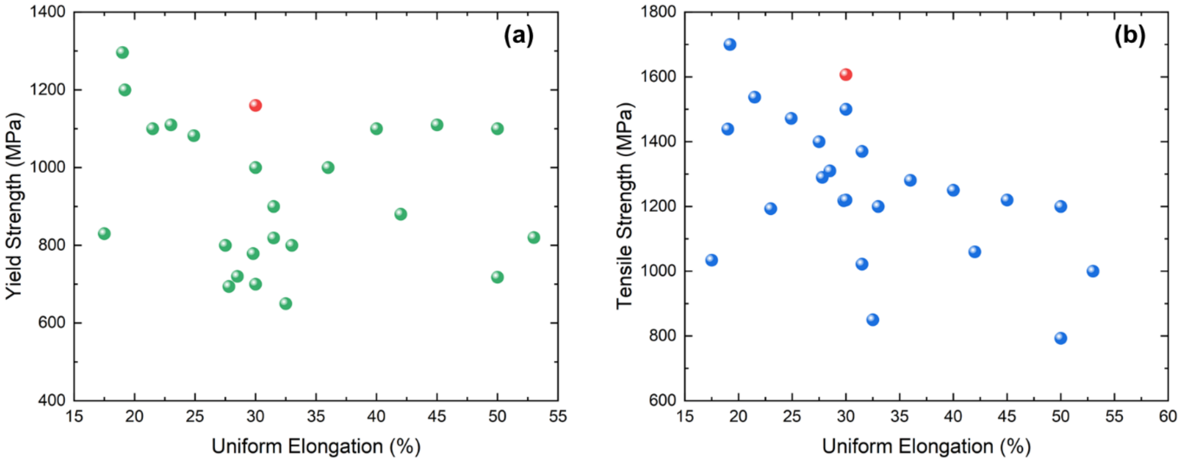

Figure 3.2 Benchmark of (a) yield strength and (b) ultimate tensile strength verse uniform elongation of medium Mn steel. Symbol coloured in red represent the current studied steel [5, 17, 19, 21, 39, 41-43, 45, 101-103]

Most of the medium Mn steels investigated previously by other researchers faced a common problem that it was difficult to achieve a good combination of yield strength, tensile strength, and uniform elongation. Most of the studies show medium Mn steels with relatively high yield strength and uniform elongation. However, the work-hardening stage is almost absent, with relatively low tensile strength. For the current study steel, we achieved a superior combination without compromising any of the three critical mechanical properties compared to the counterparts, as illustrated in Figure 3.2 and Figure 3.3.

While the engineering stress-strain curve illustrated the strengths and ductility, the true stress-strain displayed the work-hardening ability of the material. Figure 3.4a showed the true stress-strain curve calculated from the engineering stress-strain curve. A noticeable work-hardening response can be found after the yield point elongation region. The true stress reached ~2000

MPa with a true strain of ~26%. The work-hardening rate was calculated by taking the derivative of the true stress-strain curve, and the result was plotted in Figure 3.4b. Numerous deformation peaks were exhibited after the true strain >10%, indicating the occurrence of plastic instability. Despite this, the current steel exhibited an exceptional work-hardening ability which increases the true stress from ~1250 to more than 2000 MPa, and reasons will be elaborated in subsequent sections.

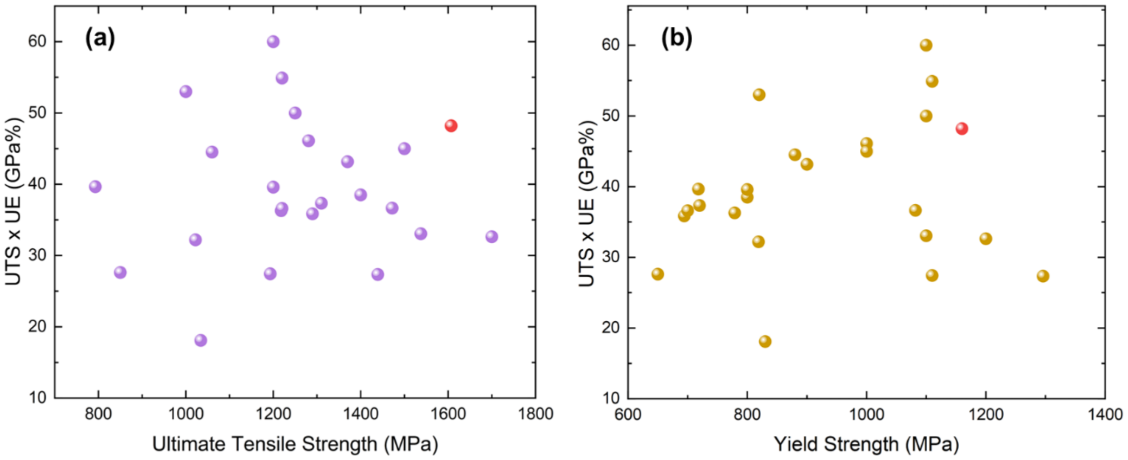

Figure 3.3 Benchmark of the product of ultimate tensile strength and uniform elongation verse (a) ultimate tensile strength (b) yield strength of medium Mn steel. Symbol coloured in red represent the current studied steel [5, 17, 19, 21, 39, 41-43, 45, 101-103]

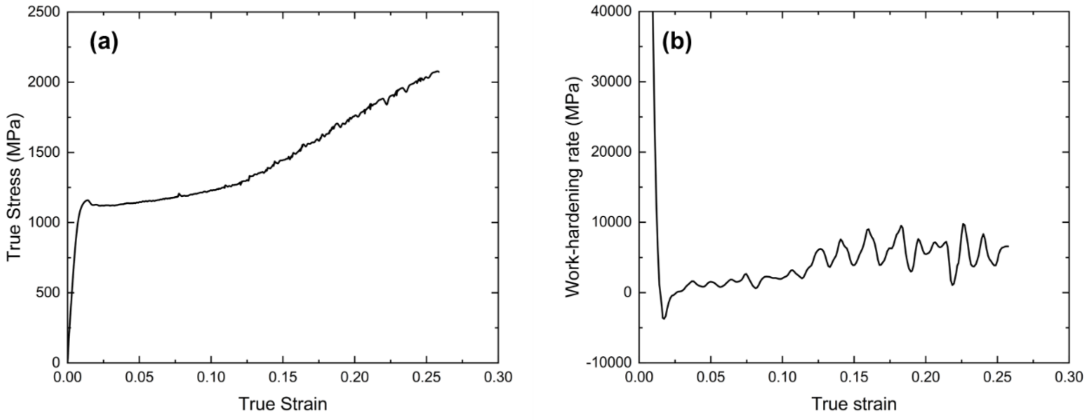

Figure 3.4 (a) True stress-strain curve and (b) work-hardening rate of the current studied steel obtained from universal tensile testing at a strain rate of 1×10^{-3}s^{-1}

3.3 Local nanohardness

The measurements of local hardness obtained from the nanoindentation test were post-processed in Matlab and combined with the EBSD phase mapping result. Moreover, the nanohardness was categorised by the type of phase, as shown in Figure 3.5. The full austenite and full martensite label indicate that the measurement was taken purely from the corresponding phase. Major austenite and major martensite denote that the indenter covered most of the related phase with an embedded second phase. The remaining category means that the nanohardness was measured at a point where the fractions of both are approximately equal (i.e., phase boundary).

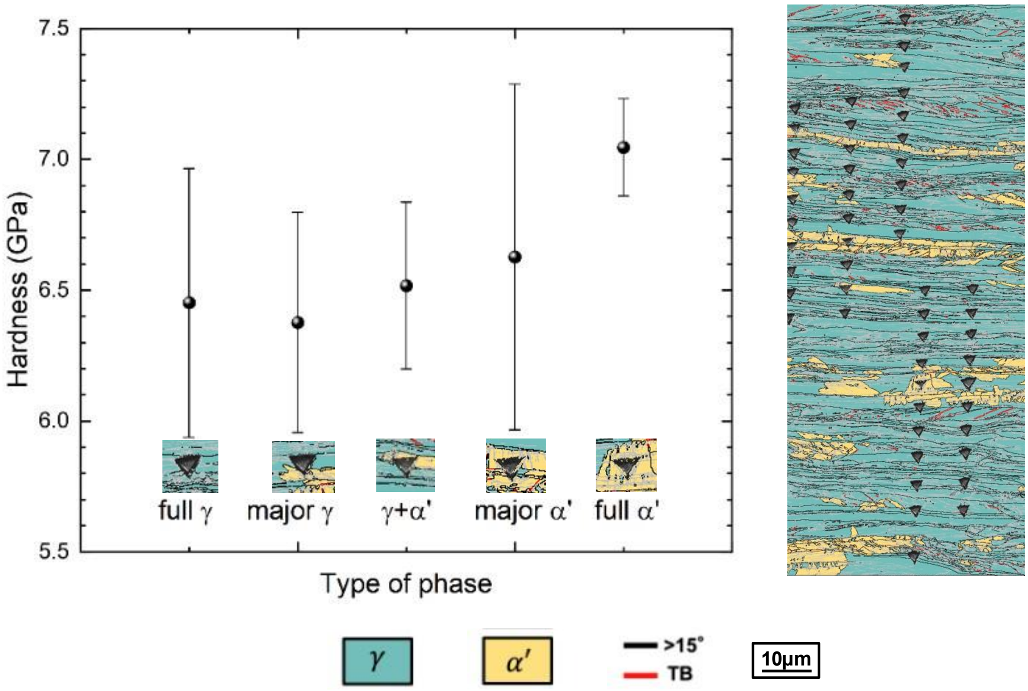

Figure 3.5 The hardness of phases obtained using UMIS nanoindentation system with a Berkovich tip

The results demonstrate that the hardness of all phases is in-between the range of 6.5 ± 0.7 GPa, while the hardness of martensite is slightly higher than those of other categories, with an average value of 7 ± 0.2 GPa. This provides evidence that the BCC phase detected by EBSD is the BCT martensite phase since the average hardness of BCC ferrite reported by others is

3.6±0.5 GPa [57, 58, 84]. The elevated hardness of BCT martensite might have resulted from the large amount of dislocation stored in the grains.

3.4 Microstructures before deformation

Three types of microstructural features could be readily extracted from EBSD mapping. Phase mapping illustrates the phase content, phase fraction, grain morphology, and grain size (Figure 3.6a). A large fraction of austenite is retained after the quenching process due to the addition of a large amount of austenite stabilizer (Mn). The fraction of austenite is measured to be 84.3 ± 3.5% and coloured in aqua in Figure 3.6a. Martensite was embedded into the matrix austenite with a fraction of 15.7% (coloured in yellow), and with a layered structure. Twin boundaries were overlayed on the phase map to illustrate the distribution of twins in grains. A large number of twinned grains displayed within the austenite phase might have resulted from the warm rolling process. From the inverse pole figure on the z-axis (IPF-Z) orientation mapping shown in Figure 3.6b, large and elongated austenite grains with a high aspect ratio (defined by the length over the width) can be readily identified. A statistical study on counting the number of grains with different aspect ratios is shown in Figure 3.7. It could be seen that there are large amounts of austenite grains with a large aspect ratio, matching the observation in the image. Local misorientation mapping (Figure 3.6b) shows that the dislocation density in both phases is high, which is caused by the warm rolling process without annealing.

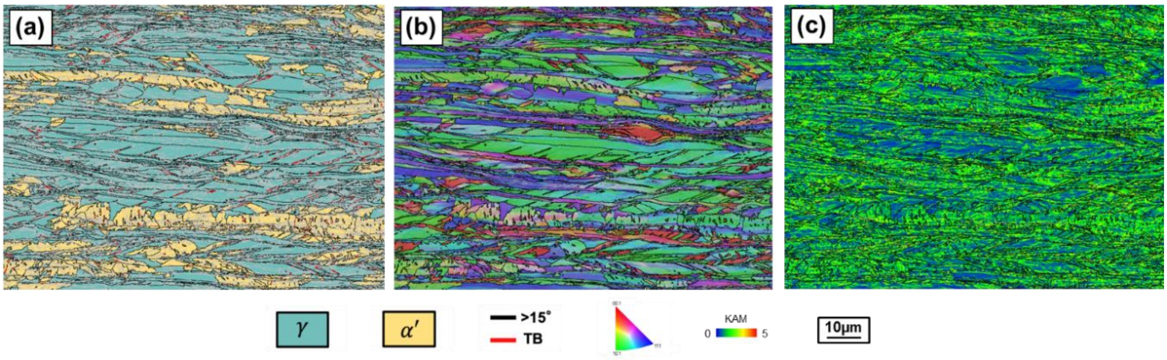

Figure 3.6 Initial microstructure of 35-WR-LN before deformation. (a) EBSD phase map, (b) IPF-Z orientation map, (c) Local misorientation map

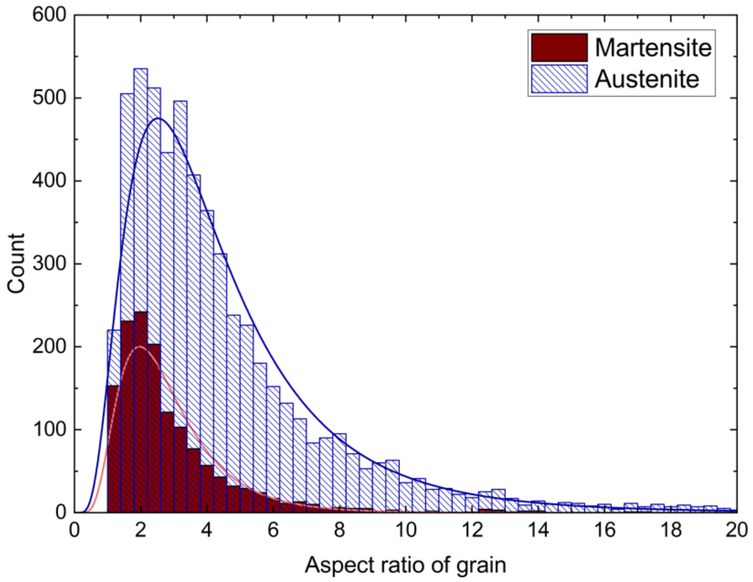

Figure 3.7 Histogram count on grains with respect to their aspect ratio in the initial microstructure

To further investigate the microstructures at a finer scale, TEM was applied to characterise the typical microstructural features. As exhibited in Figure 3.8, the elongated grain morphology can be the signature of the overall microstructure, which can be attributed to the massive warm rolling processes. Twinned grains were found frequently in FCC austenite and can be confirmed by the mirroring diffraction pattern along the FCC [011] zone axis. In addition, vanadium carbide precipitates with a diameter of ~100nm scatter within the austenite phase, as confirmed by the electron diffraction pattern with a shorter lattice parameter along the FCC [011] zone axis (Figure 3.9).

The typical embedded BCT martensite grains were revealed under TEM, as shown in Figure 3.10. Due to the limited resolution of TEM, the difference in the lattice parameter on the c-axis could not be easily distinguished. In addition, the dislocation densities in both phases are quite high. It should be noted that the corrosion rate of the austenite phase during electropolishing for the preparation of TEM samples is much faster than that of martensite. Therefore, the region with martensite seems to be much darker than the austenitic area, which can be due to the relatively large thickness.

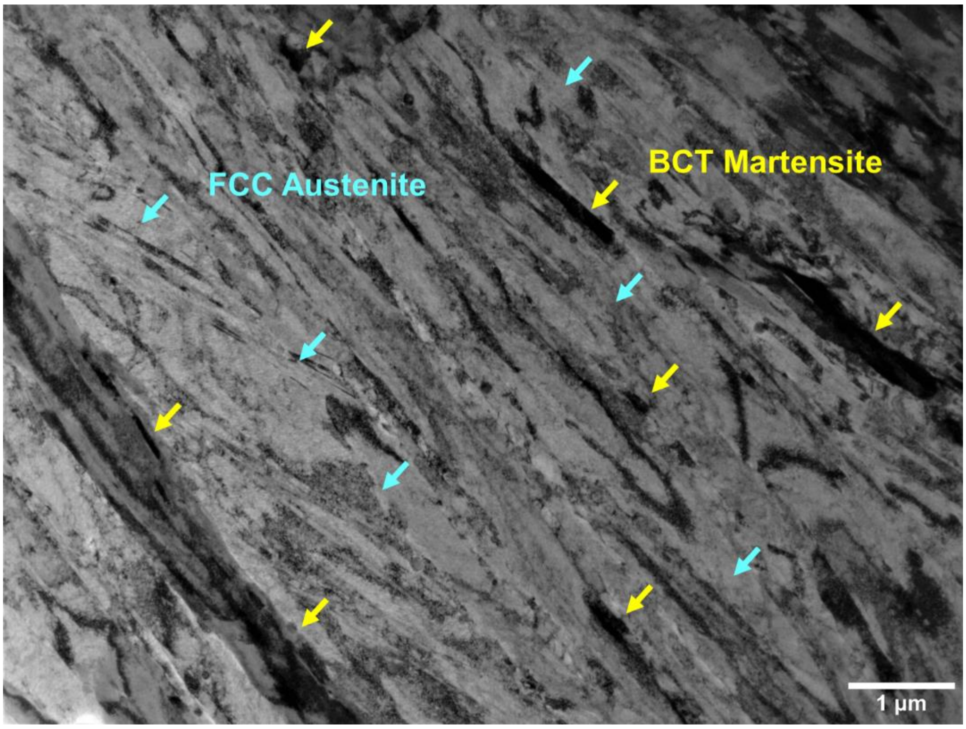

Figure 3.8 TEM image of microstructure prior to deformation

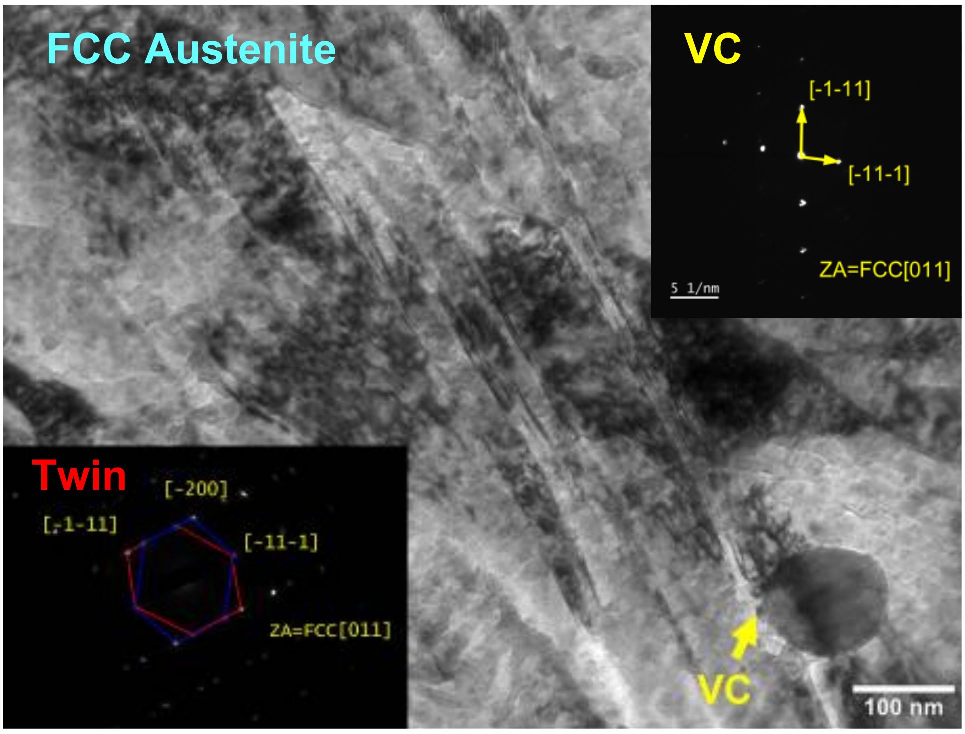

Figure 3.9 TEM image of zoomed twin structure and vanadium carbide precipitate (more TEM image in Appendix A.3)

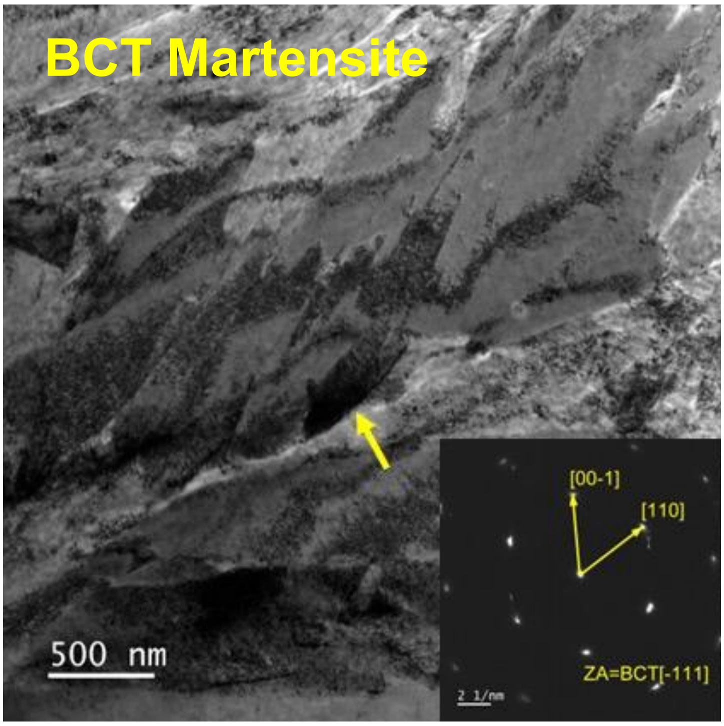

Figure 3.10 TEM image of BCT martensite in the microstructure before deformation

3.5 Microstructures after deformation and fracture surface

The typical microstructures of the steel after deformation were also characterised by using EBSD mapping, as shown in Figure 3.11. The phase map indicates that a large amount of austenite had transformed into martensite. Around 65% of originally retained austenite transformed, resulting in only 29.2±7.8% of austenite remained and 73.8% of fresh martensite formed after deformation. The twin boundaries that appeared in the initial microstructures could be barely detected in the final microstructure after fractured. In fact, it was found that twin boundaries acted as preferential martensite nucleation sites. IPF-Z orientation map shows that most of the elongated austenite grains had turned into relatively equiaxed martensite grains, as confirmed by the statistical count on grains regard to the aspect ratio. The volume fraction of martensite grains increases significantly, with most grains having an aspect ratio of less than 4. The local misorientation map indicates that the dislocation density also increases, and the dislocation distribution is more homogeneous compared with the microstructure before deformation, which is probably due to the martensitic transformation and the associated refinement in grain size promoting the dislocation multiplication.

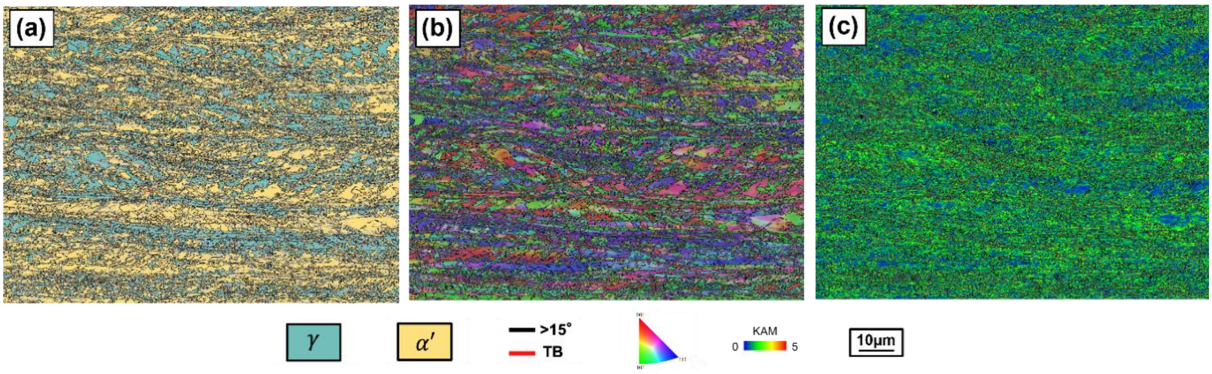

Figure 3.11 Final microstructure of 35-WR-LN after fracture. (a) EBSD phase map, (b) IPF-Z orientation map, (c) Local misorientation map

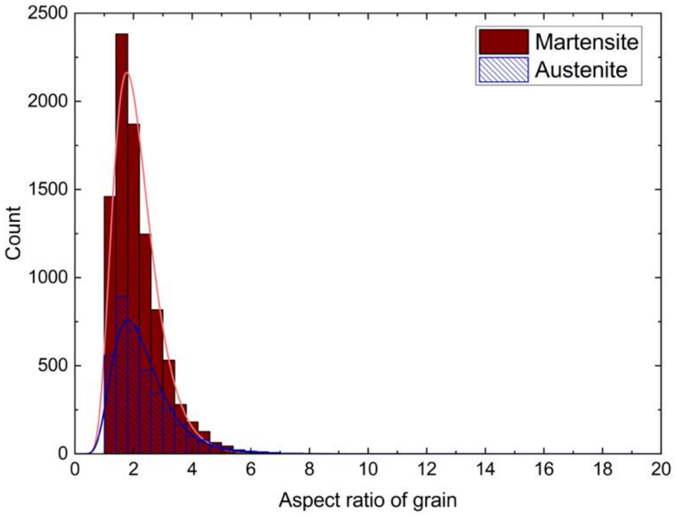

Figure 3.12 Histogram count on grains with respect to their aspect ratio in the final microstructure

TEM images of the tensile deformed sample are shown in Figure 3.13. Apparently, the phase transformation from austenite to martensite occurred extensively, making the martensite become the main microstructural feature. In addition, excessive dislocation can be evidenced through the strong contrast (as indicated by the arrows in Figure 3.13b). Slip bands were found at a roughly 45-degree angle to the elongated direction (as indicated by the arrows in Figure 3.13a).

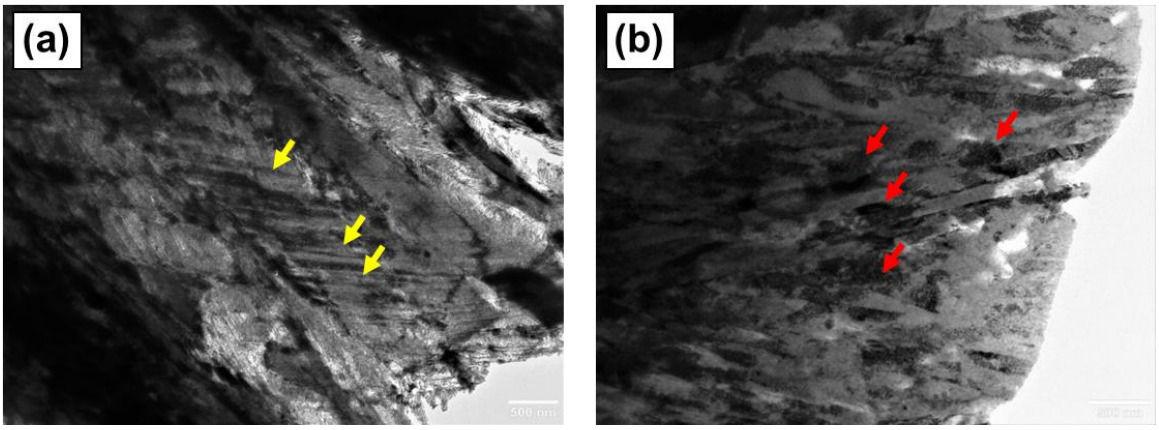

Figure 3.13 TEM image of present steel after deformation

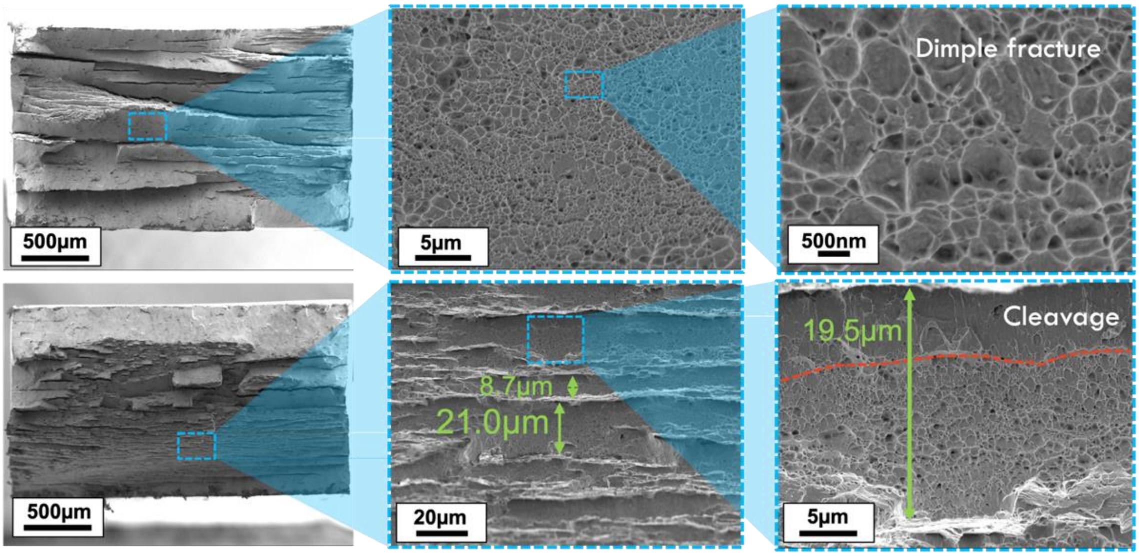

Figure 3.14 Fractography of the current studied steel deformed at 1×10^{-3}s^{-1}

In addition, the topography of the fracture surface was studied by SEM, as shown in Figure 3.14. The fractography features both fine and coarse delaminated layers, a thickness of around tens of microns. The delaminated layers are reported to be caused by the strength anisotropy between the longitudinal and transverse directions of the sample [5]. For the coarse layer, dimple-type fracture distributes homogeneously, whereas, for the fine layer, quasi-cleavage fracture could be observed in the region near the edge of the layer.

3.6 Phase transformation

The EBSD study has clearly demonstrated robust evidence of change in phase fraction before and after deformation, suggesting that the stress-induced martensitic phase transformation governs plastic deformation. However, the behaviour and kinematics of phase transformation could not be elucidated directly from EBSD studies alone. Therefore, we applied multiple *in-situ and ex-situ* characterisation techniques to track and examine the detailed processes of phase transformation.

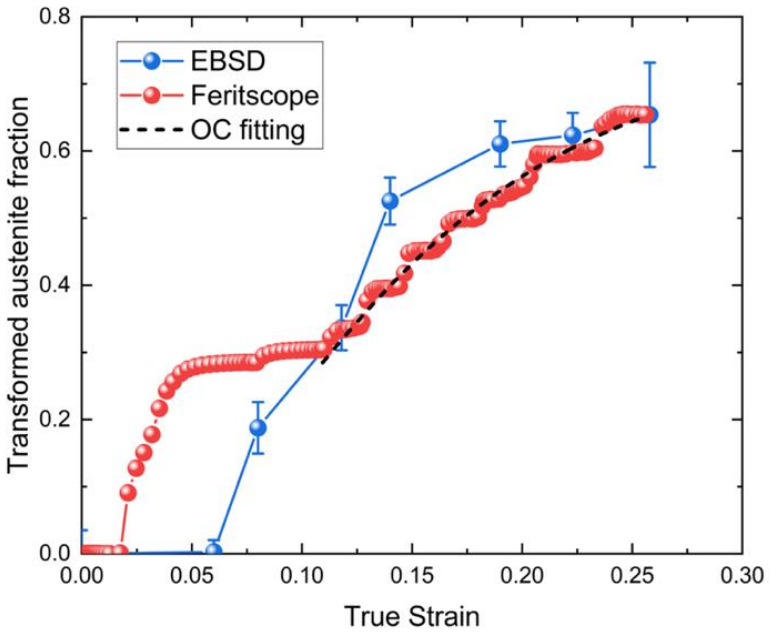

Figure 3.15 Transformed austenite fraction at 1×10^{-3}s^{-1} measured by Feritscope and calibrated by EBSD data

During the tensile deformation, Feritscope was implemented on the surface of the specimen to measure the real-time content of magnetic material. The passage of either the Lüder bands or the PLC bands will lead to the increase in the magnetic content due to the freshly transformed martensite causing the measurement on Feritscope to increase as well. Noting that the detection region of Feritscope can be treated as a point detection, which could measure the change in local magnetic content, and since both the Lüder band and PLC bands were propagating in a specific direction on the gauge section, the change in magnetic content may not be observed at an identical strain among all experiments. Therefore, the Feritscope could represent the change in the transformed austenite fraction well. However, it fails to represent the strain distribution over the entire sample.

By normalising the final austenite content of the fractured sample with data obtained from EBSD (Figure 3.16), the transformed austenite fraction during deformation was converted and plotted in Figure 3.15. Austenite transformed in a step-like manner, which could be related to the passing of the Lüder band and PLC bands [25], with the largest increase obtained in the Lüder band region of around 50% of martensitic transformation. The Olson-Cohen model of martensitic transformation was fitted to the curve of the work-hardening stage obtained by the Feritcope, and the associated variables α and β will be discussed. The Olson-Cohen model is illustrated below:

$$f^{\alpha'} = 1 - \exp\{-\beta p[1 - \exp(-\alpha\epsilon)]^n\} \tag{3.1}$$

To quantitatively reveal the plastic deformation mechanism involved in phase transformation, we have conducted EBSD studies on the interrupted tensile samples that were elongated to 6%, 12%, 15%, 20% and 25%, respectively, as shown in Figure 3.16. An extensive amount of twin boundaries (marked in red) could be seen in the 6% pre-Lüder band region (Figure 3.16a). After the passage of the Lüder band (Figure 3.16b), most of the twin grains have transformed to martensite already with a 45° angle off the rolling direction. Phase contents at different stages of interrupted tensile samples have been quantified and plotted in Figure 3.15. The curve obtained from EBSD roughly matches the data obtained by Feritscope.

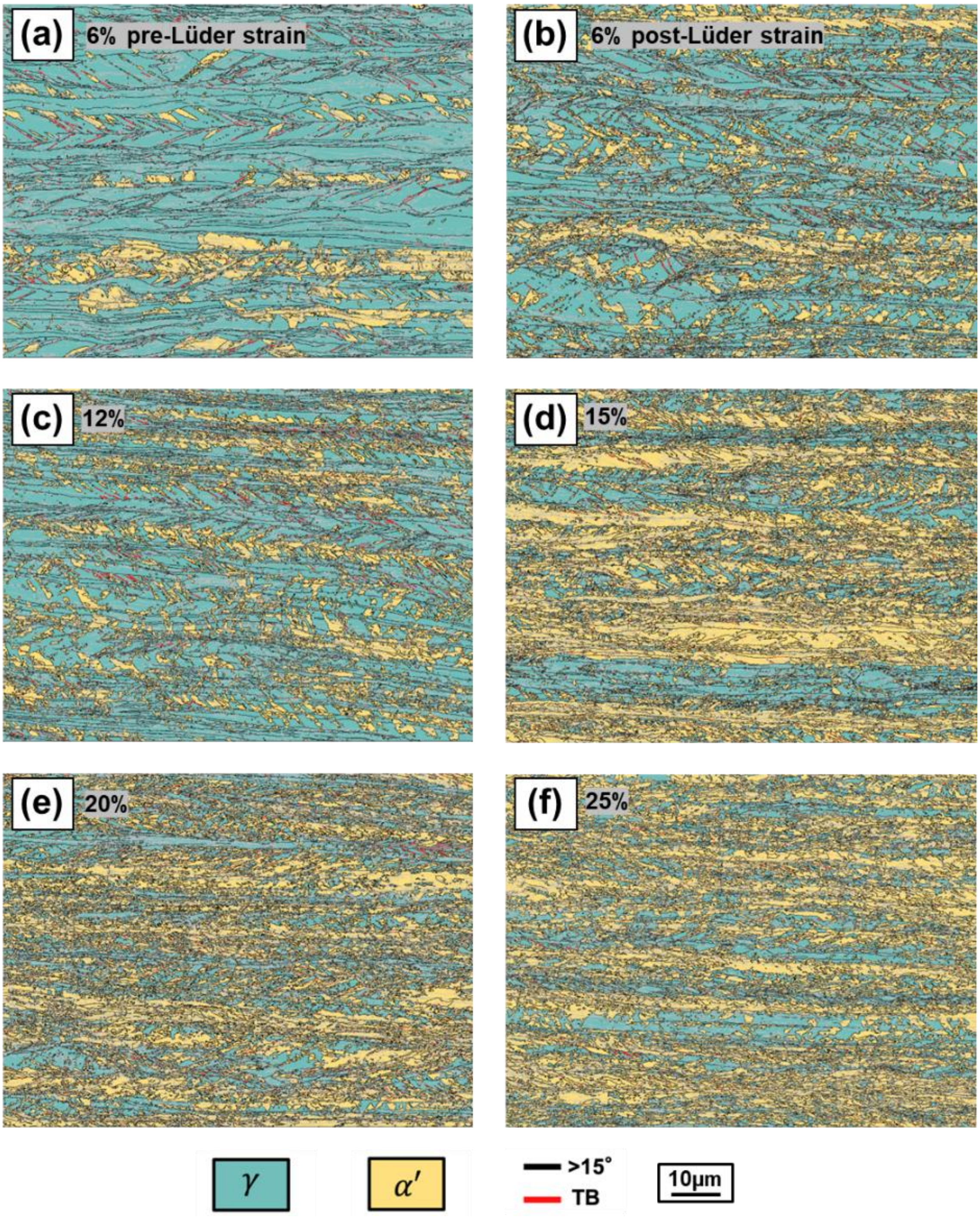

Figure 3.16 EBSD Phase mapping of the interrupted tensile 35-WR-LN sample at a strain rate of $1\times10^{-3}s^{-1}$. (a) 6% pre-Lüder strain, (b) 6% post-Lüder strain, (c)12%, (d) 15%, (e)20%, and (f) 25%.

3.7 Discussion

The current studied steel exhibits a remarkable yield strength among its counterparts as shown in Figure 3.2a, despite having a large amount of austenite phase in the initial microstructure which is known for lowering the overall yield strength. The high yield strength is likely due to the dislocation strengthening, precipitate strengthening effects and martensite that co-existed in the current steel. Precipitate strengthening is achieved by the addition of alloying element V, which promotes the formation of Vanadium Carbide [17]. Another benefit of Vanadium Carbide is that it suppressed the recrystallization of austenite, leaving the austenite grains with a large aspect ratio after the warm rolling process, which introduced tremendous work-hardening ability [17]. Since recrystallization of austenite is suppressed during warm rolling, the resulting dislocation density in austenite increases in order to accommodate the deformation, as illustrated from the local misorientation map Figure 3.6c. Austenite with high dislocation density also contributes to the remarkable yield strength [17]. Rapid quenching to cryogenic temperature transformed a fraction of the austenite into martensite. Therefore, the athermal martensite is also responsible for the superior yield strength due to the high density of mobile dislocation within the microstructure [104].

A special heat treatment process, namely, intercritical annealing, was generally applied to tune the microstructures, phase fraction, and stability of austenite during the fabrication of conventional medium Mn steels reported previously [12, 36]. This process involves heating the steel to an elevated temperature for a prolonged time, which allows the segregation of Mn and other stabilising elements to austenite [104]. The duration ranges from several minutes to hours [1, 12, 105], consuming a significant amount of energy. Therefore, the warm rolling process was invented, in which the rolling an intercritical annealing process was combined, making the manufacturing more cost-effective. Due to the high temperature in the intercritical annealing process, the recrystallization of austenite was promoted, which tends to form an equiaxed grain morphology after cooling [5]. The sizes of the equiaxed grains can be controlled by the intercritical annealing temperature and duration [5, 19]. According to the Hall-Petch relationship, refining the grain size can improve the yield strength to some extent, but the ductility is compromised due to a lack of work-hardening ability [106]. For current warm-rolled steel, on the other hand, the yield strength is attributed to the dislocation in martensite and austenite and the existence of embedded Vanadium carbide precipitates. Noting that a large number of twins were also found in the initial microstructure Figure 3.6, which might contribute to the yield strength to some extent.

Since intercritical annealing was not applied in the current steel, the recrystallization of austenite was suppressed. Austenite grains underwent a warm rolling process, resulting in an elongated shape with a large aspect ratio (Figure 3.7) and high density of dislocations also retained. After the stress passed the macroscopic yielding point, the current steel did not start the work-hardening immediately, instead, the Lüder band initiated, representing the so-called yield point elongation. In this process, the plastic strain increased, but the flow stress stayed relatively constant. From the microstructural perspective, a fraction of the austenite phase transformed into martensite within the Lüder band (Figure 3.16a and b). Whether the localised transformation is the cause, or the result of localised strain has not been proven. Wang et al. [46] and Sun et al. [25] pointed out that a strong correlation between martensitic phase transformation and localised Lüder strain was found, but both of them can exist independently from the other. In our case, 50% of the phase transformation was found within the yield point elongation regime. The elongated austenite grains with a large aspect ratio provided enough space for shear band formation [17], which acts as a preferential nucleation site for martensite. In addition, the large number of twins also act as a preferential site for martensite to form as illustrated in Figure 3.16. The combination of these two factors contributes to the significant amount of phase transformation during the yield point elongation.

Work-hardening start after the passage of Lüder strain over the entire gauge length. The contribution of the TRIP effect, i.e., the transformation of austenite to martensite, to the work hardening has been well-established [17, 45]. Half of the phase transformation has already occurred during the yield point elongation stage; the remaining is responsible for work-hardening. To sustain the work-hardening ability, we have carefully engineered the austenite stability of the current steel. By introducing the warm rolling, sufficient mobile dislocations remained in the microstructure, which also leads to the occurrence of austenite with different grain sizes. By doing so, the current studied steel achieves a maximum true stress of ~2000 MPa and a true strain of ~26%.

3.8 Summary

Results from the mechanical tests demonstrated that the present steel exhibited remarkable yield strength and work-hardening ability, attributing to the dislocation and precipitating strengthening, and the TRIP effect, respectively. However, the plastic instability phenomena were observed as well, which have been discovered in a wide range of medium Mn steels, especially those with significant work-hardening after yielding [17, 39, 45]. The work-hardening rate curve (Figure 3.4b) is reflected by the distinct peaks, representing the instability of plasticity. In the next section, the causes and the factor that would affect this phenomenon will be elaborated.

Chapter 4 Discontinuous yielding

4.1 Overview

Discontinuous yielding behaviour is a type of plastic instability, which has been widely found in many alloy systems such as Ni-base superalloy, Al-Mg alloy, and Fe-C alloy [107]. The materials will suffer from uneven sample surfaces induced by the discontinuous yielding phenomena during processing, which affects their physical appearance and mechanical properties [1, 107]. In medium Mn steel, this problem is also frequently reported [19, 25], but the underlying mechanism is yet to be properly understood. Previous studies showed that the strain rate and temperature could have a substantial influence on this plastic instability [38, 46, 107]. Therefore, the following section will show the experimental studies we have conducted to uncover the discontinuous yielding behaviour in the current medium Mn steel and provide unique insight on the underlying mechanism of this phenomenon.

4.2 Strain rate effect

Strain rate, reportedly, has a substantial effect on the yielding behaviour reflected on the tensile stress-strain curve [38, 46, 108]. Figure 4.1a presents the representative tensile stress-strain curves of the current material at various strain rates ranging from 10^{-1} s^{-1} to 10^{-5} s^{-1} (equivalent to 100 mm/min to 0.05 mm/min). The occurrence of yielding plateau and stress serration that can be due to the formation of the Lüder band and PLC bands, respectively, could be observed on all four curves whilst presenting different features. The yield strength is relatively independent of the strain rates with a constant value of ~1140 MPa, in contrast to the tensile strengths and elongations, which varied with the strain rates. The uniform elongation increased by ~36% from 0.22 to 0.30 by increasing the strain rate from 10^{-5} s^{-1} to 10^{-3} s^{-1}, and the tensile strength increased by 8% from 1480 MPa to the highest 1600 MPa. The total elongation further increased by another ~20% to 0.36 at the strain rate of 10^{-2} s^{-1}. The measured tensile strength stayed around the highest value of 1600 MPa. Further increasing the strain rate to 10^{-1} s^{-1}, the tensile strength experienced a decrease by 14% from 1600 MPa to 1370 MPa, and the total elongation approximately remained at 0.36. The global work-hardening rate decreased at a higher strain rate, and the frequency of stress serration was reduced (Figure 4.1a). The PLC effect was also presented during the work-hardening stage on all curves featured by the irregular serration at low strain rates of 10^{-5} s^{-1} and 10^{-3} s^{-1}, namely the Type A serration and the large step-like serration at higher strain rates of 10^{-2} s^{-1} and 10^{-1} s^{-1}, in which refers to as Type D serration [63]. Critical strain is defined as the strain where the stress serration starts to occur, often reported in Ni-based alloy systems. However, there is no sign of critical strain in all four stress-strain curves obtained from the current steel probably due to the presence of yield drop, in which the stress value had changed abruptly and could be counted as the first stress serration.

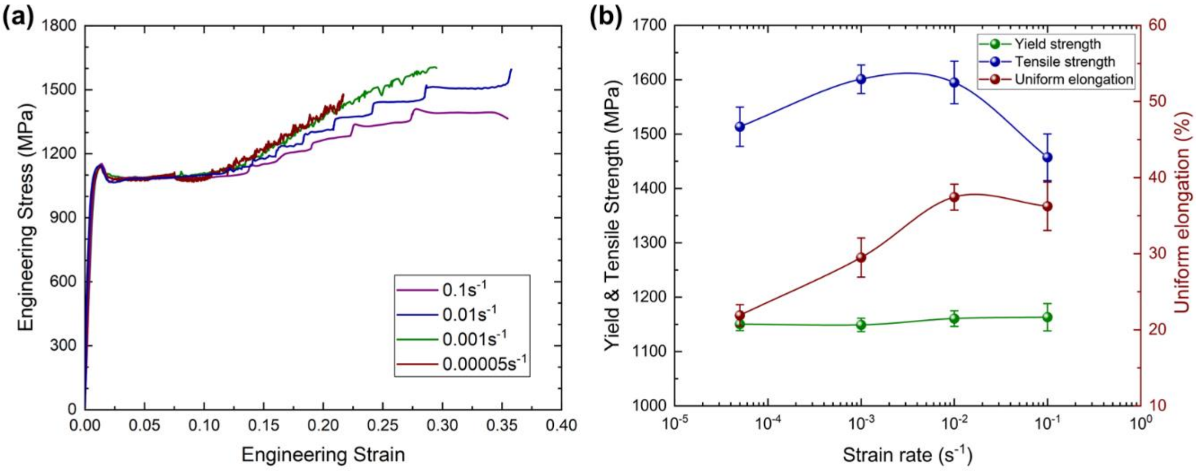

Figure 4.1 (a) Engineering stress-strain curve of 35-WR-LN deformed at different strain rates, and (b) Mechanical properties obtained from the curves

Comparing the work-hardening rate (Figure 4.2b), the sample tested at a slow strain rate featured more frequent stress fluctuation with smaller amplitude than those deformed at higher strain rates. Work-hardening behaviour of the samples strained at $10^{-5}s^{-1}$ and $10^{-3}s^{-1}$ were comparable, as observed from the stress-strain curve (Figure 4.1a) and work-hardening graph (Figure 4.2b), the rate of the work-hardening on the stress-strain curves are identical between this two strain rates. Further increasing the strain rate led to a decrease in this gradient, as presented by the higher strain rate samples. In addition, the work-hardening peaks at low strain rates were relatively constant (Figure 4.2b), whereas the peaks at high strain rates experienced steady growth (Figure 4.2b). Hence, the hypothesis is that the deformation behaviour and mechanical responses of the current studied steel were altered under different strain rates, which might also be the cause of the improvement in mechanical properties from low to high strain rate.

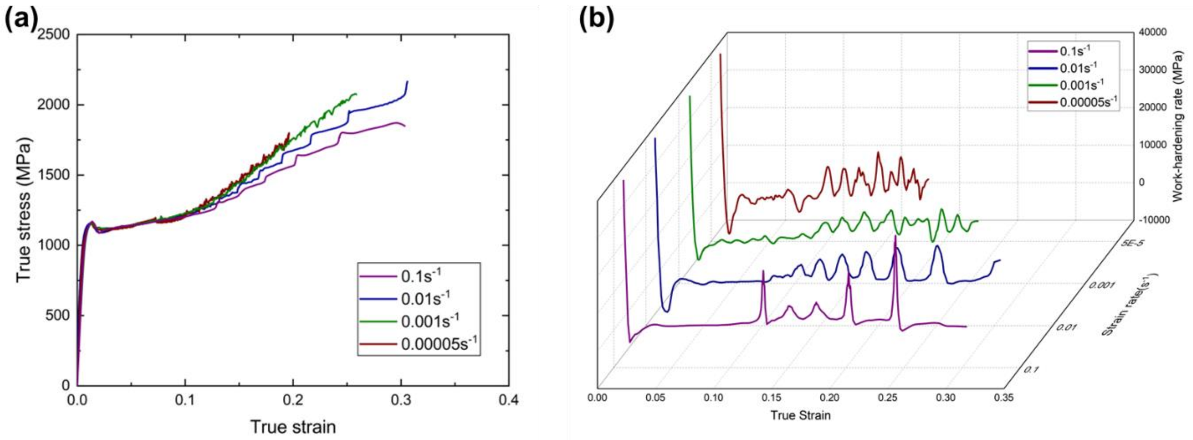

Figure 4.2 (a) Tensile true stress-strain curve of 35-WR-LN deformed at a range of strain rates, and (b) work-hardening rate calculated from true stress-strain curves.

It is well known that the TRIP effect played a predominant role in the tensile performance of medium Mn steels, and several investigations have indicated that the effects of strain rates on the transformation of austenite are prominent [38, 45]. To examine the phase transformation, the fractured samples under each strain rate were studied by EBSD phase mapping (Figure 4.3). Each sample had been mapped at least three times, and the results were average and plotted in Figure 4.4.

The transformed austenite fraction experienced a first increased trend from ~62% at the strain rate of 5×10^{-5} s^{-1} to ~75% at 1×10^{-2} s^{-1}, and then the fraction dropped back to ~60% at 1×10^{-2} s^{-1}. Despite that, the total elongation of the sample deformation at a strain rate of 1×10^{-1} s^{-1} presented a similar total elongation as the 1×10^{-2} s^{-1}. Less austenite had transformed during the deformation. This implied that the kinetics of phase transformation may be altered as the strain rate increases.

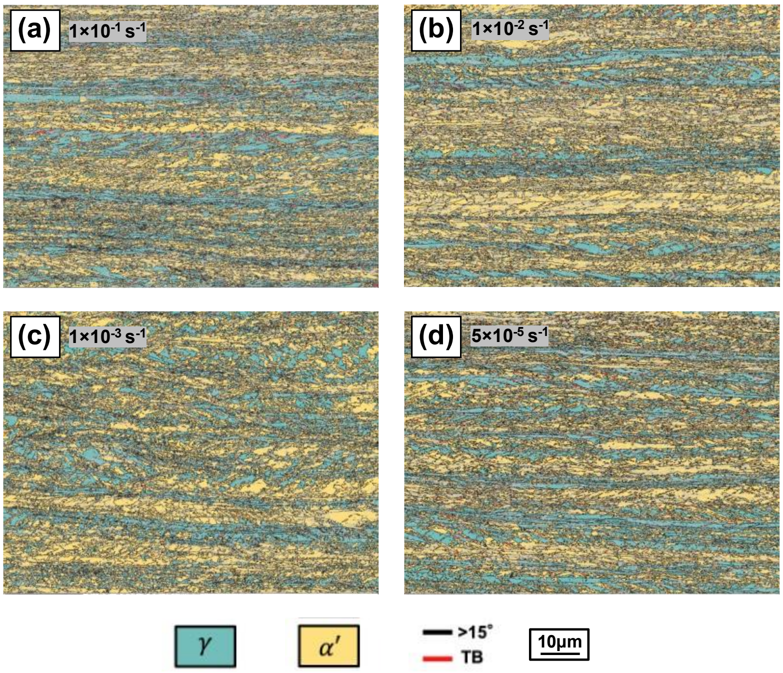

Figure 4.3 EBSD phase map of fractured 35-WR-LN under strain rate-of (a) 1×10^{-1} s^{-1}, (b) 1×10^{-2} s^{-1}, (c) 1×10^{-3} s^{-1} and (d) 5×10^{-5} s^{-1}

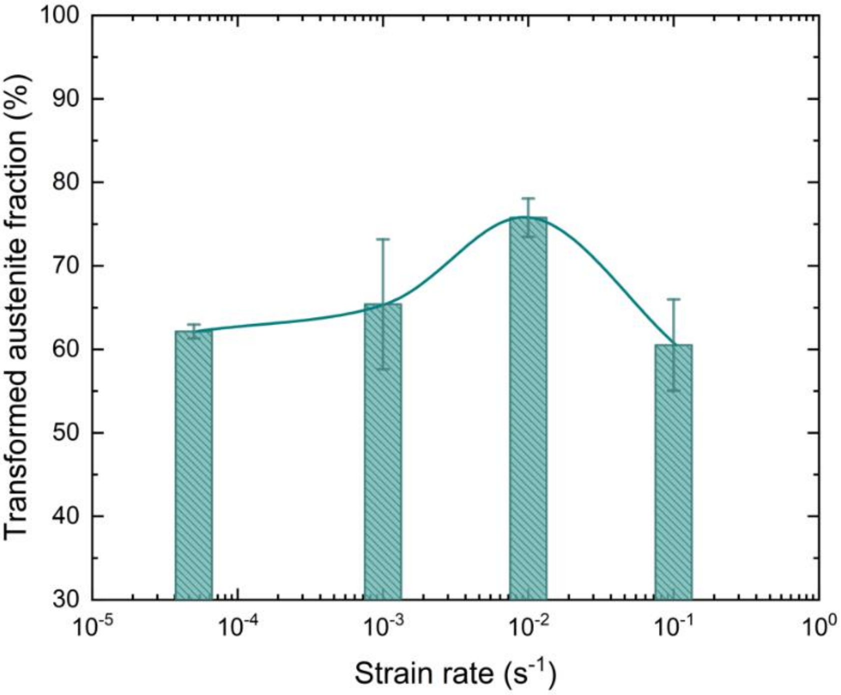

Figure 4.4 Final austenite phase fraction of fractured tensile sample

The Feritscope measurement provided convincing evidence of this phenomenon, as shown in Figure 4.5. The phase transformation tendency during the work-hardening stage was different among the applied strain rates. The deformation at the slowest strain rate exhibited a more rapid phase transformation among others, while the rate of phase transformation of the sample at the highest strain rate was the most sluggish. However, it should be noted that the sampling frequency of the Feritscope (5Hz) may limit the temporal resolution of the measurement.

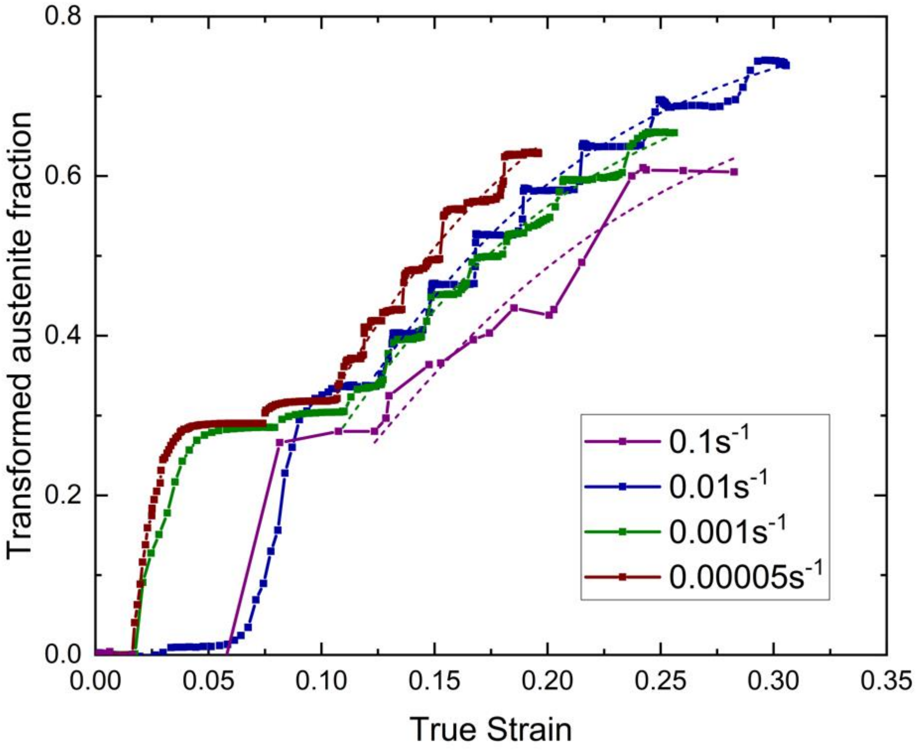

Figure 4.5 Transformed austenite fraction at a range of strain rates measured by Feritscope and calibrated by EBSD phase data obtained from the initial and fractured sample. Dotted curves fitted by the OC model.

The kinetics of phase transformation from austenite to martensite could be well characterised by the well-known Olson-Cohen model [34] with the formula shown in the equation below:

$$f^{\alpha'} = 1 - \exp\{-\beta[1 - \exp(-\alpha\epsilon)]^n\} \tag{4.1}$$

Where β and α are both temperature-dependent parameters [34]. The α is associated with the formation rate of shear band, which links to the SFE of materials and the applied strain rates

[26, 34]. The β is associated with the probability of phase transformation at the shear band intersection, which is highly pertinent to the chemical driving force [26, 34]. The parameter n is a material constant that depends on the chemical composition, and here $n = 3$ was found to give the best fitting of the curves at all applied strain rates. The β and α parameters obtained at different strain rates are shown in Figure 4.6. For the strain rate with the highest amount of phase transformation (1×10^{-2} s^{-1}), the α coefficient is the lowest, which means the rate of shear band formation rate is partially suppressed under the deformation in this strain rate. In contrast, parameter β for this strain rate is the highest, representing that the probability of phase transformation at shear band interception for this strain rate is the largest.

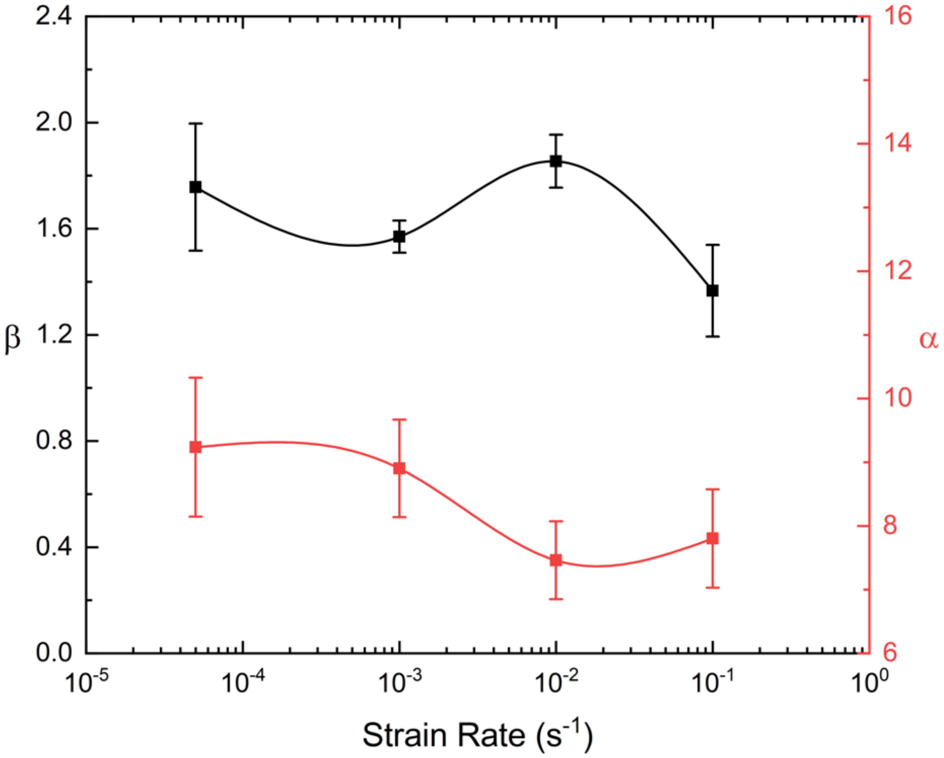

Figure 4.6 Parameters fitted from Olson-cohen phase transformation model [34]

The results from Feritscope indeed showed different phase transformation tendency under different strain rates, but to quantitatively study how the strain rate affect phase transformation, more advanced imaging techniques were required to provide the macroscopic and microscopic characterisations. Here, we employed in-situ DIC and infrared temperature detection methods to record the evolutions of local strain and temperature fields, respectively, during the formation, allowing us to further comprehend the discontinuous yielding phenomena.

4.3 Serrations in the stress-strain curves

Stress serration is one of the key features of discontinuous yielding phenomena, which is characterised by stress plateau, stress jump, and stress drop. These behaviours are closely related to the macro- and microstructure of the material. Figure 4.7 shows the magnified Lüder strain regime of the tensile stress-strain curves deformed at different strain rates. The curves obtained at low strain rates (1×10^{-3} s^{-1} and 5×10^{-5} s^{-1}) feature serrations with higher frequencies and amplitudes, in which a stress drop of 32 MPa at the strain of 7.5% was observed. Statistical Histograms (Figure 4.8) illustrate the events of stress change quantitatively. The stress drop event for the slowest strain rate test ($5\times10^{-5}s^{-1}$) was distributed in a wider range than the $1\times10^{-3}s^{-1}$ curve. A relatively large amount of stress change event experienced a magnitude between 15-20MPa, compared to the moderate strain rate ($1\times10^{-3}s^{-1}$), where most stress changes have a magnitude less than 5MPa. Serrations with constant stress jump and drop are often referred to as Type-B serration [63]. The stress-strain curve provides an overview of stress serration behaviour but fails to present the dynamic features corresponding to the propagating band. Therefore, we applied the DIC method to our experiment and correlated it with the tensile data.

A similar histogram was plotted (Figure 4.10) for the statistics of stress serrations in the work-hardening regime, which is known for the occurrence of PLC bands [25]. Noting that the stress serrations on the highest strain rate sample were insignificant with only the Type D band, the statistic of it was therefore not included. The slowest strain rate test featured the larger amount of stress serration events, with a magnitude higher among others. The stress-serration amplitude reached 50MPa, sharing similar values in the Lüder banding regime. Unlike the stress change distribution in the Lüder strain, the work-hardening stage presented a higher frequency of small stress drops (<5MPa). This indicated that fine changes in stress dominated the work-hardening stage of the present steel, and to investigate the characteristic of the PLC bands that created these stress serrations, a method with the direct and high-resolved method was applied, i.e., the DIC method including the strain and temperature mapping.

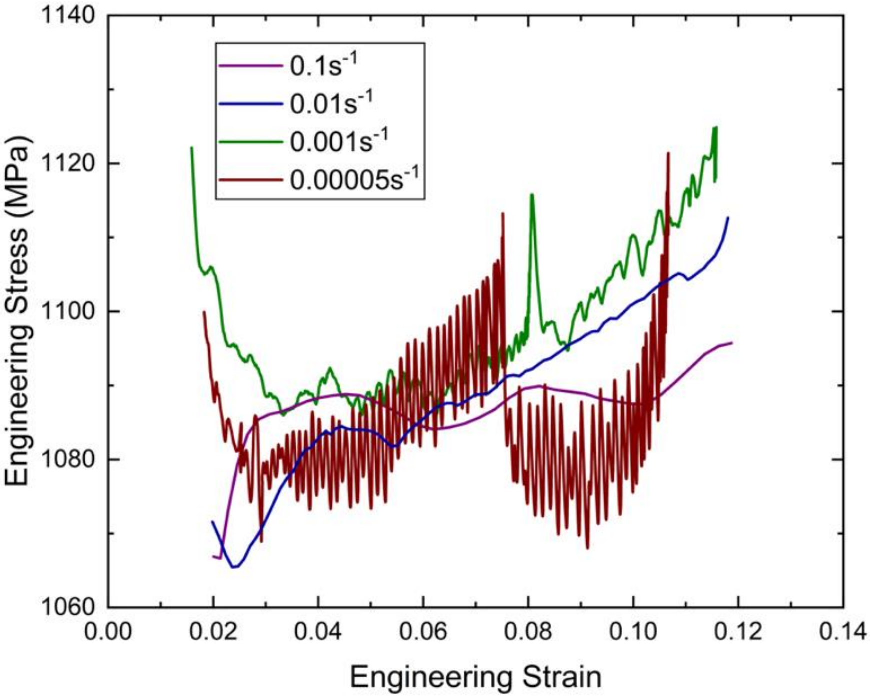

Figure 4.7 Magnified Lüder band regime of the stress-strain curve.

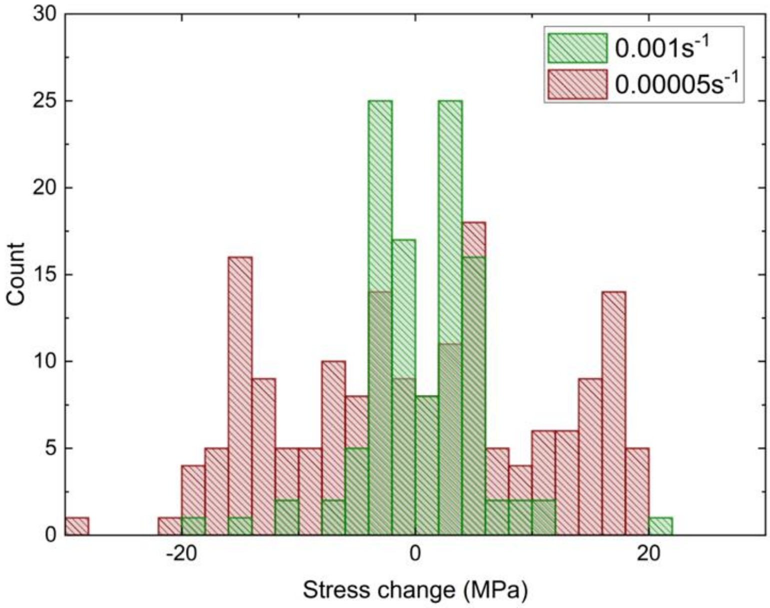

Figure 4.8 Histogram of the magnitude of stress serration event in the Lüder band regime

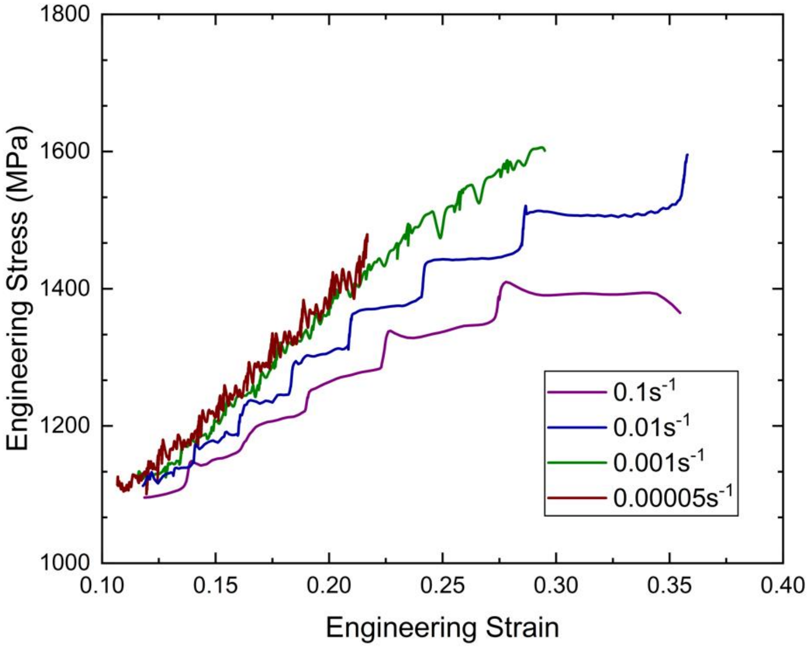

Figure 4.9 Magnified work-hardening regime of the stress-strain curve.

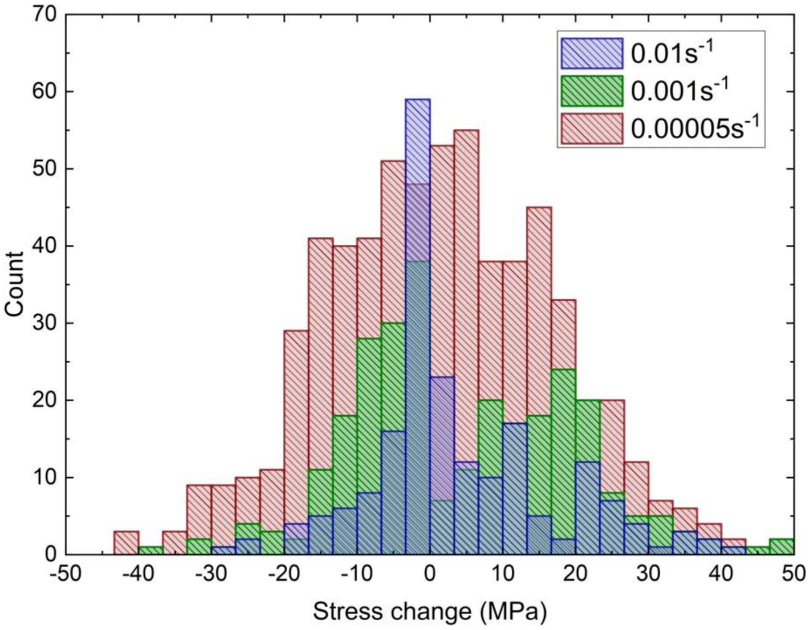

Figure 4.10 Histogram of stress serration event in work-hardening regime

4.4 In-situ observation

4.4.1 Digital image correlation

In present study, data obtained from the DIC were post-processed with Matlab. To illustrate the overview of strain evolution with time, the strain distribution along the tensile direction at the middle of the specimen at each time step was exported and plotted, as shown in Figure 4.11. Strain localisations can be reflected effectively by differentiating the strain with respect to each time increment, as shown in Figure 4.12. The propagation velocities of the Lüder band and PLC bands were calculated based on the position difference over time and labelled in the figures. The velocity of the propagating bands was different due to the variation in the applied strain rate; however, this effect could be eliminated by normalising the velocity with strain rates. The normalised velocities were plotted in Figure 4.13 with the x and y-axis representing strain rate and band velocity, respectively.

The propagation velocity of the Lüder bands was not identical to either the constant crosshead speed or the converted strain rate. In reality, they were moving at a velocity around 6-10 times faster than the constant crosshead. This implied that the material microstructure responded differently to the macroscopic input. Followed by the completion of Lüder band propagation, the work-hardening stage began, and multiple PLC bands initiated and propagated at 3-6 times faster velocity than the Lüder band. The normalised propagating velocity of the Lüder bands exhibits a decreasing trend to the applied strain rate in a roughly linear relationship (Figure 4.13), while the average velocity of PLC bands fluctuated with the applied strain rate. In fact, the propagating velocity of PLC bands varied with the strain as well. For example, at the strain rate of 1×10^{-1} s^{-1}, the strain rate decreases with the strain. The phenomenon might be caused by or resulted from the higher band strain, as illustrated in Figure 4.14. This will be discussed in the following section.

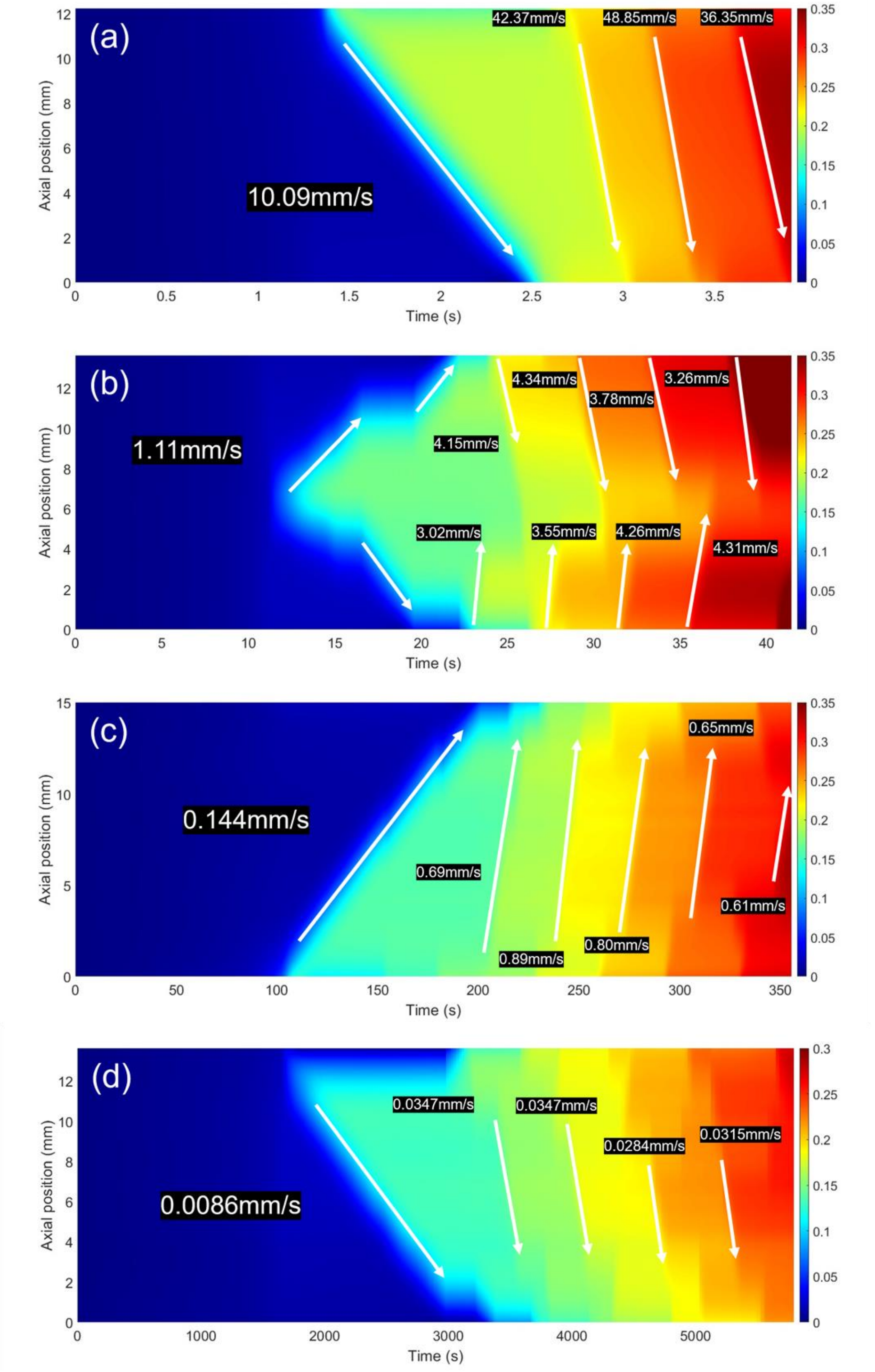

Figure 4.11 Strain evolution with time of 35-WR-LN extracted from DIC result at the strain rate of (a)$1\times10^{-1}s^{-1}$, (b)$1\times10^{-2}s^{-1}$, (c)$1\times10^{-3}s^{-1}$ and (d)$5\times10^{-5}s^{-1}$. With arrows indicating band propagation direction and labels showing the speed of propagating bands.

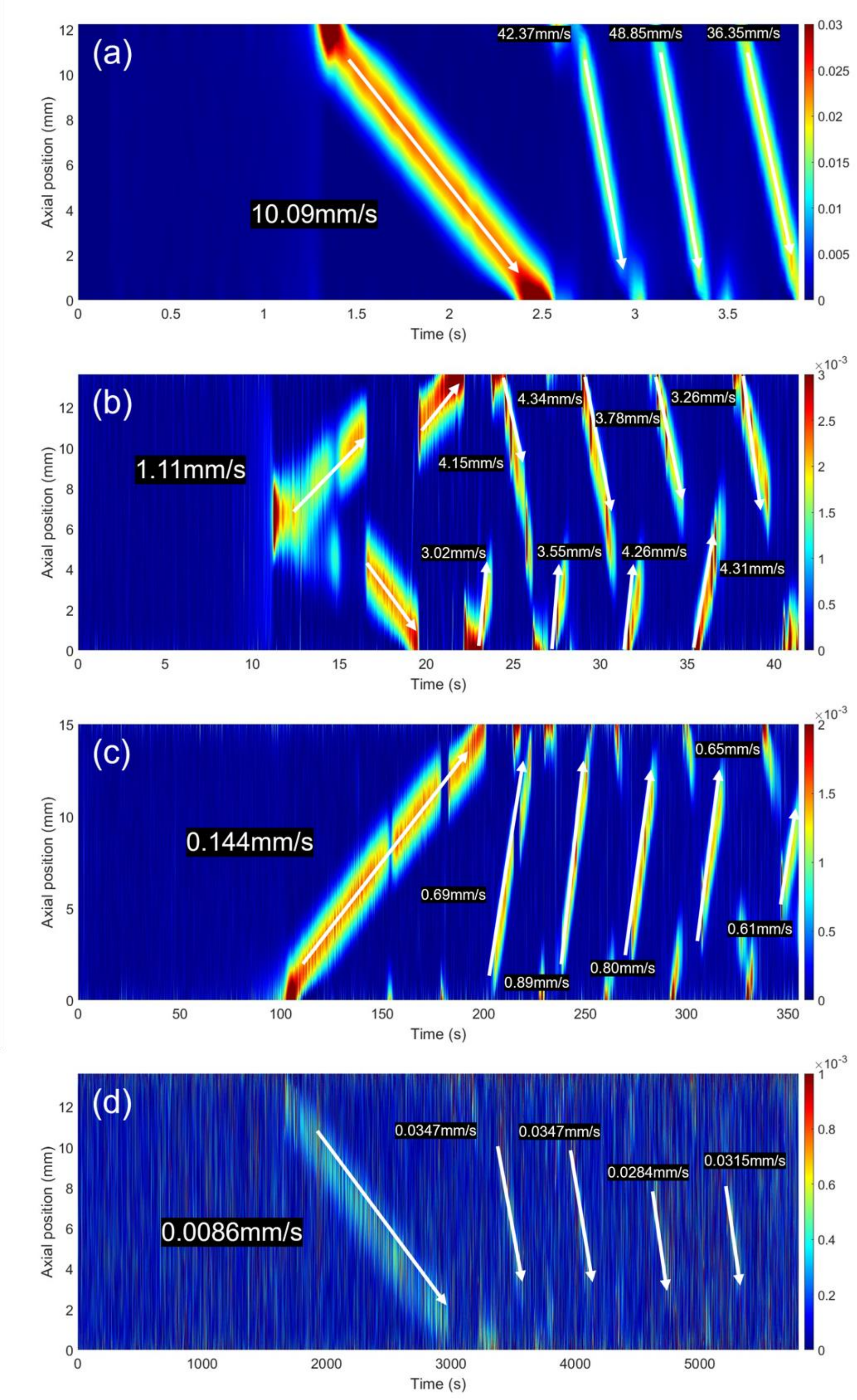

Figure 4.12 Differentiated strain evolution with time of 35-WR-LN extracted from DIC result at the strain rate of (a)$1\times10^{-1}s^{-1}$, (b)$1\times10^{-2}s^{-1}$, (c)$1\times10^{-3}s^{-1}$ and (d)$5\times10^{-5}s^{-}1$. With arrows indicating band propagation direction and labels showing the speed of propagating bands.

During the propagation of the Lüder band (Figure 4.12), it could be noticed that there are two noticeable zero-strain gaps at around 150 s and 175 s. Combing the DIC strain distribution map and stress-strain curve, it could be deduced that the hopping of the Lüder band from the top to the bottom of the specimen corresponds to a stress drop, followed by an increase in stress larger than the nominal stress than the rest of the Lüder band.

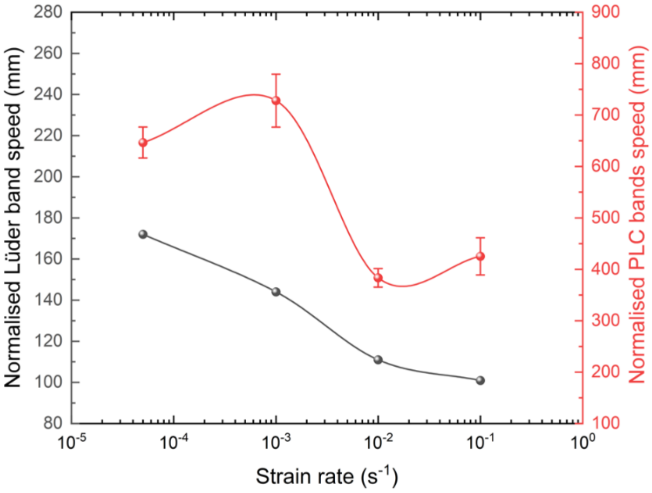

Figure 4.13 Normalised speed of Lüder band and PLC bands of 35-WR-LN varied with strain rates

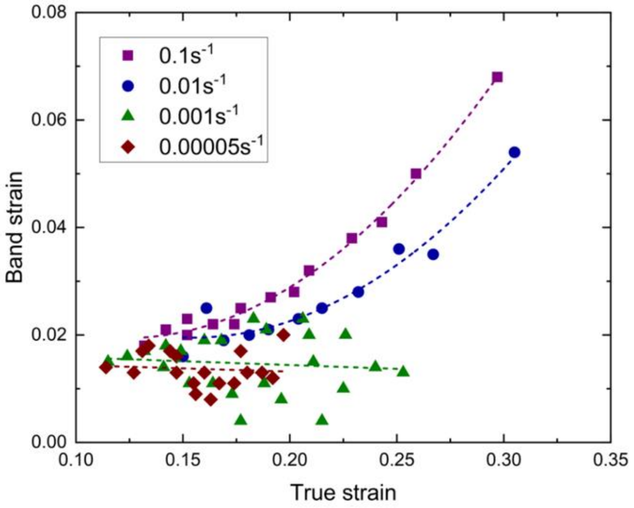

Figure 4.14 Band strain extracted from work-hardening curves. Band strain is defined as the true strain between two work-hardening rate peaks in Figure 4.2

4.4.2 Infrared thermographic imaging

Besides the strain mapping obtained by the DIC method, after post-processing temperature data in Matlab, the temperature evolution of the specimens during the tensile test was plotted with the x-axis representing the deformation time and the y-axis representing the position on the gauge length along the rolling direction of the specimen (Figure 4.15). During the deformation at a high strain rate, an enormous amount of heat was released to the sample surface. Under room temperature of approximately 24 °C, the temperature on the surface of the specimen reached a maximum of 91.2 °C for the tensile test at the strain rate of the 1×10^{-1} s^{-1}, 69.1 °C at the strain rate of 1×10^{-1} s^{-1} test, 34.5 °C at the strain rate of 1×10^{-3} s^{-1} test and 31.0 °C at the strain rate of 5×10^{-5} s^{-1} test.

In the temperature distribution maps, it could be observed that the temperature increased linearly along the tensile direction. The temperature variation is associated with strain localisation and/or localised phase transformation [40, 109], which is also known as the Lüder band and PLC band.

Figure 4.16 illustrates the differentiated temperature distribution contour graph with respect to each time increment, which shows the increase in temperature during band propagation in a more vivid manner. With decreasing the strain rate, the temperature changes became less significant and nearly disappeared when the strain rate is 5×10^{-5} s^{-1}. This could result from sluggish heat generation and quick heat dissipation because of the slow strain rate or the alternation of the PLC band feature. Another interesting observation is that the propagating speed of PLC tends to decrease slightly as the strain increase for the highest strain rate test, suggesting that it might be impeded at the later stage of deformation when the temperature of the material is elevated.

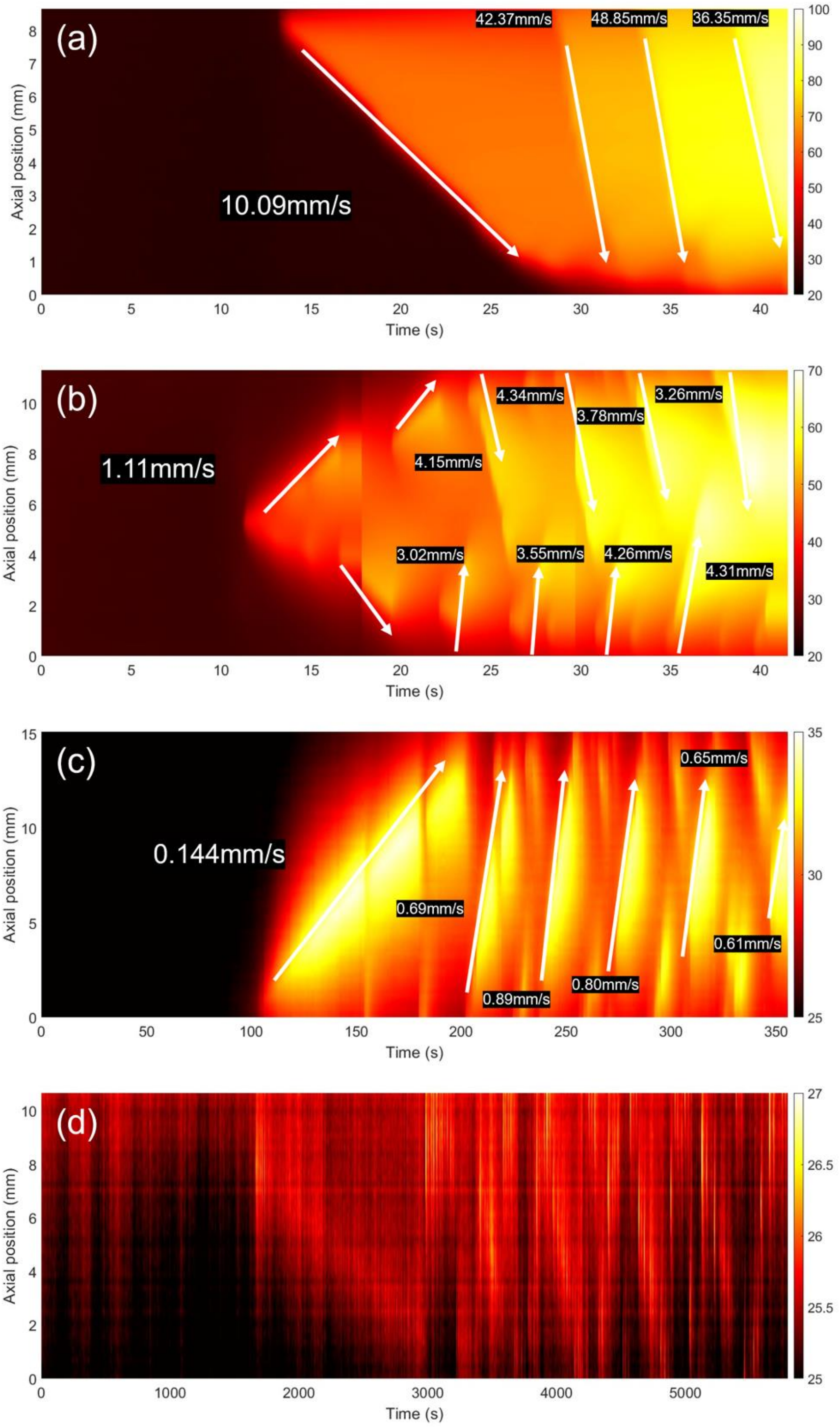

Figure 4.15 Surface temperature evolution with time of 35-WR-LN extracted from infrared camera result at the strain rate of (a)$1\times10^{-1}s^{-1}$, (b)$1\times10^{-2}s^{-1}$, (c)$1\times10^{-3}s^{-1}$ and (d)$5\times10^{-5}s^{-}1$. With arrows indicating band propagation direction and labels showing the speed of propagating bands.

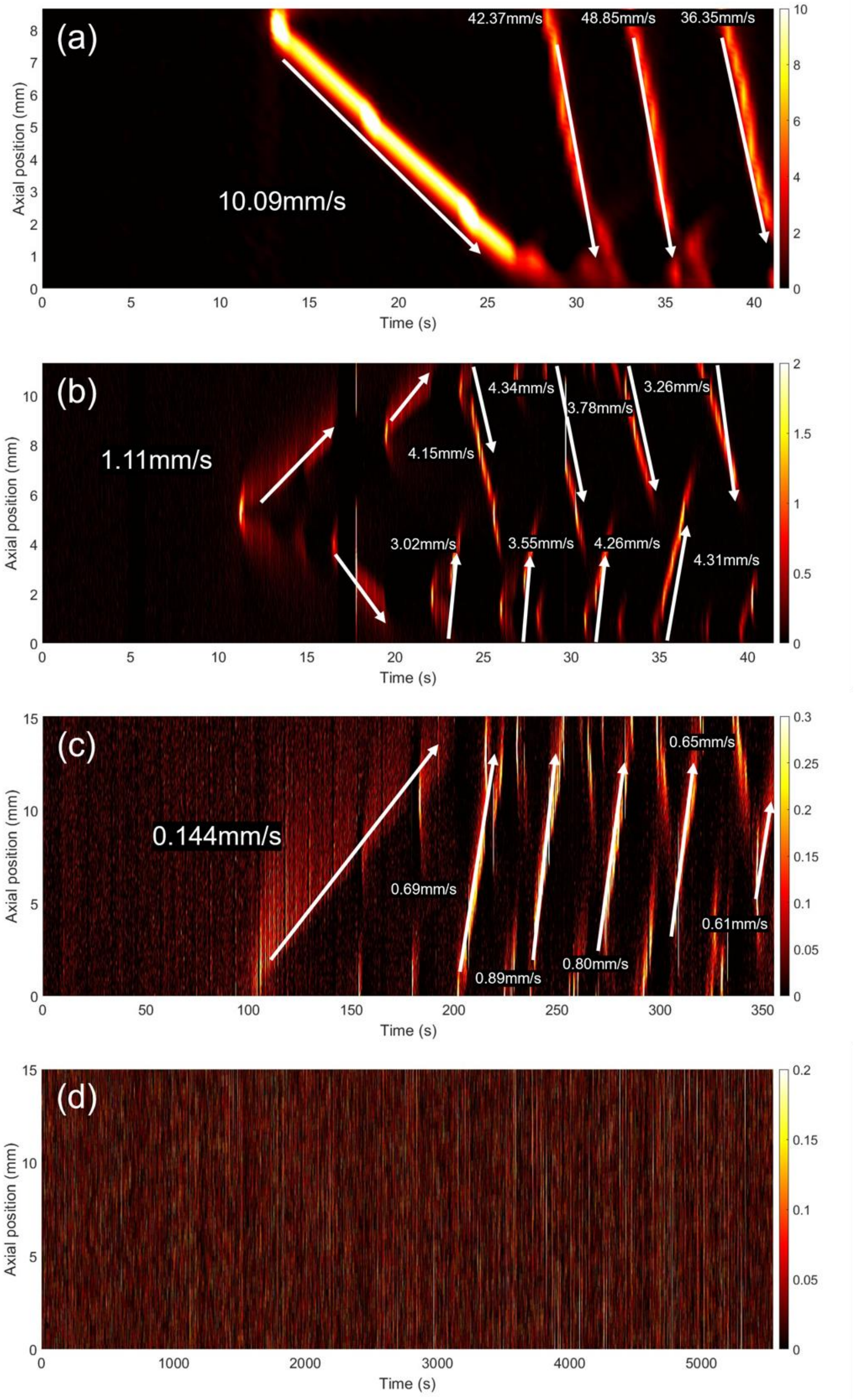

Figure 4.16 Differentiated surface temperature evolution with time of 35-WR-LN extracted from infrared camera result at the strain rate of (a)1×10^{-1}s^{-1}, (b)1×10^{-2}s^{-1}, (c)1×10^{-3}s^{-1} and (d)5×10^{-5}s^{-}1. With arrows indicating band propagation direction and labels showing the speed of propagating bands.

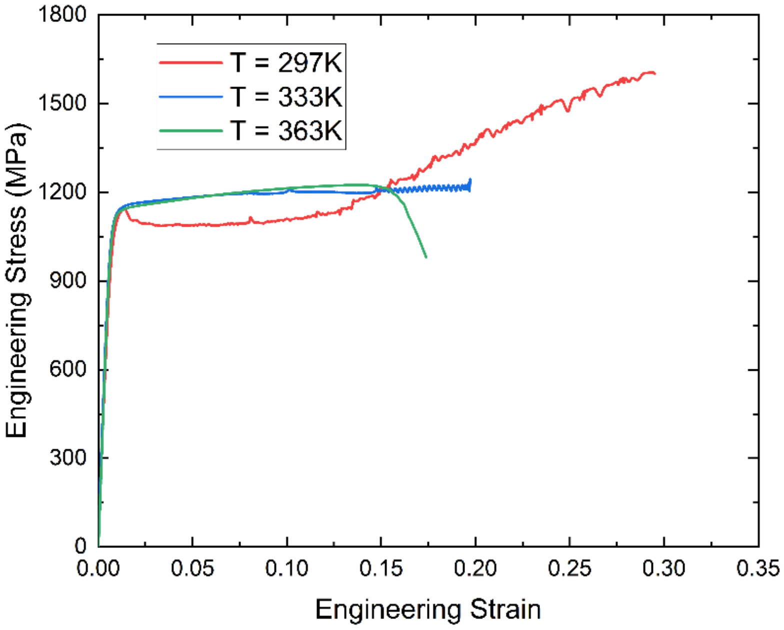

Figure 4.17 Tensile stress-strain curve of 35-WR-LN deformed at 1×10^{-3} s^{-1} with ambient temperatures of 297 K, 333K, 363 K

To further examine the temperature effect on the deformation mechanism, tensile tests at various temperatures and a strain rate of 1×10^{-3} s^{-1} were conducted and the stress-strain curves are shown in Figure 4.17. Temperatures were set at elevated temperatures that matched the highest surface temperature during the 1×10^{-1} s^{-1} strain rate test of 90 °C (363 K) and the medium temperature in-between 60 °C (333 K). The stress-strain curves obtained at elevated temperatures displayed a completely different work-hardening behaviour compared to that obtained at room temperature, noticeably the absence of yield drop at both temperatures. At 333K, the work-hardening rate was remarkably decreased, and the stress was kept almost constant except for the stress serration starting at the strain of 15%. Whereas at 363K, the obtained stress-strain curve was completely smooth without any sign of stress serration, and the work-hardening ability was significantly weakened compared to the room temperature test. A similar loss in work-hardening ability was reported at elevated temperatures (423K) on Fe–7Mn–0.12C–0.3Si medium Mn TRIP steel despite that the yield point elongation remained

[46]. The study by Yang et al. [38] also showed that stress serrations were absent when the deformation temperature increased to 373K.

It is well-establish that for austenite to transform to martensite, an energy barrier needs to be overcome, either by thermal activated or strain assisted. Increasing the temperature will require more chemical driving force, making the phase transformation more difficult to operate [34]. Another reason for an explanation using the SSA/DSA might be that due to the temperature elevation, the pinning and unpinning motion of dislocation is unable to operate, leading to the vanish of stress serration [64, 107].

The yield strength remains roughly constant at applied deformation temperatures, but the yield drop phenomenon was absent at elevated temperatures. Specimen deformed at 333 K experienced a tensile strength of 1244 MPa and total elongation of 19.7%. At 363 K, the tensile strength reached a similar level at the strain of 14.1%, followed by the necking, which was not observed in other deformation temperatures, resulting in a total elongation of 17.4%. Plastic instability was not observed at 363 K. The deformation is entirely continuous, whereas, at 333 K, periodic small stress serrations were observed after an engineering strain of 14.7%. The observations above suggest that the temperature indeed influences the deformation behaviour of the studied steel in a way that the temperature elevation induced by the phase transformation during high strain rate tests might contribute to the difference in the work-hardening rate.

To confirm the role of temperature in the phase transformation behaviour, we conducted EBSD phase mapping on the fractured sample tested at two temperatures, as shown in Figure 4.18, respectively. Phase transformation was almost absent in both tests due to the elevated temperature and, therefore, explained the reason why the global work-hardening rate of the highest strain rate test displayed the lowest value. Phase transformation was hindered by the elevated temperatures induced by the applied strain rate. However, we obtained the best combination of tensile strength and uniform elongation at the strain rate of $1\times10^{-2}\ s^{-1}$ despite the temperature elevation detected by the infrared camera (Figure 4.15). Therefore, we can conclude that the competition between the increase in strain rate and local temperature elevation has contributed to the difference in mechanical response. Cai et al. reported that the TRIP effect was responsible for the strain hardening at a low strain rate, while both TRIP and

TWIP effects were observed during medium and high strain rates, although the temperature variation was neglected in this study [45].

It could also be observed from the EBSD mapping that an excessive number of twins were formed during the deformation due to the elevated SFE, shifting the TRIP to TWIP effect. During the deformation at an intermediate strain rate of $1\times10^{-2}\,s^{-1}$, the first martensite formed at the shear band intersection, possibly in one of the twinned grains of the initial microstructure. The martensitic transformation caused the local temperature to increase, as reported by Wang et al. [40]. The increase in temperature can increase the local SEF, and heat dissipates to the neighbouring grains and elevates their temperature, which also increases the SFE. This could promote the formation of shear bands. Concurrently, due to the higher applied strain rate, the strain-induced martensite forms in the shear band intersection, leading to the pronounced TRIP effect. The transition from discontinuous to continuous Lüder and PLC bands might be caused by this mechanism as well. In other words, the deformation at a slow strain rate is driven by weak shear band formation sites such as microstructural defects, which constrain the mechanical properties of the test material, causing premature failure. Whereas for the fast strain rate test, the deformation is interfered with by the local alternation in SFE, leading to better ductility.

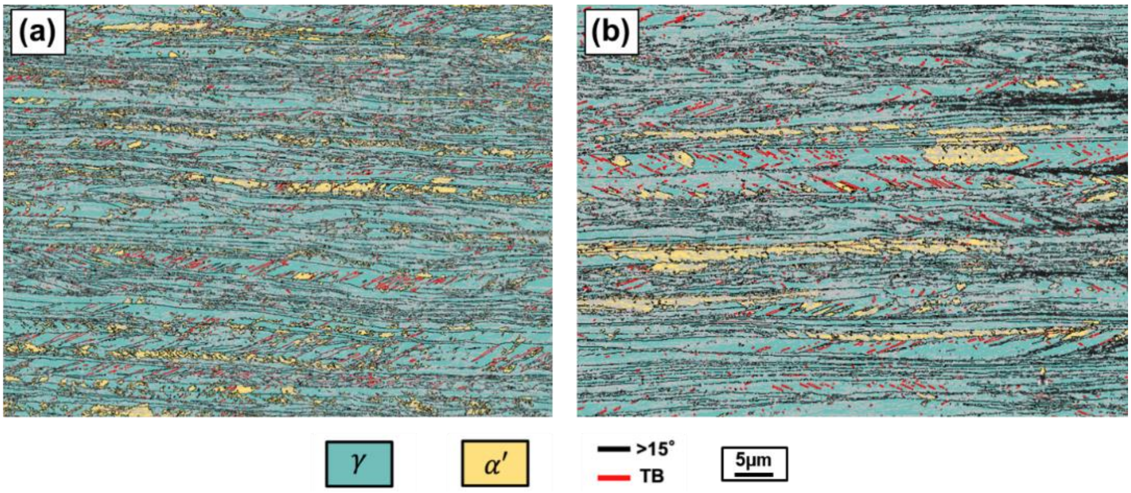

Figure 4.18 EBSD phase mapping of sample deformed at $1\times10^{-3}s^{-1}$ with an ambient temperature of (a) 333 K (87.4% Austenite and 12.6% Martensite) and (b) 363 K (89.3% Austenite and 10.7% Martensite)

4.5 Discussion

The cause of discontinuous yielding in metallic material remains unelucidated, although numerous theories have been used to explain this phenomenon in Fe-C metallic systems, including the plastic instabilities theory, static/dynamic strain aging theory, short/long range diffusion theory, dynamic precipitation theory [107]. Three main variables have been proposed to affect discontinuous yielding behaviour. Temperature and strain affect the diffusivity of solute atoms and dislocation, strain rate controls the waiting time of dislocation at the obstacles, and strain governs the overall dislocation density in the material. SFE of materials could also have a significant influence on discontinuous yielding since the stress serration could be attributed to a rapid formation of localised twins [107]. The amplitude of the stress drop is proportional to the SFE since higher stress is required to facilitate twinning [107]. Sun et al. [25] also reported discontinuous yielding behaviour is closely related to the amount of C-Mn complexes in medium Mn steels since they increase the SFE, which reduces the amount of partial dislocation and stacking faults.

The current steel sample underwent a rolling process at an intermediate temperature upon subsequent cooling to the cryogenic temperature (77 K), resulting in a microstructure with a high density of dislocations. The deformation during this step also created mechanical twins within the FCC austenite. The combining effects of dislocation plasticity in the martensite phase and the hardening effect due to the embedded twins greatly increase the nanohardness of the two constituted phases in the initial microstructure, minimising the possibility of strain partitioning at the initial stage of plastic deformation [57, 58]. Instead, the large number of C-Mn complexes resulting from the high weight percentage of Mn (12%) alloying element might be the reason for discontinuous yielding based on the short-range diffusion model theory in medium/high Mn steel [47, 107, 110, 111]. However, this might contradict the deformation mechanism that we observed previously, where martensitic transformation is preferentially initiated from austenite twins.

It is well-known that martensitic transformation is accommodated by the displacive movement of atoms, and the entire procedure is diffusionless, meaning that the DSA theory explained by the short-range diffusion model must be two separate events to the martensitic transformation. However, whether there exists a relationship in terms of energetic-assisted activation or localised strain-induced correlation remains unknown.

At the slow strain rates, since the dislocation velocity is low, the frequent pinning and unpinning events cause the serrated plastic flow, whereas at high strain rates, this event could be largely suppressed due to the higher dislocation velocity, with greater potential energy to sustain a relatively continuous flow until the successive PLC band passes through the whole gauge section. The time for the interaction of dislocations with other defects is limited, reducing the probability of stress concentration, which might lead to improved mechanical properties. On the contrary, a slow strain rate allows sufficient interaction between defects, which may induce more defects even after the propagation of the PLC band leading to premature failure. However, this does not explain why the normalised propagation speed of the Lüder band and PLC bands was higher at a slow strain rate.

Hopping of the PLC band, reported by Yang et al. [38], is related to the stability of the austenite phase stability as mentioned in Chapter 1.4. It results from the large fraction of martensitic transformation, which requires higher stress to overcome and suppress the propagation of the band and then results in localised transformation at another weak site. In our study, the hopping phenomenon was found in both Lüder and PLC banding regimes, at least at the strain rates of 1×10^{-2} s^{-1} and 1×10^{-3} s^{-1}. The stability of austenite should be identical among the entire specimen, and therefore, the hopping of the band is irrelevant to the extent of transformation. Since the variation in temperature for the sample deformed at 1×10^{-3} s^{-1} is insignificant, the effect of temperature elevation can be isolated. The work-hardening rate of the slow strain rate sample is noticeably higher than those deformed at a high strain rate. Hence the strain rate might be the factor affecting the feature of the PLC band.

The enhanced twinning effect might be a possible explanation for the increased work-hardening rate at a slow strain rate [107]. Deformation twinning occurs commonly to accommodate the plastic deformation in metal. The crystal lattice shears and forms an identical crystal structure with different orientations, with the symmetrical plane known as the twin plane. The deformation plasticity of steel with enriched manganese content (>15 w.t.% [110])

is often accommodated by twining due to the decreased SFE [25]. The current steel consists of 12 w.t.% Mn, sitting at a higher end of the medium Mn (3-12 w.t.%) regime, although the SFE was not simulated or approximated. The role of twinning is difficult to elucidate with the currently available data, but twin structures are indeed displayed in Figure 3.6. However, upon further straining, the number of twins did not show any sign of increasing, meaning that twinning could be irrelevant to the present deformation mechanism.

The microstructures of the initial warm-rolled and quenched steel possessed an elongated martensite matrix with embedded twin grains marked by red boundaries in Figure 3.6. As the deformation progressed (Figure 3.16), instead of nucleating more twins, as in the high Mn TWIP steel, the original twins got consumed and transformed into martensite. The shear band (twin bundles, ϵ platelets, and slip planes) intersection was known as the preferential nucleation site of strain/stress-induced α' martensite [34, 35]. Based on the parameters fitted from the OC model in Figure 4.6, α, representing the formation rate of the shear band, is the greatest for the slowest strain rate among all tests. This is believed to correspond to the highest work-hardening rate and strength at the same level of strain. Noticeably more frequent stress serration events could be observed in the work-hardening curve on the slowest strain rate curve. This is probably due to the prolonged wait time for partial dislocation motion and sufficient time for shear band formation and phase transformation.

For the deformation at higher strain rates, however, the more rapid rate of deformation leaves no time for the complete process for the shear bands to interact. The phase transformation turned into the quasi-Lüder band type, as illustrated on the stress-strain curve (Figure 4.1). Minor shear band nucleation and martensitic transformation scattered around the specimen, making the strain distribution hard to detect using the DIC method. The phase transformation at higher strain rates was rather localised and continuous. When the stress reaches a certain level, the new PLC band nucleates and propagates. This might explain the fundamentally different PLC banding behaviour on the deformation curve. Randomly nucleated shear bands and the subsequent phase transformation might also make the steel more vulnerable since the strain is more likely to concentrate on intrinsic defects, which might also explain the high susceptibility to hydrogen embrittlement reported earlier.

Intermittent plastic flow, which is analogous to serration, is another term used to describe small-scale plastic instability. Intermitted-to-smooth transition in microplasticity in metallic systems (Nb, Au, and Cu alloy systems) was reported frequently in small-scale crystals, usually on the scale of micrometre [112-114]. The magnitude and frequency of intermittent were reported to significantly associate with the displacement rate and sample size [112]. The absence of plastic intermittency was found when the strain rate exceeds 2.5 s^{-1}, attributing to the delocalisation of slip with increasing rates. A higher strain rate requires the operation of multiple sources of dislocation to sustain the plastic strain rate, in which a large number of dislocation sources merge and form a smooth plastic flow. This would require massive dislocation multiplication at the early stage of the deformation [112].

4.6 Summary

To summarise, we have investigated the effect of strain rate on the plastic instability behaviour in the present medium Mn steel. It was found that the strain rate has a substantial impact on the discontinuous yielding phenomenon, primarily by affecting the formation mechanisms of the shear bands. The elevation of temperature was induced by the rapid rate of straining, causing a secondary effect on the kinetics of phase transformation as well. Therefore, the mechanical properties also varied under different strain rates. We have characterised the discontinuous yielding macroscopically through various techniques, and future study should focus on discovering more microstructural evidence.

Chapter 5 Hydrogen embrittlement

5.1 Overview

Hydrogen energy has shown its promising potential as an alternative to fossil fuel due to its completely green burning by-product. However, materials, particularly high-strength alloys, are susceptible to hydrogen embrittlement in many service environments for renewable energy applications such as hydrogen transportation and the bearings of wind turbines. Hydrogen-induced embrittlement can lead to unpredictable and catastrophic failures at relatively low applied stresses. The associated hydrogen embrittlement issue has not been fully understood in metallic material systems. The current medium Mn steel consists of two distinct phases with different responses to hydrogen intake. Hydrogen susceptibility has been reported to be associated with the deformation mechanisms of medium Mn steels since the metastable austenite undergoes martensitic transformation under external load, and the diffusible hydrogen will release from austenite and segregate to phase boundaries, causing hydrogen-enhanced decohesion and therefore promoting the premature failure. Numerous factors have been reported to have crucial influences on the hydrogen diffusion paths and crack propagation paths, such as the solid solution precipitation [115], the local austenite stability [75], and grain morphology [68]. In addition, it is commonly known that hydrogen susceptibility is proportional to the strength of the material, and therefore, the toleration of advanced high-strength steel to hydrogen ingression is much lower than its lower-strength counterparts.

5.2 Experimental methodology

As reported in Chapter 3, the current medium Mn steel possesses elongated grain morphology and vanadium carbides were found in the austenite phase. Both of these features were reported to have resistance to hydrogen embrittlement [66]. Regarding this, we have conducted numerous hydrogen-related mechanical testing on the currently studied medium Mn steel.

Hydrogen charging of the sample was performed using the AMETEK VersaSTAT 4 Galvanostat by two-electrode setup, where the Platinum foil served as the working electrode and the tensile sample was placed as the counter electrode with the reference electrode attached for measuring the potential across the cell. The experimental setup for hydrogen charging is illustrated in Figure 5.1.

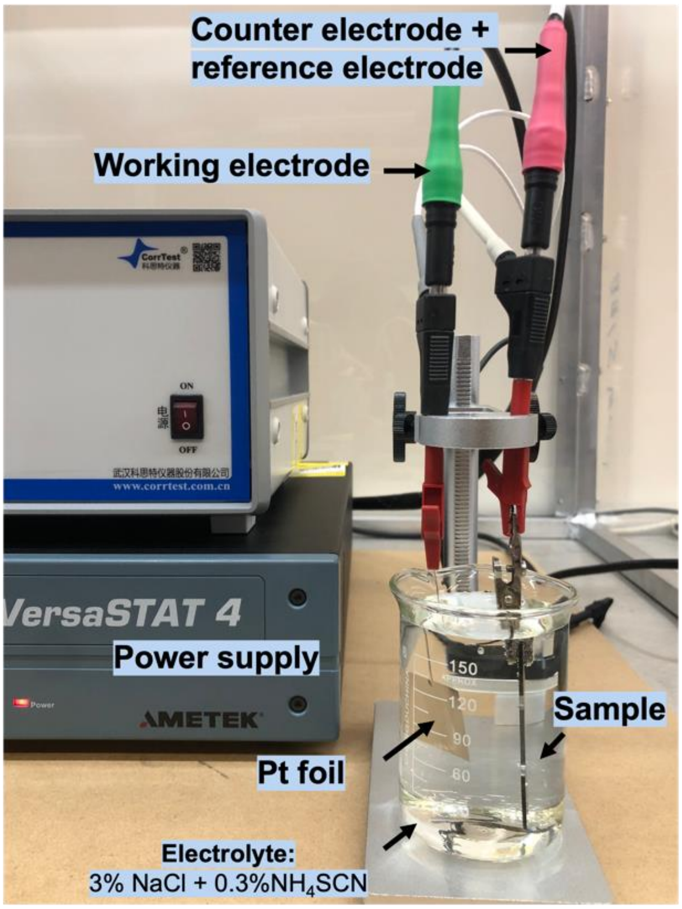

Figure 5.1 Experimental setup for hydrogen charging of the tensile specimen

The current density was set at 5 A/m^2, and a charging time of 24 hours was used [69]. The charging electrolyte implemented in the experiment was 3 wt.% Sodium Chloride (NaCl) with 0.3 wt.% Ammonium Thiocyanate (NH_4SCN). Sodium Chloride serves as an electric charge carrier, and Ammonium Thiocyanate serves as a hydrogen recombination poison that prevents hydrogen atoms from forming hydrogen gas which releases into the air [116-120]. The hydrogen-charged tensile sample was transferred and loaded to the universal tensile testing machine within 15 minutes to minimise the loss of hydrogen to the environment. The strain rate for the tensile testing was set at 0.05 mm/min (5×10^{-5}s^{-1}) to allow sufficient time for hydrogen atoms to interact with microstructural features [69, 75].

5.3 Results

The typical engineering stress-strain curves of the hydrogen-free and hydrogen-charged samples are plotted in Figure 3.16. The yield strength was not apparently affected by the hydrogen ingression, as well as the elastic modulus. Whereas at the point of fracture, the tensile strength, measured as 1210 MPa, decreased by 18%; the uniform elongation dropped to 13.2%, suffering a total elongation loss (HEI) of 37%. The benchmark of hydrogen resistance with medium Mn steels designed by other researchers (Figure 5.3a) [68, 70, 72, 77, 78, 121-123] indicates that the hydrogen resistance from the current studied steel with moderate HEI is acceptable. In fact, the present steel demonstrated the highest tensile strength compared to the counterparts with similar HEI (Figure 5.3b).

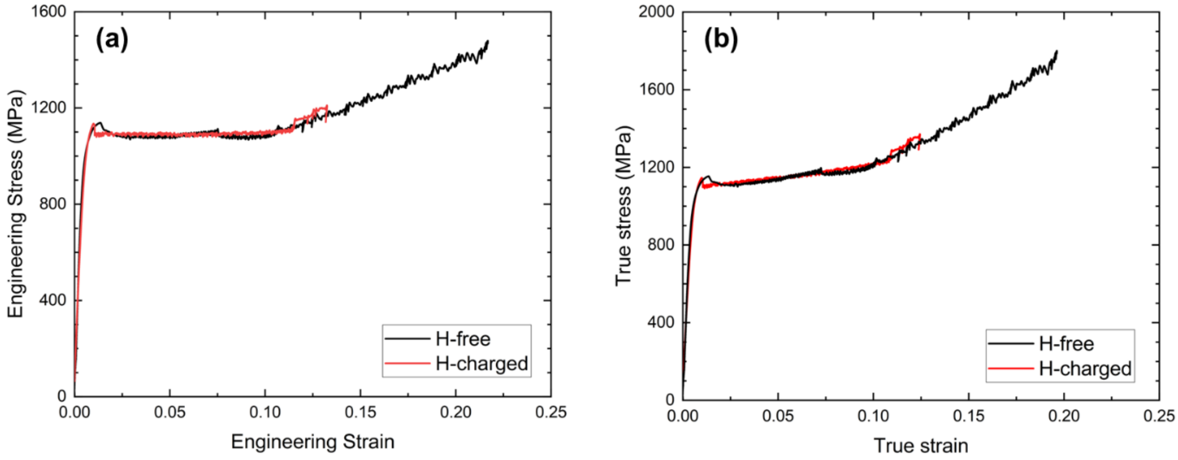

Figure 5.2 (a) Engineering stress-strain curve and (b) true stress-strain curve of the hydrogen-free and hydrogen-charged sample under a strain rate of 5×10^{-5}s^{-1}

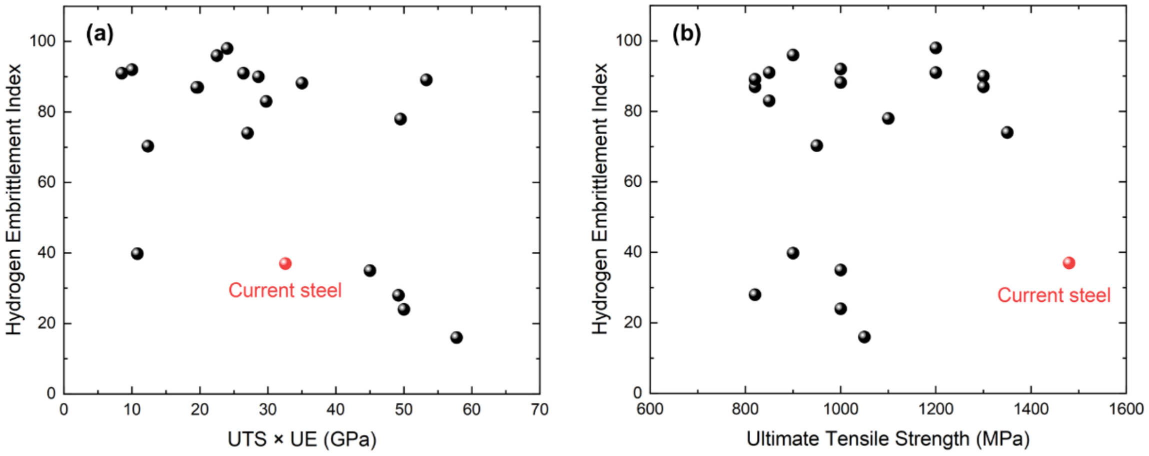

Figure 5.3 Benchmark of hydrogen resistance with other medium Mn steels [68, 70, 72, 77, 78, 121-123]. (a) Product of UTS and UE, and (b) UTS verses hydrogen embrittlement index

The mechanical performance was deteriorated by the entry of hydrogen, and the discontinuous yielding was preserved. Figure 5.2b shows that the work-hardening rate was not affected by the hydrogen either, indicating that the deformation mechanism was not altered, which can be further proved by EBSD phase mapping (Figure 5.4) and in-situ magnetic measurement (Figure 5.5). It is clear that the transformed austenite fraction increased in the same trend, with no difference in phase transformation kinetics. Therefore, it is safe to conclude that the fracture mechanism might be changed by hydrogen ingression, and the fractography will be a good indication.

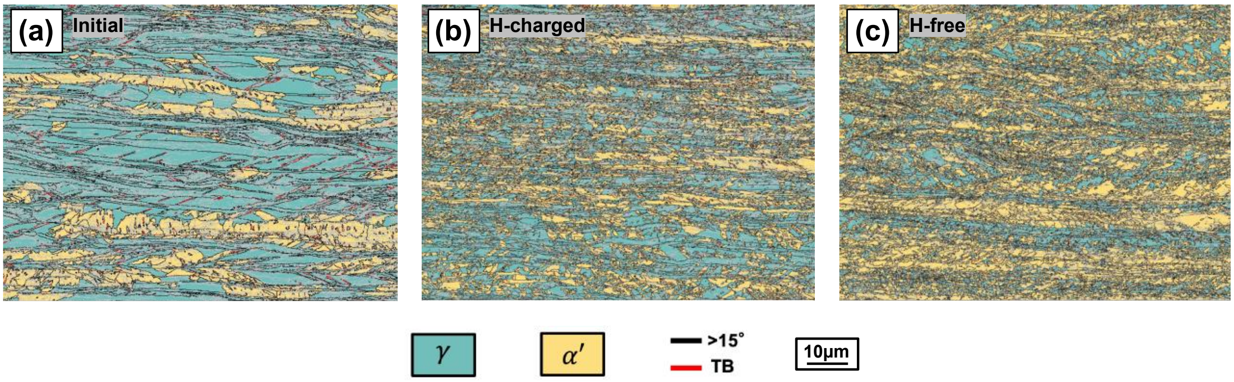

Figure 5.4 EBSD phase map of (a) original sample before the tensile test, (b) deformed hydrogen-charged sample and (c) hydrogen-free sample after fractured

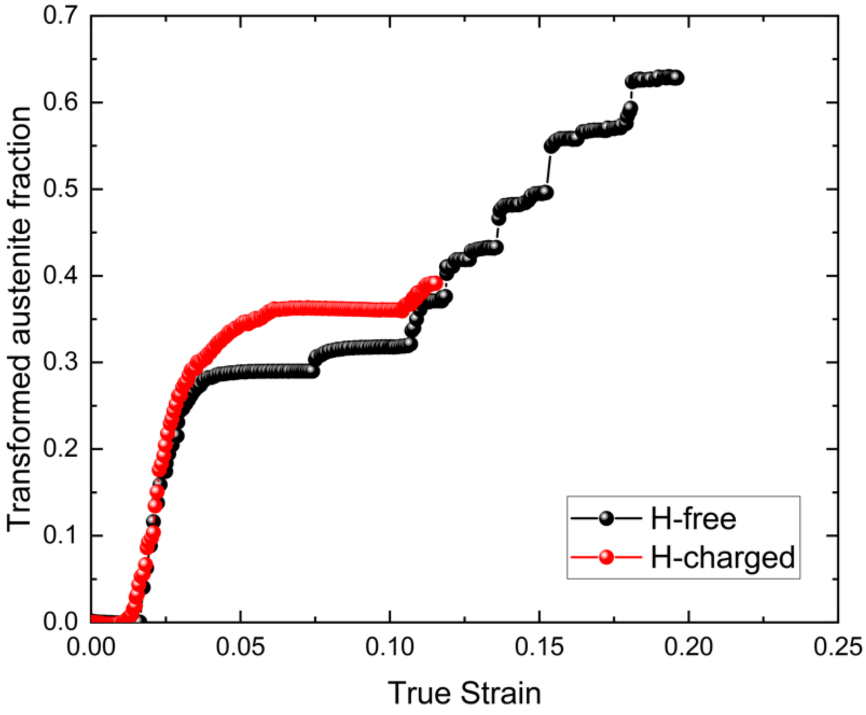

Figure 5.5 In-situ magnetic measurement using Feritscope during the tensile test of hydrogen-free and hydrogen-charged sample under strain rate of $5\times10^{-5}s^{-1}$

Previous investigations indicated that the intake of hydrogen could cause changes in the local nanohardness of metallic material [66, 84, 124]. The pop-in behaviour on the force verse displacement curve was commonly associated with phase transformation [57, 58]. To elucidate the hydrogen effect on the local mechanical properties, nanohardness tests were also conducted on the hydrogen-charged sample using the UMIS nanoindentation platform. Hydrogen charging was performed using the experimental setup as illustrated in Figure 5.1 with a current density of 5 A/m^2 and a charging time of 24 hours. Nanoindentation tests were conducted within 15 minutes after charging. The results of the hardness were obtained from the load-displacement curve and plotted in Figure 5.6. Due to the prolonged charging time, the sample surface condition could not be indexed by EBSD detection in SEM. Hence, the results represent the hardness of the combination of the two phases.

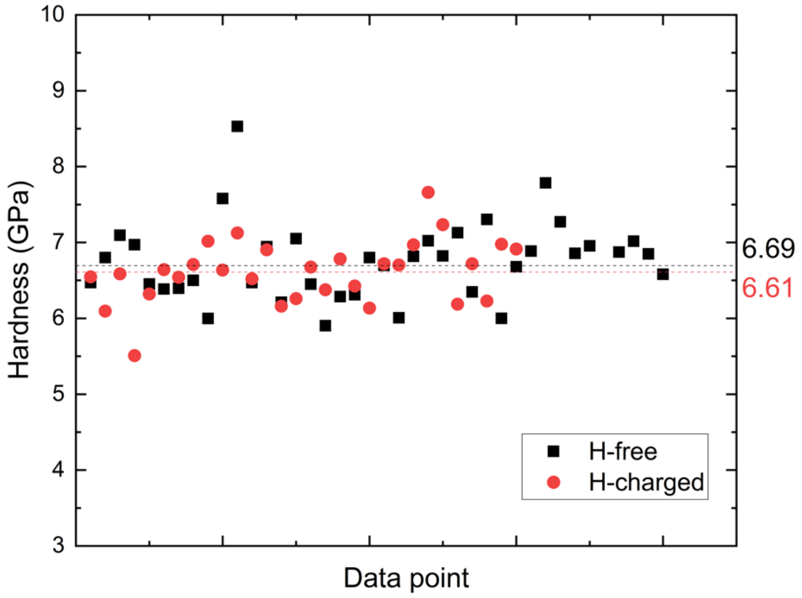

Figure 5.6 Nanohardness of hydrogen-free and hydrogen-charged samples measured by nanoindentation

The nanoindentation test showed that the hardness of the material is roughly independent of the hydrogen status, and the pop-in behaviour was not observed among all force-displacement curves, further proving that the phase transformation mechanism was not apparently affected by the intake of hydrogen. This independence of the hardness on the hydrogen in the present steel is distinct from previous investigations, which suggested that the intake of hydrogen in austenitic stainless steel would increase the nanohardness due to the activation of secondary slip planarity [124, 125]. This might be attributed to the initially high density of dislocation inherited from insufficient recrystallization during heat treatment and processing.

5.4 Discussion

In Chapter 3.3, the nanohardness of austenite and martensite phases was measured, and the hardness difference between the two phases could be negligible. Therefore, the potential effect of strain partitioning can be excluded as a reason for the premature failure of the hydrogen-charged sample. It is well reported that hydrogen embrittlement of metallic material is driven by two mechanisms, i.e., the HELP and HEDE. The HELP mechanism suggests that the increase in local plasticity will significantly promote the formation of voids, and the accumulation of voids will lead to the formation of cracks [69]. This type of fracture mechanism can be reflected in the fractography by a large amount of void [126]. The HEDE mechanism indicates that the hydrogen prefers to segregate at the grain boundaries, reducing the bonding energy and then leading to crack formation [69]. The topography of the fracture surface results from the HEDE mechanism featured with quasi-cleavage facets [76].

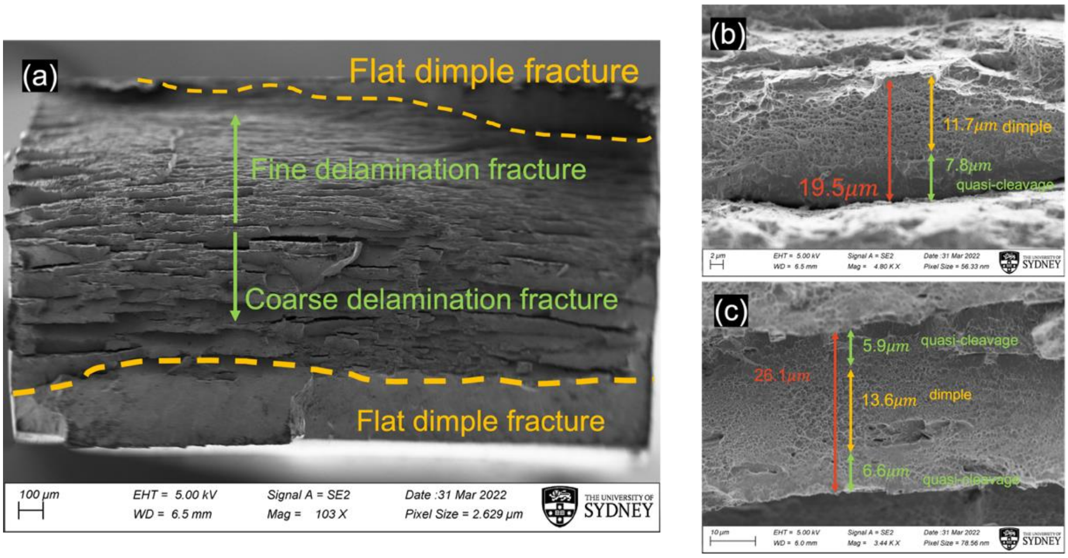

Figure 5.7 Fractography of hydrogen-free sample strained at $5\times10^{-5}s^{-1}$ with (a) the overview and (b, c) the magnification on layer

To elucidate the effect of hydrogen ingression on the fracture mechanism, the fractography of H-free and H-charged samples were studied using SEM. The uncharged sample features two types of fracture topography, namely, the delamination fracture and the dimple fracture, as shown in Figure 5.7. On the layer of delamination fracture, two types of fracture could be observed, namely the dimple fracture and the quasi-cleavage fracture. The dimple fracture could further be divided into two types, namely equiaxial dimples and parabolic dimples [127]. The equiaxial dimple results from uniform stress and the parabolic dimples are caused by lateral load [127]. The thickness of delaminated layers has a similar thickness (tens of microns) compared to the sample deformed at the strain rate of 1×10^{-3} s^{-1}.

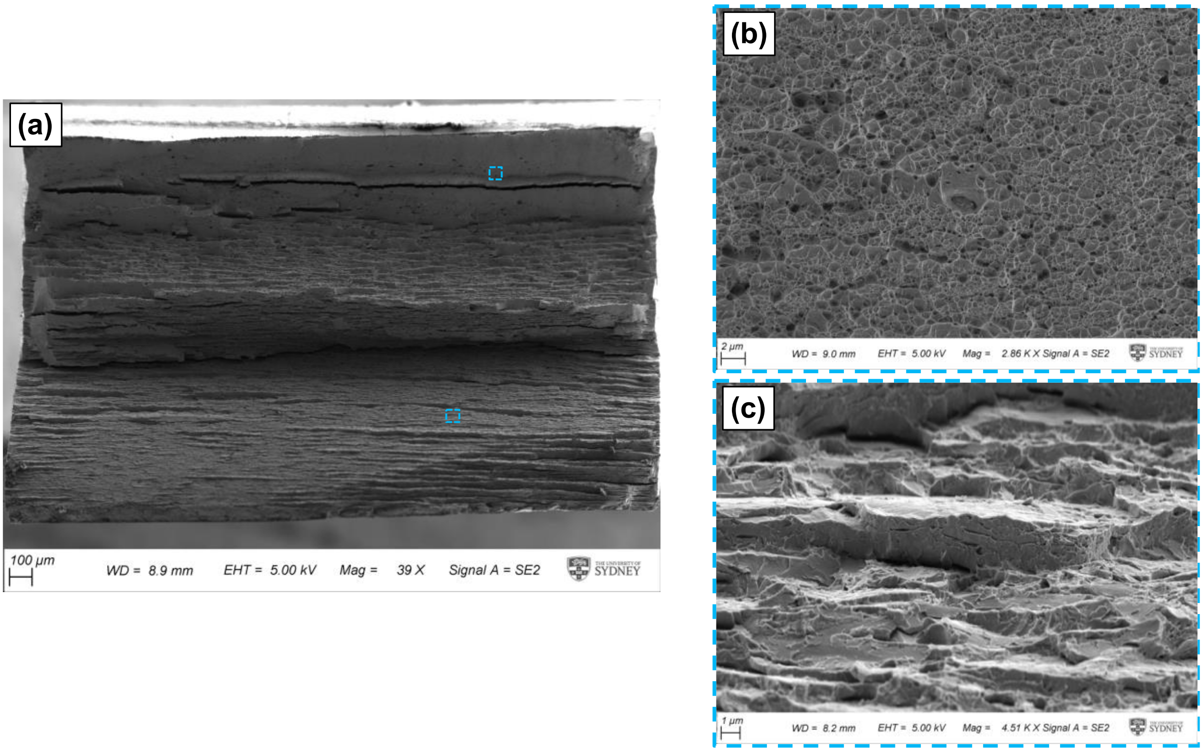

Figure 5.8 Fractography of hydrogen-charged sample strained at $5\times10^{-5}s^{-1}$ with (a) the overview and (b, c) the magnification on layer

The fracture surface of the hydrogen-charged sample is exhibited in Figure 5.8. It is displayed that flat dimple fracture is also presented in the H-charged sample (Figure 5.8b). The difference in fractography between H-free and H-charged samples is distinguishable in the delaminated fracture region (Figure 5.8c), in which the thickness of delaminated layers is smaller after the ingression of hydrogen with a thickness of several microns. In each delaminated layer, the dimple-type surface is absent, whereas the quasi-cleavage surface remains. Hence, it can suggest the existence of hydrogen embrittlement in the current material. The fracture mechanism is altered by the ingression of hydrogen, and the embrittlement mechanism may be dominated by the well-established HEDE mechanism.

5.5 Summary

We applied electrochemical charging on the present medium Mn steel in order to facilitate hydrogen ingression, aiming to test the resistance to hydrogen embrittlement and reveal the underlying mechanism. Results show that the current steel suffered from hydrogen embrittlement with 37% total elongation loss. We did not find any sign of the hardness increase in both phases, and the phase transformation kinetics are believed to be unaffected by the intake of hydrogen. Therefore, we concluded that the originally ductile steel was embrittled by hydrogen through the HEDE mechanism, due to the diffusible hydrogen released from the austenite during phase transformation. Future studies on hydrogen embrittlement should be focused on introducing the microstructure features through heat treatments which could prevent hydrogen-induced crack propagation.

Chapter 6 Conclusion and future work

6.1 Conclusion

In conclusion, the current work has been focused on the microstructures, mechanical properties, deformation mechanisms, and hydrogen embrittlement behaviour of a medium Mn steel with the chemical composition of Fe-12Mn-0.35C-2Al-0.4V-0.8Mo. This advanced steel shows a superior combination of yield strength, tensile strength, and uniform elongation compared to other medium Mn counterparts that have been investigated. The remarkable yield strength can be mainly attributed to 1) the martensite with high dislocation density resulting from the quenching process, 2) the high density of dislocation and twins in retained austenite, and 3) precipitate strengthening from the Vanadium carbide. Whereas the superior tensile strength and uniform elongation mainly stemmed from the gradual transformation of retained austenite which can induce the dynamic “Hall-Petch” relationship to strengthen the materials and allow a sustainable work-hardening stage to promote significant plasticity and enable excellent ductility.

In addition, we have found the pronounced discontinuous yielding phenomena in the current steel, featured by the Lüder band after yielding and the PLC bands during the work-hardening stage. These instable plastic phenomena are found to be highly associated with martensitic transformation, which is also significantly affected by the applied strain rates and temperatures. To investigate the underlying mechanisms, we conducted numerous universal tensile experiments with variations in strain rates and ambient temperatures. To characterise this discontinuous yielding behaviour, we have implemented Feritcope, DIC camera, and infrared camera to the experiments, along with a series of microstructural characterisations using SEM and EBSD.

Results showed that the discontinuous yielding mode changed by increasing the strain rates from $5\times10^{-5}s^{-1}$ to $1\times10^{-1}s^{-1}$, in which stress serration was barely found at a high strain rate.

Tensile strength and uniform elongation experienced a first increase and then decreased trend. The ultimate tensile strength and uniform elongation peaked at a strain rate of 1×10^{-2} s^{-1} due to a more pronounced phase transformation in this sample. We have attributed this improvement of mechanical properties to the combined effect of local temperature rise and shear band formation.

The resistance of the current steel to hydrogen embrittlement was also examined using various testing methods. It was found that the steel experienced premature failure during a slow strain rate tensile test after electrochemical charging of 24 h, featured with a 37% total elongation loss and 18% tensile strength loss compared with the uncharged sample. The hardness of both phases in the material remained nearly unchanged before and after the hydrogen charging measured by the nanoindentation test, indicating that there is no obvious strain partitioning effect involved. By comparing the fractography of the H-free and H-charged sample, it could be proposed that the material is likely embrittled by the HEDE mechanism, reflected by the decrease in delaminated layer thickness and the absence of dimple-type fracture surface within the layer.

6.2 Future work

Current work has demonstrated that the mode of discontinuous yielding behaviour has changed remarkably with increasing the applied strain rates. However, the Lüder band and PLC bands were yet to disappear even at the highest strain rate of 1×10^{-1} s^{-1}. Since the constant crosshead speed had already reached the maximum value during these tests, it is worth performing additional tests under a higher strain rate, such as the split Hopkinson tensile bar experiment [128] to examine if the discontinuous yielding behaviour could be suppressed by further increasing the strain rates.

Current studies have performed extensive characterisations on localised deformation. However, most attention was focused on the macroscopic behaviour rather than on the microscale. Although the explanation concerning phase transformation has mentioned the formation mechanism of the shear band, there is not sufficient microscopic evidence to support it. Therefore, future work could concentrate on the microscale characterisation of the Lüder band and PLC bands. For example, recent studies have implemented high-resolution in-situ DIC to observe the strain partitioning effect on dual-phase material under SEM and EBSD, providing real-time observation of the phase interaction during deformation (Figure 6.1)[43, 60, 129]. In addition, in-situ observations of transformation and the associated discontinuous yielding behaviours have barely been studied under TEM, leaving a large knowledge gap and hindering the understanding of the deformation mechanism of this steel at the nanoscale. One of the barriers preventing the in-situ TEM study is the difficulty of preparing the TEM sample. The focused ion beam is an essential tool for TEM sample fabrication due to its superior resolution and easy operation [130]. However, our studies have found that the current steel is vulnerable to high-energy FIB milling and would inevitably induce phase transformation during this process. Therefore, future studies could consider the possibility to apply the cryogenic FIB that might potentially suppress the phase transformation.

In addition, although the tensile performance significantly deteriorated when the deformation temperature is elevated, the discontinuous yielding behaviour tends to disappear, and no work-hardening is observed. Phase transformation is suppressed due to the elevated SFE, and deformation tends to be carried by deformation twinning. In another way, future studies may focus on deformation behaviours at cryogenic temperatures, in which ϵ martensite is more likely to form. This investigation could provide more insight into the relationship between phase transformation and plastic instability.

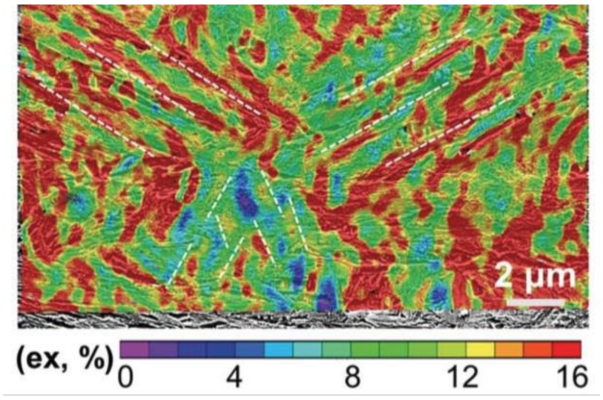

Figure 6.1 High-resolution DIC study conducted by in-situ SEM [129]

The present material is vulnerable to hydrogen ingression, making it inapplicable to hydrogen-related applications. More attention could be dedicated to investigating potential solutions to reduce the effect of hydrogen embrittlement, for example, applying heat treatments to tailor the microstructure feature and alter the hydrogen-induced crack propagation mechanism [75]. Also, in the present study, the nanohardness tests were conducted in an *ex-situ* manner. Although the sample was transferred to the testing equipment within 15 minutes, the hydrogen would inevitably diffuse to the air during the transferring and testing processes. Therefore, *in-situ* nanohardness test is recommended to perform to eliminate this systematic uncertainty. In fact, the *in-situ* testing equipment has been designed and modelled using Solidworks and manufactured through polymer additive manufacturing, as illustrated in Figure 6.2. By doing this, test results with higher reliability can be generated, and provide more valuable information for improving the hydrogen resistance of the present steel.

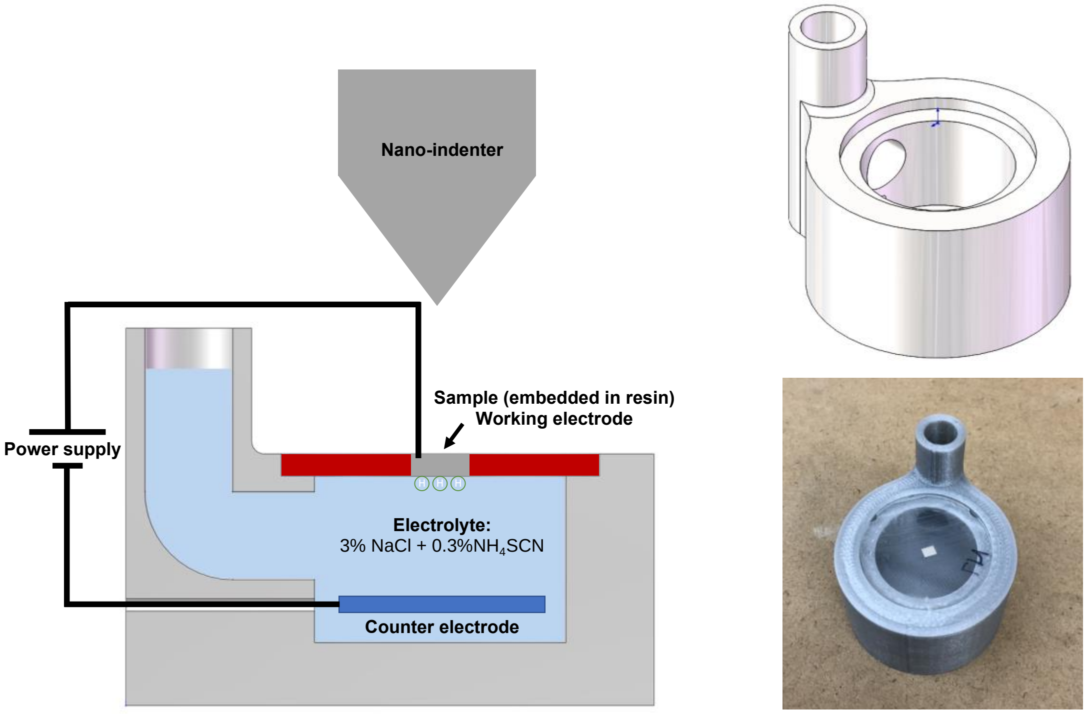

Figure 6.2 *In-situ* nanoindentation equipment concept and prototype for hydrogen charging

Chapter 7 References

[1] H. Bhadeshia, R. Honeycombe, Steels: microstructure and properties, Butterworth-Heinemann2017.

[2] H. Pollack, Fe-Fe3C Phase Diagram, Materials Science and Metallurgy. 4th ed. Hoboken, New Jersey, United States: Prentice-Hall (1998).

[3] L.S. Marks, Marks' standard handbook for mechanical engineers, Standard handbook for mechanical engineers (1978).

[4] R.E. Reed-Hill, R. Abbaschian, R. Abbaschian, Physical metallurgy principles, Van Nostrand New York1973.

[5] B. Sun, F. Fazeli, C. Scott, N. Brodusch, R. Gauvin, S. Yue, The influence of silicon additions on the deformation behavior of austenite-ferrite duplex medium manganese steels, Acta Materialia 148 (2018) 249-262.

[6] N. Sekiguchi, The evolution of non-OECD countries in the twenty-first century: developments in steel trade and the role of technology, Mineral Economics 35(1) (2021) 103-132.

[7] M. Shome, M. Tumuluru, Introduction to welding and joining of advanced high-strength steels (AHSS), Welding and Joining of Advanced High Strength Steels (AHSS), Elsevier2015, pp. 1-8.

[8] B. Hu, H. Luo, F. Yang, H. Dong, Recent progress in medium-Mn steels made with new designing strategies, a review, Journal of Materials Science & Technology 33(12) (2017) 1457-1464.

[9] J. Zhao, Z. Jiang, Thermomechanical processing of advanced high strength steels, Progress in Materials Science 94 (2018) 174-242.

[10] H. Aydin, E. Essadiqi, I.-H. Jung, S. Yue, Development of 3rd generation AHSS with medium Mn content alloying compositions, Materials Science and Engineering: A 564 (2013) 501-508.

[11] R.L. Miller, Ultrafine-grained microstructures and mechanical properties of alloy steels, Metallurgical and Materials Transactions B 3(4) (1972) 905-912.

[12] B. Sun, A. Kwiatkowski da Silva, Y. Wu, Y. Ma, H. Chen, C. Scott, D. Ponge, D. Raabe, Physical metallurgy of medium-Mn advanced high-strength steels, International Materials Reviews (2023) 1-39.

[13] Z. Dai, H. Chen, R. Ding, Q. Lu, C. Zhang, Z. Yang, S. van der Zwaag, Fundamentals and application of solid-state phase transformations for advanced high strength steels containing metastable retained austenite, Materials Science and Engineering: R: Reports 143 (2021).

[14] B. He, B. Hu, H. Yen, G. Cheng, Z. Wang, H. Luo, M. Huang, High dislocation density–induced large ductility in deformed and partitioned steels, Science 357(6355) (2017) 1029-1032.

[15] T. Pepelnjak, E. Kayhan, B. Kaftanoglu, Analysis of non-isothermal warm deep drawing of dual-phase DP600 steel, International Journal of Material Forming 12 (2019) 223-240.

[16] D.-W. Suh, S.-J. Park, T.-H. Lee, C.-S. Oh, S.-J. Kim, Influence of Al on the Microstructural Evolution and Mechanical Behavior of Low-Carbon, Manganese Transformation-Induced-Plasticity Steel, Metallurgical and Materials Transactions A 41(2) (2009) 397-408.

[17] B. Hu, B. He, G. Cheng, H. Yen, M. Huang, H. Luo, Super-high-strength and formable medium Mn steel manufactured by warm rolling process, Acta Materialia 174 (2019) 131-141.

[18] Y. Han, J. Shi, L. Xu, W. Cao, H. Dong, Effects of Ti addition and reheating quenching on grain refinement and mechanical properties in low carbon medium manganese martensitic steel, Materials & Design 34 (2012) 427-434.

[19] B. Hu, F. Ding, X. Tu, Q. Guo, C. Ding, Y. Wang, H. Luo, Influence of lamellar and equiaxed microstructural morphologies on yielding behaviour of a medium Mn steel, Materialia 20 (2021).

[20] J. Sun, T. Jiang, Y. Sun, Y. Wang, Y. Liu, A lamellar structured ultrafine grain ferrite-martensite dual-phase steel and its resistance to hydrogen embrittlement, Journal of Alloys and Compounds 698 (2017) 390-399.

[21] P. Wen, B. Hu, J. Han, H. Luo, A strong and ductile medium Mn steel manufactured via ultrafast heating process, Journal of Materials Science & Technology 97 (2022) 54-68.

[22] K. Steineder, D. Krizan, R. Schneider, C. Béal, C. Sommitsch, On the microstructural characteristics influencing the yielding behavior of ultra-fine grained medium-Mn steels, Acta Materialia 139 (2017) 39-50.

[23] Z.Y. Liang, Z.H. Cao, J. Lu, M.X. Huang, C.C. Tasan, Influence of co-existing medium Mn and dual phase steel microstructures on ductility and Lüders band formation, Acta Materialia 221 (2021).

[24] S. Lee, S.-J. Lee, S. Santhosh Kumar, K. Lee, B.C.D. Cooman, Localized Deformation in Multiphase, Ultra-Fine-Grained 6 Pct Mn Transformation-Induced Plasticity Steel, Metallurgical and Materials Transactions A 42(12) (2011) 3638-3651.

[25] B. Sun, N. Vanderesse, F. Fazeli, C. Scott, J. Chen, P. Bocher, M. Jahazi, S. Yue, Discontinuous strain-induced martensite transformation related to the Portevin-Le Chatelier effect in a medium manganese steel, Scripta Materialia 133 (2017) 9-13.

[26] M. Callahan, O. Hubert, F. Hild, A. Perlade, J.-H. Schmitt, Coincidence of strain-induced TRIP and propagative PLC bands in Medium Mn steels, Materials Science and Engineering: A 704 (2017) 391-400.

[27] J. Bowles, C. Wayman, The bain strain, lattice correspondences, and deformations related to martensitic transformations, Metallurgical Transactions 3 (1972) 1113-1121.

[28] H.K. Bhadeshia, Theory of transformations in steels, CRC Press2021.

[29] J. Mazur, Lattice parameters of martensite and of austenite, Nature 166 (1950) 828-828.

[30] V. Lobodyuk, Y.Y. Meshkov, E.V. Pereloma, On tetragonality of the martensite crystal lattice in steels, Metallurgical and Materials Transactions A 50 (2019) 97-103.

[31] G. Kurdjumow, G. Sachs, Über den mechanismus der stahlhärtung, Zeitschrift für Physik 64(5-6) (1930) 325-343.

[32] Z. Nishiyama, X-ray investigation of the mechanism of the transformation from face-centerd cubic lattice to body-centerd cubic lattice, Sci. Tohoku Univ. 23 (1934) 638.

[33] A.B. Greninger, A.R. Troiano, The mechanism of martensite formation, Jom 1 (1949) 590-598.

[34] G. Olson, M. Cohen, Kinetics of strain-induced martensitic nucleation, Metallurgical transactions A 6(4) (1975) 791-795.

[35] F. Lecroisey, A. Pineau, Martensitic transformations induced by plastic deformation in the Fe-Ni-Cr-C system, Metallurgical and Materials Transactions B 3 (1972) 391-400.

[36] Y.K. Lee, J. Han, Current opinion in medium manganese steel, Materials Science and Technology 31(7) (2014) 843-856.

[37] M. Koyama, M. Rohwerder, C.C. Tasan, A. Bashir, E. Akiyama, K. Takai, D. Raabe, K. Tsuzaki, Recent progress in microstructural hydrogen mapping in steels: quantification, kinetic analysis, and multi-scale characterisation, Materials Science and Technology 33(13) (2017) 1481-1496.

[38] F. Yang, H. Luo, E. Pu, S. Zhang, H. Dong, On the characteristics of Portevin–Le Chatelier bands in cold-rolled 7Mn steel showing transformation-induced plasticity, International Journal of Plasticity 103 (2018) 188-202.

[39] W. Wang, Y. Liu, Z. Zhang, M. Yang, L. Zhou, J. Wang, P. Jiang, F. Yuan, X. Wu, Deformation mechanisms for a new medium-Mn steel with 1.1 GPa yield strength and 50% uniform elongation, Journal of Materials Science & Technology 132 (2023) 110-118.

[40] X.G. Wang, L. Wang, M.X. Huang, Kinematic and thermal characteristics of Lüders and Portevin-Le Châtelier bands in a medium Mn transformation-induced plasticity steel, Acta Materialia 124 (2017) 17-29.

[41] B. Sun, Y. Ma, N. Vanderesse, R.S. Varanasi, W. Song, P. Bocher, D. Ponge, D. Raabe, Macroscopic to nanoscopic in situ investigation on yielding mechanisms in ultrafine grained medium Mn steels: Role of the austenite-ferrite interface, Acta Materialia 178 (2019) 10-25.

[42] Y. Ma, W. Song, S. Zhou, A. Schwedt, W. Bleck, Influence of Intercritical Annealing Temperature on Microstructure and Mechanical Properties of a Cold-Rolled Medium-Mn Steel, Metals 8(5) (2018).

[43] J. Han, S.-J. Lee, J.-G. Jung, Y.-K. Lee, The effects of the initial martensite microstructure on the microstructure and tensile properties of intercritically annealed Fe–9Mn–0.05C steel, Acta Materialia 78 (2014) 369-377.

[44] A. Cottrell, LXXXVI. A note on the Portevin-Le Chatelier effect, The London, Edinburgh, and Dublin Philosophical Magazine and Journal of Science 44(355) (1953) 829-832.

[45] Z.H. Cai, D.L. Zhang, L.F. Ma, H. Ding, Y. Feng, J. Hu, R.D.K. Misra, Competing deformation mechanisms in an austenite-ferrite medium-Mn steel at different strain rates, Materials Science and Engineering: A 818 (2021).

[46] X.G. Wang, B.B. He, C.H. Liu, C. Jiang, M.X. Huang, Extraordinary Lüders-strain-rate in medium Mn steels, Materialia 6 (2019).

[47] S.-J. Lee, J. Kim, S.N. Kane, B.C.D. Cooman, On the origin of dynamic strain aging in twinning-induced plasticity steels, Acta Materialia 59(17) (2011) 6809-6819.

[48] R.S. Varanasi, S. Zaefferer, B. Sun, D. Ponge, Localized deformation inside the Lüders front of a medium manganese steel, Materials Science and Engineering: A 824 (2021).

[49] A.H. Cottrell, B.A. Bilby, Dislocation theory of yielding and strain ageing of iron, Proceedings of the Physical Society. Section A 62(1) (1949) 49.

[50] D.A. Zhemchuzhnikova, M.A. Lebyodkin, T.A. Lebedkina, R.O. Kaibyshev, Unusual behavior of the Portevin–Le Chatelier effect in an AlMg alloy containing precipitates, Materials Science and Engineering: A 639 (2015) 37-41.

[51] L. Kubin, Y. Estrin, C. Perrier, On static strain ageing, Acta metallurgica et materialia 40(5) (1992) 1037-1044.

[52] A. Kozlowska, B. Grzegorczyk, M. Morawiec, A. Grajcar, Explanation of the PLC Effect in Advanced High-Strength Medium-Mn Steels. A Review, Materials (Basel) 12(24) (2019).

[53] S. Lee, B.C. De Cooman, Tensile Behavior of Intercritically Annealed Ultra-Fine Grained 8% Mn Multi-Phase Steel, steel research international 86(10) (2015) 1170-1178.

[54] M. Koyama, T. Yamashita, S. Morooka, Z. Yang, R.S. Varanasi, T. Hojo, T. Kawasaki, S. Harjo, Hierarchical Deformation Heterogeneity during Lüders Band Propagation in an Fe-5Mn-0.1C Medium Mn Steel Clarified through in situ Scanning Electron Microscopy, ISIJ International (2022).

[55] G. Van Rooyen, The stress and strain distribution in a propagating Lüders front accompanying the yield-point phenomenon in iron, Materials Science and Engineering 3(2) (1968) 105-117.

[56] J. Han, S.-H. Kang, S.-J. Lee, Y.-K. Lee, Fabrication of bimodal-grained Al-free medium Mn steel by double intercritical annealing and its tensile properties, Journal of Alloys and Compounds 681 (2016) 580-588.

[57] B.B. He, Z.Y. Liang, M.X. Huang, Nanoindentation investigation on the initiation of yield point phenomenon in a medium Mn steel, Scripta Materialia 150 (2018) 134-138.

[58] B.B. He, M.X. Huang, Z.Y. Liang, A.H.W. Ngan, H.W. Luo, J. Shi, W.Q. Cao, H. Dong, Nanoindentation investigation on the mechanical stability of individual austenite grains in a medium-Mn transformation-induced plasticity steel, Scripta Materialia 69(3) (2013) 215-218.

[59] M. Zhang, R. Li, J. Ding, H. Chen, J.-S. Park, J. Almer, Y.-D. Wang, In situ high-energy X-ray diffraction mapping of Lüders band propagation in medium-Mn transformation-induced plasticity steels, Materials Research Letters 6(12) (2018) 662-667.

[60] Y. Ma, B. Sun, A. Schökel, W. Song, D. Ponge, D. Raabe, W. Bleck, Phase boundary segregation-induced strengthening and discontinuous yielding in ultrafine-grained duplex medium-Mn steels, Acta Materialia 200 (2020) 389-403.

[61] Y. Nakada, A. Keh, Serrated flow in Ni-C alloys, Acta Metallurgica 18(4) (1970) 437-443.

[62] M. Koyama, T. Sawaguchi, K. Tsuzaki, Overview of Dynamic Strain Aging and Associated Phenomena in Fe–Mn–C Austenitic Steels, ISIJ International 58(8) (2018) 1383-1395.

[63] P. Rodriguez, Serrated plastic flow, Bulletin of Materials Science 6 (1984) 653-663.

[64] Y. Zhang, J.P. Liu, S.Y. Chen, X. Xie, P.K. Liaw, K.A. Dahmen, J.W. Qiao, Y.L. Wang, Serration and noise behaviors in materials, Progress in Materials Science 90 (2017) 358-460.

[65] B. Berkowitz, J. Burton, C. Helms, R. Polizzotti, Hydrogen dissociation poisons and hydrogen embrittlement, Scripta Metallurgica 10(10) (1976) 871-873.

[66] O. Barrera, D. Bombac, Y. Chen, T.D. Daff, E. Galindo-Nava, P. Gong, D. Haley, R. Horton, I. Katzarov, J.R. Kermode, C. Liverani, M. Stopher, F. Sweeney, Understanding and mitigating hydrogen embrittlement of steels: a review of experimental, modelling and design progress from atomistic to continuum, J Mater Sci 53(9) (2018) 6251-6290.

[67] M.B. Djukic, G.M. Bakic, V. Sijacki Zeravcic, A. Sedmak, B. Rajicic, The synergistic action and interplay of hydrogen embrittlement mechanisms in steels and iron: Localized plasticity and decohesion, Engineering Fracture Mechanics 216 (2019).

[68] J.H. Ryu, Y.S. Chun, C.S. Lee, H.K.D.H. Bhadeshia, D.W. Suh, Effect of deformation on hydrogen trapping and effusion in TRIP-assisted steel, Acta Materialia 60(10) (2012) 4085-4092.

[69] B. Sun, W. Krieger, M. Rohwerder, D. Ponge, D. Raabe, Dependence of hydrogen embrittlement mechanisms on microstructure-driven hydrogen distribution in medium Mn steels, Acta Materialia 183 (2020) 313-328.

[70] J. Han, J.-H. Nam, Y.-K. Lee, The mechanism of hydrogen embrittlement in intercritically annealed medium Mn TRIP steel, Acta Materialia 113 (2016) 1-10.

[71] J. Zhang, M. Huang, B. Sun, B. Zhang, R. Ding, C. Luo, W. Zeng, C. Zhang, Z. Yang, S. van der Zwaag, H. Chen, Critical role of Lüders banding in hydrogen embrittlement susceptibility of medium Mn steels, Scripta Materialia 190 (2021) 32-37.

[72] C. Shao, W. Hui, Y. Zhang, X. Zhao, Y. Weng, Effect of intercritical annealing time on hydrogen embrittlement of warm-rolled medium Mn steel, Materials Science and Engineering: A 726 (2018) 320-331.

[73] T.M. Park, H.-J. Kim, H.Y. Um, N.H. Goo, J. Han, The possibility of enhanced hydrogen embrittlement resistance of medium-Mn steels by addition of micro-alloying elements, Materials Characterization 165 (2020).

[74] D. Wan, Y. Ma, B. Sun, S.M.J. Razavi, D. Wang, X. Lu, W. Song, Evaluation of hydrogen effect on the fatigue crack growth behavior of medium-Mn steels via in-situ hydrogen plasma charging in an environmental scanning electron microscope, Journal of Materials Science & Technology 85 (2021) 30-43.

[75] B. Sun, W. Lu, B. Gault, R. Ding, S.K. Makineni, D. Wan, C.-H. Wu, H. Chen, D. Ponge, D. Raabe, Chemical heterogeneity enhances hydrogen resistance in high-strength steels, Nature Materials 20(12) (2021) 1629-1634.

[76] Y. Du, X. Gao, L. Lan, X. Qi, H. Wu, L. Du, R.D.K. Misra, Hydrogen embrittlement behavior of high strength low carbon medium manganese steel under different heat treatments, International Journal of Hydrogen Energy 44(60) (2019) 32292-32306.

[77] I. Jeong, K.M. Ryu, D.G. Lee, Y. Jung, K. Lee, J.S. Lee, D.-W. Suh, Austenite morphology and resistance to hydrogen embrittlement in medium Mn transformation-induced plasticity steel, Scripta Materialia 169 (2019) 52-56.

[78] Y. Zhang, W. Hui, J. Wang, M. Lei, X. Zhao, Enhancing the resistance to hydrogen embrittlement of Al-containing medium-Mn steel through heavy warm rolling, Scripta Materialia 165 (2019) 15-19.

[79] T. Chida, Y. Hagihara, E. Akiyama, K. Iwanaga, S. Takagi, M. Hayakawa, H. Ohishi, D. Hirakami, T. Tarui, Comparison of Constant Load, SSRT and CSRT Methods for Hydrogen Embrittlement Evaluation Using Round Bar Specimens of High Strength Steels, ISIJ International 56(7) (2016) 1268-1275.

[80] Y. Li, W. Li, N. Min, H. Liu, X. Jin, Homogeneous elasto-plastic deformation and improved strain compatibility between austenite and ferrite in a co-precipitation hardened medium Mn steel with enhanced hydrogen embrittlement resistance, International Journal of Plasticity 133 (2020).

[81] Z. Wang, J. Xu, J. Li, Effect of heat treatment processes on hydrogen embrittlement in hot-rolled medium Mn steels, International Journal of Hydrogen Energy 45(38) (2020) 20004-20020.

[82] Q. Liu, S. Yang, L. Shen, Q. Zhou, J. Li, Y. Su, L. Qiao, Y. Yan, The effect of hydrogen concentration on the fracture surface of medium Mn steels, Engineering Failure Analysis 108 (2020).

[83] J. Wang, W. Hui, Z. Xie, Z. Wang, Y. Zhang, X. Zhao, Hydrogen embrittlement of a cold-rolled Al-containing medium-Mn steel: Effect of pre-strain, International Journal of Hydrogen Energy 45(41) (2020) 22080-22093.

[84] X. Lu, Y. Ma, M. Zamanzade, Y. Deng, D. Wang, W. Bleck, W.W. Song, A. Barnoush, Insight into hydrogen effect on a duplex medium-Mn steel revealed by in-situ nanoindentation test, International Journal of Hydrogen Energy 44(36) (2019) 20545-20551.

[85] J.H. Ryu, D.-I. Kim, H.S. Kim, H.K.D.H. Bhadeshia, D.-W. Suh, Strain partitioning and mechanical stability of retained austenite, Scripta Materialia 63(3) (2010) 297-299.

[86] A.C. Fischer-Cripps, Critical review of analysis and interpretation of nanoindentation test data, Surface and coatings technology 200(14-15) (2006) 4153-4165.

[87] A.C. Fischer-Cripps, The IBIS Handbook of Nanoindentation, 2013.

[88] J.S. Ng, Adler's Physiology of the Eye, LWW, 2012.

[89] D.B. Murphy, M.W. Davidson, Fundamentals of light microscopy and electronic imaging, John Wiley & Sons2012.

[90] J.C. Brooks-Bartlett, E.F. Garman, The nobel science: one hundred years of crystallography, Interdisciplinary Science Reviews 40(3) (2015) 244-264.

[91] E. Ruska, The development of the electron microscope and of electron microscopy, Reviews of modern physics 59(3) (1987) 627.

[92] D.B. Williams, C.B. Carter, Transmission Electron Microscopy A Textbook for Materials Science, Springer 2009.

[93] A. Ul-Hamid, A beginners' guide to scanning electron microscopy, Springer2018.

[94] J. Edington, Practical electron microscopy in materials science, 3, Interpretation of Transmission Electron Micrographs 37 (1975).

[95] P.K. Rastogi, E. Hack, Optical methods for solid mechanics: a full-field approach, John Wiley & Sons2013.

[96] F. Hild, S. Roux, Digital image correlation: from displacement measurement to identification of elastic properties–a review, Strain 42(2) (2006) 69-80.

[97] M.A. Sutton, J.J. Orteu, H. Schreier, Image correlation for shape, motion and deformation measurements: basic concepts, theory and applications, Springer Science & Business Media2009.

[98] J. Xu, L. Liu, O.S. Hopperstad, B. Holmedal, T. Mánik, K. Marthinsen, A simple method enabling efficient quantitative analysis of the Portevin–Le Chatelier band characteristics, Scripta Materialia 222 (2023).

[99] J.-H. Nam, S.-K. Oh, M.-h. Park, Y.-K. Lee, The mechanism of dynamic strain aging for type A serrations in tensile curves of a medium-Mn steel, Acta Materialia 206 (2021).

[100] P. Reu, Calibration: stereo calibration, Experimental Techniques 38(1) (2014) 1-2.

[101] M.H. Cai, W.J. Zhu, N. Stanford, L.B. Pan, Q. Chao, P.D. Hodgson, Dependence of deformation behavior on grain size and strain rate in an ultrahigh strength-ductile Mn-based TRIP alloy, Materials Science and Engineering: A 653 (2016) 35-42.

[102] S.J. Park, B. Hwang, K.H. Lee, T.H. Lee, D.W. Suh, H.N. Han, Microstructure and tensile behavior of duplex low-density steel containing 5mass% aluminum, Scripta Materialia 68(6) (2013) 365-369.

[103] B. Hu, X. Shen, Q. Guo, Q. Wen, X. Tu, C. Ding, F. Ding, W. Song, H. Luo, Yielding behavior of triplex medium Mn steel alternated with cooling strategies altering martensite/ferrite interfacial feature, Journal of Materials Science & Technology 126 (2022) 60-70.

[104] J. Hu, X. Li, Q. Meng, L. Wang, Y. Li, W. Xu, Tailoring retained austenite and mechanical property improvement in Al–Si–V containing medium Mn steel via direct intercritical rolling, Materials Science and Engineering: A 855 (2022).

[105] Y. Ma, Medium-manganese steels processed by austenite-reverted-transformation annealing for automotive applications, Materials Science and Technology 33(15) (2017) 1713-1727.

[106] S.S. Quek, Z.H. Chooi, Z. Wu, Y.W. Zhang, D.J. Srolovitz, The inverse hall–petch relation in nanocrystalline metals: A discrete dislocation dynamics analysis, Journal of the Mechanics and Physics of Solids 88 (2016) 252-266.

[107] B.S. Rowlands, C. Rae, E. Galindo-Nava, The Portevin-Le Chatelier effect in nickel-base superalloys: Origins, consequences and comparison to strain ageing in other alloy systems, Progress in Materials Science 132 (2023).

[108] J.T. Benzing, W.E. Luecke, S.P. Mates, D. Ponge, D. Raabe, J.E. Wittig, Intercritical annealing to achieve a positive strain-rate sensitivity of mechanical properties and suppression of macroscopic plastic instabilities in multi-phase medium-Mn steels, Mater Sci Eng A Struct Mater 803 (2021).

[109] N. Ranc, D. Wagner, Some aspects of Portevin–Le Chatelier plastic instabilities investigated by infrared pyrometry, Materials Science and Engineering: A 394(1-2) (2005) 87-95.

[110] B.C. De Cooman, Y. Estrin, S.K. Kim, Twinning-induced plasticity (TWIP) steels, Acta Materialia 142 (2018) 283-362.

[111] H.-S.K. Lei Chen, Sung-Kyu Kim, B. C. De Cooman, Localized Deformation due to Portevin–LeChatelier Effect in 18Mn–0.6C TWIP Austenitic Steel, 47(12) (2007) 1804-1812.

[112] G. Sparks, Y. Cui, G. Po, Q. Rizzardi, J. Marian, R. Maaß, Avalanche statistics and the intermittent-to-smooth transition in microplasticity, Physical Review Materials 3(8) (2019).

[113] Y. Cui, G. Po, N. Ghoniem, Influence of loading control on strain bursts and dislocation avalanches at the nanometer and micrometer scale, Physical Review B 95(6) (2017).

[114] Y. Cui, G. Po, N. Ghoniem, Controlling Strain Bursts and Avalanches at the Nano- to Micrometer Scale, Phys Rev Lett 117(15) (2016) 155502.

[115] Y.-S. Chen, H. Lu, J. Liang, A. Rosenthal, H. Liu, G. Sneddon, I. McCarroll, Z. Zhao, W. Li, A. Guo, Observation of hydrogen trapping at dislocations, grain boundaries, and precipitates, Science 367(6474) (2020) 171-175.

[116] H. Fuji, T. Fujishiro, T. Hara, Effect of Ammonium Thiocyanate on Hydrogen Entry Behavior of Low Alloy Steel under Galvanostatic Cathode Charging, ISIJ International 61(4) (2021) 1151-1158.

[117] S. Ajito, T. Hojo, M. Koyama, E. Akiyama, Effects of Ammonium Thiocyanate and pH of Aqueous Solutions on Hydrogen Absorption into Iron under Cathodic Polarization, ISIJ International 61(4) (2021) 1209-1214.

[118] M. Ichiba, K. Takai, J.i. Sakai, Effects of Test Conditions on Corrosion Reactions and Hydrogen Absorption in Hydrogen Embrittlement Tests Using an Ammonium Thiocyanate Solution, ISIJ International 56(3) (2016) 397-404.

[119] S. Takagi, Y. Toji, Application of NH4SCN aqueous solution to hydrogen embrittlement resistance evaluation of ultra-high strength steels, ISIJ international 52(2) (2012) 329-331.

[120] N. Fujimoto, T. Sawada, E. Tada, A. Nishikata, Effect of pH on Hydrogen Absorption into Steel in Neutral and Alkaline Solutions, Materials Transactions 58(2) (2017) 211-217.

[121] B.C. Cameron, M. Koyama, C.C. Tasan, Phase Stability Effects on Hydrogen Embrittlement Resistance in Martensite–Reverted Austenite Steels, Metallurgical and Materials Transactions A 50(1) (2018) 29-34.

[122] X. Shen, W. Song, S. Sevsek, Y. Ma, C. Hüter, R. Spatschek, W. Bleck, Influence of Microstructural Morphology on Hydrogen Embrittlement in a Medium-Mn Steel Fe-12Mn-3Al-0.05C, Metals 9(9) (2019).

[123] Z. Wang, J. Xu, J. Li, Influence of microstructure on hydrogen embrittlement in hot-rolled medium Mn steels, Materials Science and Engineering: A 780 (2020).

[124] J. Kim, C.C. Tasan, Microstructural and micro-mechanical characterization during hydrogen charging: An in situ scanning electron microscopy study, International Journal of Hydrogen Energy 44(12) (2019) 6333-6343.

[125] K. Nibur, D. Bahr, B. Somerday, Hydrogen effects on dislocation activity in austenitic stainless steel, Acta Materialia 54(10) (2006) 2677-2684.

[126] L.Y. Mao, Z.A. Luo, C. Huang, X.M. Zhang, Hydrogen embrittlement behavior in interstitial Mn–N austenitic stainless steel, International Journal of Hydrogen Energy 47(86) (2022) 36716-36732.

[127] J.L. González-Velázquez, Fractography and failure analysis, Springer2018.

[128] M. Wang, M.X. Huang, Abnormal TRIP effect on the work hardening behavior of a quenching and partitioning steel at high strain rate, Acta Materialia 188 (2020) 551-559.

[129] Y. Li, G. Yuan, L. Li, J. Kang, F. Yan, P. Du, D. Raabe, G. Wang, Ductile 2-GPa steels with hierarchical substructure, Science 379(6628) (2023) 168-173.

[130] G. Dehm, B.N. Jaya, R. Raghavan, C. Kirchlechner, Overview on micro- and nanomechanical testing: New insights in interface plasticity and fracture at small length scales, Acta Materialia 142 (2018) 248-282.

Appendix A

A.1 Matlab code for post-processing DIC data

```
clear;
clc;
close all;

gague_start = 3; % data point where the gague start
gague_end = 51; % data point where the gague end
width_start = 7; % data point where the width start
width_end = 11; % data point where the width end
data_start = 0; % where the file numbering start
data_end = 1036; % where the file numbering end
time_gap = 0.04; % resolution of data in second
time_end = (data_end-data_start)*time_gap; % total duration of deformation
strain_max = 0.35; % set color bar limit
strain_min = 0; % set color bar limit
strain_diff_max = 0.003;  % set color bar limit differentiated
strain_diff_min = 0; % set color bar limit differentiated
mid_point = 9; % middle point of the sample width

rows = gague_start:gague_end;
cols = width_start:width_end;

figure(1)
ax = nexttile;
x0=100;
y0=100;
width=500;
height=1000;
set(gcf,'position',[x0,y0,width,height])

% myVideo = VideoWriter('LN26_dic_diff', 'MPEG-4'); % Initialize video
% myVideo.Quality = 100;
```

```
% myVideo.FrameRate = 1/time_gap;  % set frame rate
% figure('units','pixels','position',[0 0 1000 800])
% open(myVideo)
% h = animatedline;


for i = data_start:data_end

    load(['.\LN26_matlab\LN26-0000' num2str(i,'%04.f') '_0.mat']);

    % normalize x and y
    x_max = max(max(x(rows,cols)));
    x_min = min(min(x(rows,cols)));
    y_max = max(max(y(rows,cols)));
    y_min = min(min(y(rows,cols)));
    x_norm = (x(rows,cols) - x_min)/(x_max-x_min);
    y_norm = (y(rows,cols) - y_min)/(y_max-y_min);

    if i == data_start
        strain_prev = zeros(gague_end-gague_start+1, width_end-width_start+1);
    end

    % animation plot
    figure(1)
    p = pcolor(x_norm, y_norm, flip(eyy(rows, cols)*sqrt(2))-strain_prev);
    set(p, 'EdgeColor','none')
    shading interp;
    set(ax,'Colormap',jet,'CLim',[strain_diff_min, strain_diff_max])
    colorbar
    drawnow

%     frame = getframe(gcf); %get frame
%     writeVideo(myVideo, frame);

    % data collect
    strain_all(i+1,:) = eyy(rows, mid_point) * sqrt(2);

    % store the current strain value
    strain_prev = flip(eyy(rows, cols)*sqrt(2));

end

% close(myVideo)

[rows,cols] = size(strain_all);
for i = 1:rows-1
    for j = 1:cols
        strain_all_diff(i,j) = strain_all(i+1,j) - strain_all(i,j);
```

```
    end
end

figure(2)
time_exact = linspace(0,time_end,rows);
ax = nexttile;
pcolor(time_exact, y_norm(:,1)*(gague_end - gague_start + 1)*0.278, flip(strain_all'));
shading interp
set(ax,'Colormap',jet,'CLim',[strain_min, strain_max])
colorbar
xlabel('Time (s)')
ylabel('Axial position (mm)')
set(gca,'FontSize',18)
x0=100;
y0=100;
width=1500;
height=600;
set(gcf,'position',[x0,y0,width,height])

figure(3)
x = linspace(0,time_end,rows-1);
ax = nexttile;
pcolor(time_exact(1:end-1), y_norm(:,1)*(gague_end - gague_start + 1)*0.278, flip(strain_all_diff'));
shading interp
colorbar
set(ax,'Colormap',jet,'CLim',[strain_diff_min, strain_diff_max])
xlabel('Time (s)')
ylabel('Axial position (mm)')
set(gca,'FontSize',18)
x0=100;
y0=100;
width=1500;
height=600;
set(gcf,'position',[x0,y0,width,height])
```

A.2 Matlab code for post-processing infrared camera data

```
clear
clc
close all

figure(1)
ax = nexttile;
x0=100;
```

```
y0=100;
width=400;
height=1000;
set(gcf,'position',[x0,y0,width,height])

[time,point] = size(data); % define the data size
length = 68; % number of data point along length
width = 14; % number of data point along width
mid_point = 5; % middle point of the sample width
gague_start = 18; % data point where the gague start
gague_end = 68; % data point where the gague end
width_start = 4; % data point where the width start
width_end = 7; % data point where the width end
time_end = 41.52; % total duration of deformation
time_gap = 0.04; % resolution of data in second
temp_max = 70; % set color bar limit
temp_min = 20; % set color bar limit
temp_diff_max = 2;  % set color bar limit differentiated
temp_diff_min = 0; % set color bar limit differentiated

time_exact = linspace(0,time_end, time); % map the actual duration

% myVideo = VideoWriter('LN26_temp_diff', 'MPEG-4'); % Initialize video
% myVideo.Quality = 100;
% myVideo.FrameRate = 1/time_gap;  % set frame rate
% figure('units','pixels','position',[0 0 1000 800])
% open(myVideo)
% h = animatedline;


for k = 1:time
    for i = 1:width
        for j = 1:length
            temp(j,i)  = data(k, (i-1)*length + j );
        end
    end

    if k == 1
        temp_prev = zeros(gague_end-gague_start+1, width_end-width_start+1);
    end

    x = gague_start:gague_end;
    y = width_start:width_end;
    x_norm = (x-gague_start)/(gague_end - gague_start);
    y_norm = (y-width_start)/(width_end - width_start);

    % animation plot
    figure(1)
```

```
    pcolor(y_norm, x_norm, temp(x,y)-temp_prev);
    shading interp
    set(ax,'Colormap',hot,'CLim', [temp_diff_min, temp_diff_max])
    colorbar
    drawnow
    disp(k);
%     frame = getframe(gcf); %get frame
%     writeVideo(myVideo, frame);

    % data collect
    temp_all(k,:) = temp((x), mid_point);

    % store the current temp value
    temp_prev = temp(x,y);

end

% close(myVideo)

figure(2)
ax = nexttile;
pcolor(time_exact, x_norm*(gague_end - gague_start + 1)*0.222,temp_all')
shading interp
set(ax,'Colormap',hot,'CLim',[temp_min,temp_max])
colorbar
xlabel('Time (s)')
ylabel('Axial position (mm)')
set(gca,'FontSize',18)
x0=100;
y0=100;
width=1500;
height=600;
set(gcf,'position',[x0,y0,width,height])


% diffrentiated temperature map
[rows,cols] = size(temp_all);
for i = 1:rows-1
    for j = 1:cols
        temp_diff(i,j) = temp_all(i+1,j) - temp_all(i,j);
    end
end

figure(3)
ax = nexttile;
pcolor(time_exact(1:end-1), x_norm*(gague_end - gague_start + 1)*0.222,temp_diff');
shading interp
set(ax,'Colormap',hot,'CLim',[temp_diff_min, temp_diff_max])
```

```
colorbar
xlabel('Time (s)')
ylabel('Axial position (mm)')
set(gca,'FontSize',18)
x0=100;
y0=100;
width=1500;
height=600;
set(gcf,'position',[x0,y0,width,height])
```

A.3 Evidence of VC from TEM images

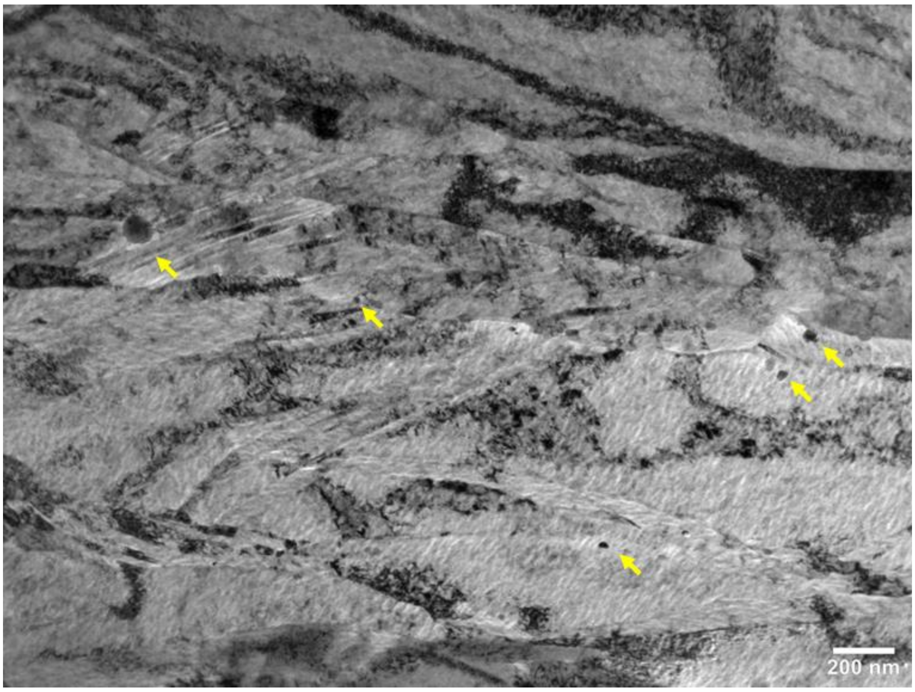

Figure 7.1 VC precipitate found in initial microstructure

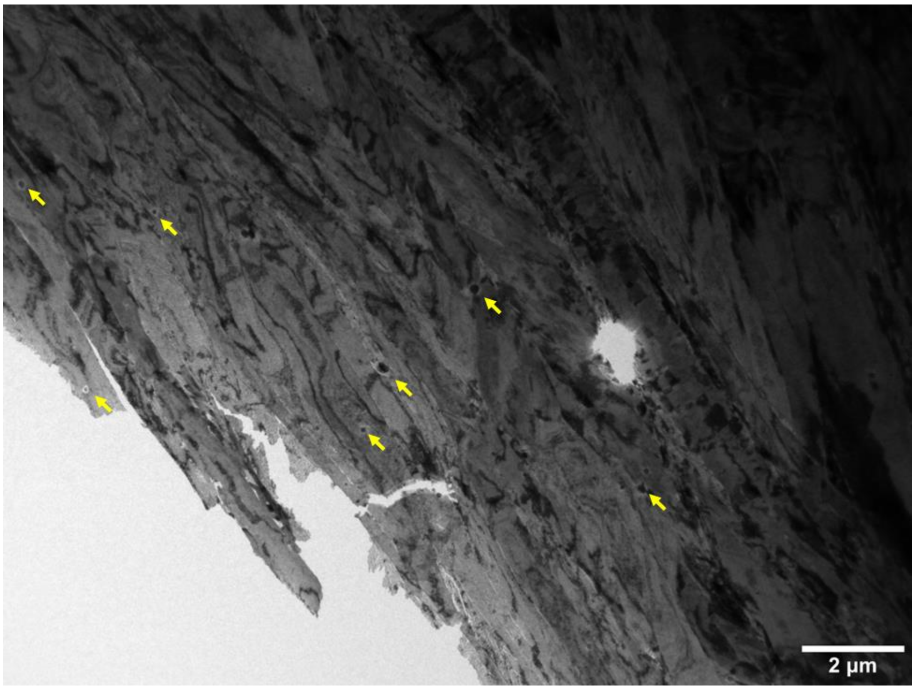

Figure 7.2 VC precipitate found in initial microstructure

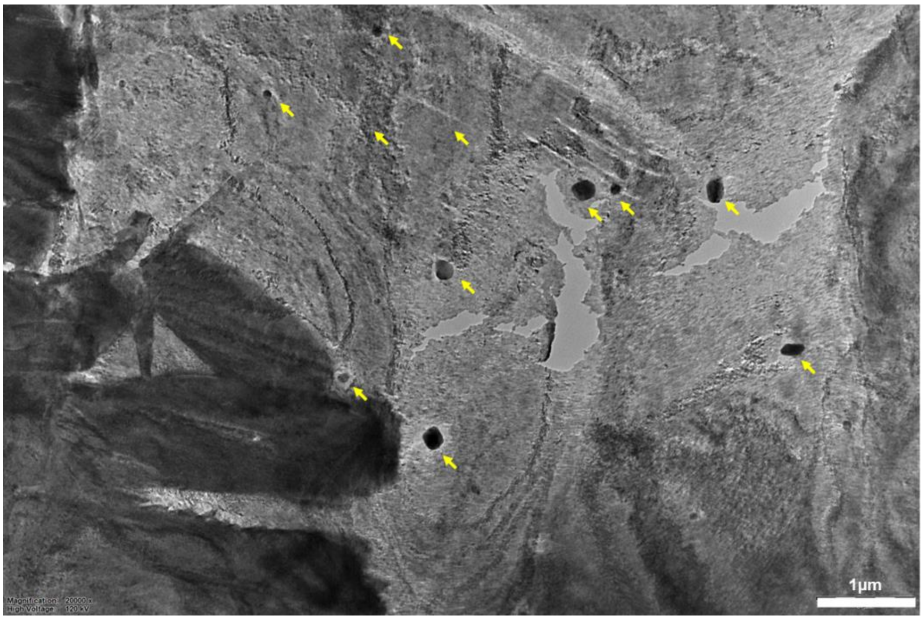

Figure 7.3 VC precipitate found in initial microstructure